RADIATIVE PROPERTIES OF SILICON WAFERS WITH MICROROUGHNESS AND THIN-FILM COATINGS

A Thesis
Presented to
The Academic Faculty

By

Hyunjin Lee

In Partial Fulfillment
Of the Requirements for the Degree
Doctor of Philosophy in the
School of Mechanical Engineering

Georgia Institute of Technology
August, 2006

RADIATIVE PROPERTIES OF SILICON WAFERS WITH MICROROUGHNESS AND THIN-FILM COATINGS

Approved by:

Dr. Zhuomin Zhang, Advisor
Woodruff School of Mechanical Engineering
Georgia Institute of Technology

Dr. Martha Gallivan
School of Chemical and Biomolecular Engineering
Georgia Institute of Technology

Dr. Yogendra Joshi
Woodruff School of Mechanical Engineering
Georgia Institute of Technology

Dr. Yiping Zhao
Department of Physics and Astronomy
University of Georgia

Dr. Kok-Meng Lee
Woodruff School of Mechanical Engineering
Georgia Institute of Technology

Date Approved: June 29, 2006

ACKNOWLEDGEMENTS

I wish to express my sincere appreciation to my advisor, Prof. Zhuomin Zhang, for his support, guidance, and encouragement during the course of this research. His insight and passion have inspired and taught me beyond research. I also thank Prof. Yogendra Joshi, Prof. Kok-Meng Lee, Prof. Martha Gallivan, and Prof. Yiping Zhao for serving on my thesis reading committee and providing helpful suggestions and support on this research.

I would like to thank all my former and current lab colleagues. I thank Dr. Qunzhi Zhu for the assistance and collaboration and Dr. Yihui Zhou for helpful advice. Support and friendship of Keunhan Park and Bong Jae Lee for the ins and outs of school life are much appreciated. I enjoyed the collaboration with Yu-bin Chen and Amanda C. Bryson. I thank Dr. Ceji Fu, Vinh Khuu, Jonathan Barletta, and Soumyadipta Basu for their help and pleasant interactions.

I gratefully acknowledge help and support from the following people: Prof. Pei-feng Hsu in the Florida Institute of Technology, Dr. Kakuen Tang in Boeing Satellite Systems, Inc., Dr. Leonard Hanssen in the National Institute of Standards and Technology, Dr. Heungjoo Shin and Mr. Joel Pikarsky in the Georgia Institute of Technology.

I wish to extend to my deepest thanks to my family, especially my parents, for constant dedication, love, and support. Finally, I appreciate the guidance of my grandparents in heaven.

TABLE OF CONTENTS

ACKNOWLEDGEMENTS iii

LIST OF TABLES vi

LIST OF FIGURES vii

LIST OF SYMBOLS AND ABBREVIATIONS x

SUMMARY xiv

CHAPTER 1 INTRODUCTION 1

CHAPTER 2 BASIC THEORIES 5

2.1 Radiative Properties of Rough Surfaces 5

2.2 Statistical Descriptions of Surface Roughness 9

2.3 Rigorous Wave Scattering Theory 13

2.4 Approximate Wave Scattering Theory 19

CHAPTER 3 ROUGHNESS CHARACTERIZATION AND RADIATIVE PROPERTY MEASUREMEENT 24

3.1 Sample Preparation and Roughness Characterization 24

3.2 Optical Scatterometer for BRDF Measurement 33

3.3 Integrating Sphere for Emittance Measurement 39

CHAPTER 4 DEVELOPMENT OF MONTE CARLO RAY-TRACING METHODS 45

4.1 Geometric-Optics Approximation and Surface Generation Method 45

4.2 Microfacet Slope Method 47

4.2 Consideration of Depolarization 53

CHAPTER 5 ANISOTOPICALLY ROUGH SURFACE SIMULATION 57

5.1 Incorporation of Topography Measurement 57

5.2 BRDF of Bare and Gold-Coated Silicon Surfaces....60
CHAPTER 6 APPLICABILITY OF PHASE RAY-TRACING METHOD....76
6.1 Phase Ray-Tracing Method....76
6.2 Mueller Matrix Comparison....80
CHAPTER 7 BRDF OF ROUGH SURFACES WITH COATING....90
7.1 Analytical Model-Based Approach....90
7.2 BRDF of Silicon Surfaces with SiO_2 Coating....97
CHAPTER 8 ANISOTROPIC ROUGHNESS EFFECTS ON EMITTANCE....104
8.1 Uncertainty Estimation for Emittance Measurements....104
8.2 Emittance of Bare and SiO_2-Coated Silicon Surfaces....106
CHAPTER 9 CONCLUSIONS AND RECOMMENDATIONS....118
REFERENCES....122
VITA....129

LIST OF TABLES

Table 3.1 Basic information about silicon wafers 25

Table 3.2 Roughness statistics of bare silicon surfaces 27

Table 3.3 Coating thickness and roughness statistics of coated surfaces 32

Table 8.1 Correction factor η at the wavelength of 635 nm 110

LIST OF FIGURES

Figure 2.1 Global coordinates for the definition of the BRDF 6

Figure 2.2 Scattering geometry of a 1D rough surface 14

Figure 2.3 Validity domains of approximate methods 20

Figure 3.1 Height distribution functions of Si-1 and Si-2 and Gaussian height distribution functions with the same rms roughness 28

Figure 3.2 2D slope distribution functions in 3D plot (upper) and contour plot (lower) .29

Figure 3.3 Autocorrelation functions along row and column directions or two diagonal directions 31

Figure 3.4 Power spectra along row and column directions or two diagonal directions .31

Figure 3.5 Schematic of the TAAS 34

Figure 3.6 Effectiveness of the procedure to improve the signal-to-noise ratio for BRDF measurements 37

Figure 3.7 Schematic of the setup for spectral radiative property measurements 40

Figure 4.1 Ray tracing between microfacets. 46

Figure 4.2 Effect of the projected area on the probability for an incoming ray to hit a microfacet when $\mathbf{n} \cdot \mathbf{s}_i < 0$ 49

Figure 4.3 Comparison of MSM with the analytical model for a 1D perfectly conducting surface with $\sigma / \tau = 0.1$ 51

Figure 4.4 BRDFs calculated from the rigorous approach, SGM, and MSM for a 1D rough surface with $\sigma / \tau = 1$ and $\sigma / \lambda = 2$ 52

Figure 5.1 In-plane BRDFs of Si-1 for random polarization 62

Figure 5.2 In-plane BRDFs of Si-2 for random polarization 64

Figure 5.3 Predicted first-order scattering and multiple scattering for the in-plane BRDF of Si-2 at $\theta_i = 45°$ and $\phi_i = 45°$ 67

Figure 5.4 In-plane BRDFs of surfaces with gold coating at $\theta_i = 30°$ for random polarization 69

Figure 5.5 Out-of-plane BRDFs of Si-2 at $\theta_i = 0°$ and $\phi_i = 45°$ 71

Figure 5.6 BRDFs predicted by MSM at $\theta_i = 30°$ for random polarization 73

Figure 5.7 In-plane BRDFs of Si-2 for random polarization at large incidence angles...74

Figure 6.1 Optical path difference between two rays leaving the surface in the same direction 77

Figure 6.2 Mueller matrix elements for a silicon surface with $\sigma/\lambda = 0.3$ and $\tau/\lambda = 6$ when $\theta_i = 30°$ 81

Figure 6.3 Mueller matrix elements for a silicon surface with $\sigma/\lambda = 0.3$ and $\tau/\lambda = 6$ when $\theta_i = 0°$ 83

Figure 6.4 Mueller matrix elements for a silicon surface with $\sigma/\lambda = 0.1$ and $\tau/\lambda = 2$ when $\theta_i = 0°$ and their coherent and incoherent components.....84

Figure 6.5 Mueller matrix elements for a gold surface with $\sigma/\lambda = 0.3$ and $\tau/\lambda = 6$ when $\theta_i = 0°$ 88

Figure 6.6 Coherent and incoherent components of the Mueller matrix elements for a gold surface with $\sigma/\lambda = 0.1$ and $\tau/\lambda = 2$ when $\theta_i = 0°$ 88

Figure 7.1 Schematic of a thin-film coated rough surface 92

Figure 7.2 Cross sections of the SDF obtained from AFM and BRDF measurements for the bare silicon samples at two different azimuthal angles 95

Figure 7.3 In-plane BRDFs of Si-1 for random polarization at $\theta_i = 0°$ with different coating thicknesses 96

Figure 7.4 In-plane BRDFs of Si-2 for random polarization at $\theta_i = 0°$ with different coating thicknesses 98

Figure 7.5 In-plane BRDFs of Si-1 for random polarization at $\theta_i = 45°$ with different coating thicknesses 100

Figure 7.6 In-plane BRDFs of Si-2 for random polarization at $\theta_i = 45°$ with different coating thicknesses 102

Figure 8.1 Comparison of emittance measurements with theoretical calculations for a double-side-polished wafer of 200 μm thickness 105

Figure 8.2 Emittance of Si-1 and Si-2 at near normal incidence 107

Figure 8.3 Emittance of Si-1 and Si-2 at the wavelength of 635 nm for two azimuthal angles $\phi_i = 0°$ and $\phi_i = 45°$ 111

Figure 8.4 Emittance of Si-1 and Si-2 with a 107.2 nm thick SiO_2 coating at near normal incidence 113

Figure 8.5 Emittance of Si-1 and Si-2 with 216.5 nm and 324.6 nm thick SiO_2 coatings at near normal incidence 115

LIST OF SYMBOLS AND ABBREVIATIONS

A	area
C	autocorrelation function
D	diameter, mm
E	electric field
F	normal derivative of electric field or view factor
f_r	bidirectional reflectance distribution function, sr^{-1}
G	Green's function or energy of ray bundles
g	comparison function
$\mathbf{h}$	unit vector perpendicular to the plane of incidence or reflection
h	(average) coating thickness, nm
I	intensity
i	$\sqrt{-1}$
$\mathbf{k}$	wave vector
$\mathbf{k}^-$	$\mathbf{k}_i - \mathbf{k}_r$
$\mathbf{k}^+$	$\mathbf{k}_i + \mathbf{k}_r$
k	wave number
l	length of a surface, μm
$\mathbf{M}$	Mueller matrix
m	element of the Mueller matrix

n complex refractive index

P power spectrum

p_s slope distribution function

p_w weighted slope distribution function

R Fresnel's reflection coefficient or uniform random number

$\mathcal{R}$ directional hemispherical spectral reflectance

$\mathbf{r}$ position vector

r absolute value of a position vector or distance

$\mathbf{S}$ Stokes vector

S Smith shadowing function or surface

$\mathbf{s}$ unit vector in the direction of incidence or reflection

T temperature

$\mathcal{T}$ directional hemispherical spectral transmittance

V volume or electrical signal

$\mathbf{v}$ unit vector parallel to the plane of incidence or reflection

w root-mean-square slope

Greek symbols

α inclination angle, deg

β phase shift

Γ	weight function
ε	directional spectral emittance or dielectric constant
ζ	microfacet slope
η	correction factor
θ	zenith angle, deg
θ_f	refraction angle, deg
λ	wavelength in vacuum, μm
ξ	height of surface rough, μm
ρ	microfacet reflectivity
σ	root-mean-square roughness, μm
τ	autocorrelation length, μm
ϕ	azimuthal angle, deg
χ	characteristic function
ψ	local incidence angle, deg
ω	solid angle, sr

Subscripts

0	air
coh	coherent component
f	film

i	incidence
inc	incoherent component
obs	observation
p	*p* polarization (TM wave)
r	reflection
s	*s* polarization (TE wave), substrate, or sample
w	sphere wall

Abbreviations

AFM	atomic force microscope
BRDF	bidirectional reflectance distribution function
BTDF	bidirectional transmittance distribution function
GOA	geometric-optics approximation
KA	Kirchhoff approximation
LPRT	light-pipe radiation thermometer
MSM	microfacet slope method
PRTM	phase ray-tracing method
RTP	rapid thermal processing
SDF	slope distribution function
SGM	surface generation method
TAAS	three-axis automated scatterometer

SUMMARY

The bidirectional reflectance distribution function (BRDF) that describes the scattered energy distribution is the most fundamental radiative property to calculate other properties. Although recent progress in surface metrology allows topography measurement in an atomic level, most studies still assume statistical distributions of roughness because of difficulty in roughness modeling. If the BRDF of rough silicon wafers is modeled with assumptions, predicted radiative properties may be inaccurate because non-Gaussian and anisotropic roughness of some wafers cannot be approximated with known statistics. Therefore, this thesis focuses on development of BRDF modeling that accounts for anisotropic roughness to accurately predict radiative properties of rough silicon surfaces with thin-film coatings. Monte Carlo ray-tracing methods are developed to consider multiple scattering and the change of polarization states and to satisfy physical laws such as the reciprocity principle. Silicon surface topographic data measured with an atomic force microscope are incorporated into the ray-tracing algorithms to model anisotropic roughness statistics. For validation, BRDF and emittance predictions are compared with measurements using an optical scatterometer and an integrating sphere. Good agreement between prediction and measurement demonstrates that the incorporation of topography measurement into BRDF modeling is essential for accurate property prediction. Roughness effects on the BRDF are so strong that BRDFs also reveal anisotropic features regardless of the presence of coating. Anisotropic roughness increases multiple scattering although first-order scattering is dominant, and thus enhances emittance noticeably. Silicon dioxide coating changes the magnitude of BRDF

and emittance and reduces the anisotropic roughness effect on emittance enhancement. The research in this thesis advances the method to predict radiative properties by incorporating anisotropic rough statistics into BRDF modeling.

CHAPTER 1

INTRODUCTION

Since the late 19th century, wave scattering from rough surfaces has been studied in various areas such as optics, heat transfer, acoustics, geophysics, remote sensing, and computer graphics. Particularly, many researchers in heat transfer have been interested in electromagnetic wave scattering to account for radiative property variation due to surface roughness. The most fundamental radiative property describing the scattered energy distribution is the bidirectional reflectance distribution function (BRDF), as other properties can be calculated from BRDF [1-3]. Early studies modeled the BRDF with simple assumptions such as diffuse or specular reflections or combination of both. From 1940s to 1960s, formulation and modification of approximate models led to a remarkable leap in wave scattering theory [4-7]. Since 1980s, numerical solutions of wave equations have been calculated by aid of computational progress [8-11]. Rigorous solutions have expanded understanding of wave scattering and assisted to identify the validity domain of approximations. Along with advancements in scattering theory, BRDF modeling becomes more sophisticated and realistic [12-17].

Recent developments in surface metrology allow topography measurement even in an atomic scale and the precise determination of roughness statistics. The use of precise roughness statistics for BRDF models could improve the prediction of radiative properties. However, because of difficulty in modeling surface roughness, most studies did not fully take advantage of advancements in topography measurement for BRDF modeling. They imported only roughness parameters, such as the root-mean-square (rms)

roughness and the autocorrelation length, from topography measurement while assuming statistical distribution functions, most commonly from Gaussian statistics [4-6]. Furthermore, two-dimensional (2D) surface roughness statistics are often assumed to be isotropic so that they adopt BRDF modeling from one-dimensional (1D) surfaces. If surface roughness disobeys those assumptions, predicted radiative properties may largely differ from actual properties. Hence, BRDF modeling based on actual surface profiles is imperative for the accurate prediction of radiative properties.

Accurate radiative properties are very important for temperature measurement in rapid thermal processing (RTP). RTP is a key technique in semiconductor manufacturing to shrink device size in integrated circuits and increase their packing density [18-20]. In RTP technique, accurate temperature measurement is crucial to achieve wafer temperature uniformity and process repeatability [21,22]. Due to fast response and non-intrusiveness, a light-pipe radiation thermometer (LPRT) is frequently chosen to monitor wafer temperature during a process [22-24]. Temperature uncertainty requirement is ± 2°C at 1000°C, and then emittance uncertainty should be less than 2% [24]. An LPRT usually views the unpolished backside of wafers, whose roughness scatters the incident light and thereby increases emittance uncertainty [25,26]. Zhu and Zhang demonstrated that microstructures created during chemical etching process of some commercial silicon wafers result in non-Gaussian and anisotropic roughness statistics [27,28]. Although they demonstrated that non-Gaussian and anisotropic roughness strongly affects the BRDF, only the in-plane BRDF is predicted because of limitations of their analytical model-based approach. A BRDF modeling method that predicts the out-of-plane BRDF should be developed to investigate anisotropic roughness effects on the emittance.

In addition to anisotropic roughness modeling, further considerations in BRDF modeling should be taken for accurate property prediction of rough silicon surfaces. First, multiple scattering is important because it significantly changes radiative properties; for instance, backscattering or emittance enhancements [29,30]. If a surface is very rough, deep roughness cavities may cause multiple scattering and trap the incident light [1-3]. In general, analytical BRDF models cannot deal with multiple scattering. Second, the change of polarization states due to scattering, or depolarization, needs to be considered as well. Most studies in heat transfer assumed that polarization changes are counterbalanced for unpolarized light based on random roughness statistics. However, because silicon surface roughness with anisotropic microstructures is not random in a strict sense, this assumption may not be valid. Radiative properties of an anisotropic surface may be accurately modeled with the consideration of depolarization, which also reveals property dependence on the incident polarization. Finally, the presence of oxide and other thin-film coatings should be considered. Thin-film coatings are commonly present on wafers and significantly alter radiative properties depending on their optical constants and thickness. These considerations impose more difficulty on development of BRDF modeling.

The research in this thesis aims at BRDF modeling to predict radiative properties of rough silicon wafers, focusing on anisotropic roughness statistics. Ray-tracing algorithms using the Monte Carlo technique are developed to consider multiple scattering and depolarization while physical laws such as the reciprocity principle are satisfied. Silicon surface topography is measured with an atomic force microscope (AFM), and topography measurements are incorporated into the ray-tracing algorithms to account for

anisotropic roughness statistics. Furthermore, a modified ray-tracing method to trace the field amplitude and phase is explored to identify whether it can deal with wave effects. Additionally, an analytical model-based approach is proposed for coated surfaces to eliminate modeling errors caused by topography measurement. For validation of modeling developments, predictions are compared with experimental results. The BRDF is measured with an optical scatterometer after signal-to-noise ratio enhancement, and an integrating sphere with monochromatic light sources is set up for emittance measurement.

This thesis is organized as follows. Chapter 2 summarizes basic theories; radiative property definitions, statistical roughness descriptions, and rigorous and approximate wave scattering theories. Chapter 3 presents sample roughness statistics obtained from AFM measurements and describes instruments for property measurement. Chapter 4 describes development of two Monte Carlo ray-tracing methods. In Chapter 5, BRDFs of bare and gold-coated surfaces with anisotropic roughness are studied after the incorporation of topography measurements. Chapter 6 examines the modified ray-tracing method to assess its applicability for surfaces with small roughness parameters. In Chapter 7, BRDF variation with silicon dioxide coating thickness is investigated with an analytical model. In Chapter 8, anisotropic roughness effects on the emittance are studied. Chapter 9 concludes this thesis with recommendations for future works.

CHAPTER 2

BASIC THEORIES

This chapter summarizes basic theories relevant to this thesis. First, radiative properties associated with scattering are introduced. Various statistical distribution functions and parameters to characterize surface roughness are presented, and the spectral method used for numerical generation of rough surfaces is briefly introduced. A rigorous approach to the numerical solution of Maxwell's equations is summarized to gain physical insight of scattering problems. Because it is not practical to apply the rigorous approach for scattering from 2D rough surfaces, approximate methods to tackle scattering from rough silicon surfaces are selected and their basic features are presented.

2.1 Radiative Properties of Rough Surfaces

The emittance is a key radiative property for radiation thermometry, and its uncertainty determines the accuracy of temperature measurements [25,26]. The emittance indicates how well a real body radiates energy as compared with a blackbody, and its definition is a ratio of the energy emitted from a real surface to the energy emitted from a blackbody at the same temperature [1,2]. The directional spectral emittance is defined by

$$\varepsilon\left(T,\lambda,\theta,\phi\right)=\frac{I\left(T,\lambda,\theta,\phi\right)\cos\theta d\omega}{I_b\left(T,\lambda\right)\cos\theta d\omega}=\frac{I\left(T,\lambda,\theta,\phi\right)}{I_b\left(T,\lambda\right)} \tag{2.1}$$

The radiative intensity I is defined as radiative power per unit wavelength λ per unit solid ω angle per unit area projected to propagation direction $\left(\theta,\phi\right)$. The term $I\cos\theta d\omega$

represents radiative power per unit wavelength. The emittance is basically a function of wavelength, temperature, and direction.

The BRDF is defined as a ratio of the reflected intensity I_r to the radiative power on spectral basis [1,2].

$$f_r\left(\lambda,\theta_i,\phi_i,\theta_r,\phi_r\right)=\frac{I_r\left(\lambda,\theta_i,\phi_i,\theta_r,\phi_r\right)}{I_i\left(\lambda,\theta_i,\phi_i\right)\cos\theta_i d\omega_i}[\mathrm{sr}^{-1}] \tag{2.2}$$

In the spherical coordinates as shown in Figure 2.1, (θ_i, ϕ_i) and (θ_r, ϕ_r) denote incidence and reflection directions, respectively. The BRDF describes how the incident energy spreads over the upper hemisphere after scattering from rough surfaces. If a material is not opaque, the bidirectional transmittance distribution function (BTDF) can be similarly defined with Equation 2.2 by replacing the reflected intensity with the transmitted intensity. The knowledge of BRDF and BTDF enables the calculation of radiative heat transfer between rough surfaces or the determination of an effective emittance at given

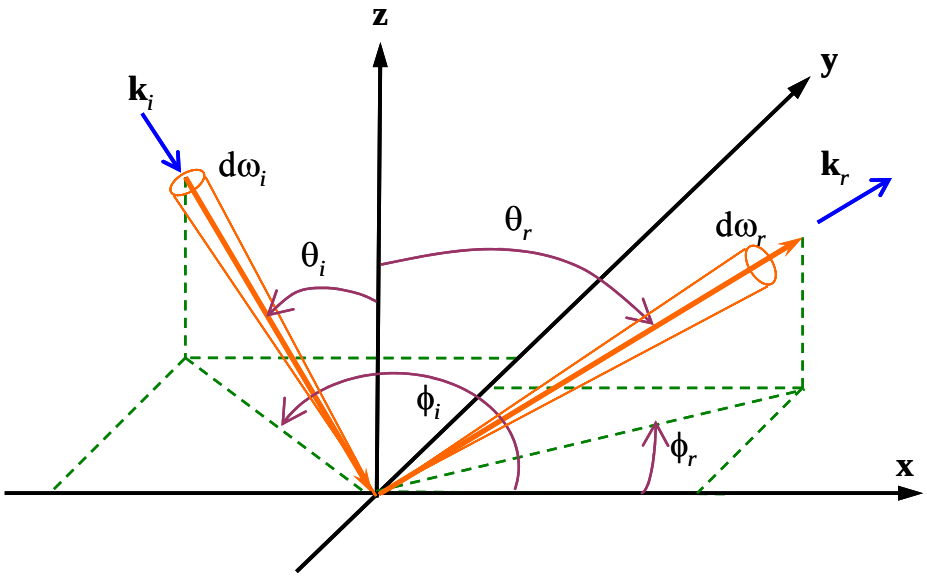

Figure 2.1 Global coordinates for definition of the BRDF. The *x*- *y* plane is the mean plane of a rough surface, and the *z*-axis is normal to the mean plane. The wave vectors of incidence and reflection are denoted by $\mathbf{k}_i$ and $\mathbf{k}_r$,

radiation environment [31-34].

Both BRDF and BTDF are the most fundamental radiative properties, and other hemispherical properties can be obtained from their integration. The directional-hemispherical spectral reflectance $\mathcal{R}$ is given by

$$\mathcal{R} = \int_{2\pi} f_r \left(\lambda, \theta_i, \phi_i, \theta_r, \phi_r\right) \cos\theta_r \mathrm{d}\omega_r \tag{2.3}$$

Similarly, the directional-hemispherical spectral transmittance $\mathcal{T}$ can be calculated from the BTDF. Energy conservation and Kirchhoff's law connect the directional emittance with the directional-hemispherical reflectance and transmittance.

$$\varepsilon = 1 - \mathcal{R} - \mathcal{T} \tag{2.4}$$

Because all radiative properties in this thesis are presented on spectral basis, spectral dependence is not explicitly expressed for simple notation. Furthermore, the emittance simply refers to the directional emittance henceforth while the reflectance (transmittance) refers to the directional-hemispherical reflectance (transmittance). Throughout this thesis, meanwhile, the ending *–ivity* is assigned for properties of optically smooth surfaces, otherwise the ending *–ance* is used.

Polarization effects are generally not considered in heat transfer because emitted light is randomly polarized. However, because scattering from rough surfaces alters the polarization state, dependence of radiative properties on polarization is important to understand scattering further. The Stokes vector or parameters fully describes the polarization state. The Stokes vector of a monochromatic plane wave consists of four elements as follows:[2,35]

$$\mathbf{S} = \begin{bmatrix} I \\ Q \\ U \\ V \end{bmatrix} = \begin{bmatrix} I_p + I_s \\ I_p - I_s \\ I_{+45} - I_{-45} \\ I_{rhc} - I_{lhc} \end{bmatrix} = \begin{bmatrix} \left\langle E_p E_p^* + E_s E_s^* \right\rangle \\ \left\langle E_p E_p^* - E_s E_s^* \right\rangle \\ \left\langle E_p E_s^* + E_s E_p^* \right\rangle \\ i\left\langle E_p E_s^* - E_s E_p^* \right\rangle \end{bmatrix} \tag{2.5}$$

An electric field amplitude and its conjugate are denoted by E and E^*, respectively, and the bracket $\langle\ \rangle$ represents the ensemble average. Subscripts in the intensities stand for the linear polarization states of *p*, *s* , +45°, and -45°, as well as the circular polarizations of right hand (*rhc*) and left hand (*lhc*). Scattering alters the Stokes vector of the incident field to that of the scattered field, and the Mueller matrix, **M,** characterizes the transform of the two Stokes vectors. The Mueller matrix is generally a 4×4 matrix with 16 elements, but only four independent elements remain for scattering from 1D rough surfaces [36].

$$\begin{bmatrix} I_r \\ Q_r \\ U_r \\ V_r \end{bmatrix} = \begin{bmatrix} m_{11} & m_{12} & 0 & 0 \\ m_{12} & m_{11} & 0 & 0 \\ 0 & 0 & m_{33} & m_{34} \\ 0 & 0 & -m_{34} & m_{33} \end{bmatrix} \begin{bmatrix} I_i \\ Q_i \\ U_i \\ V_i \end{bmatrix} \text{ or } \mathbf{S}_r = \mathbf{M}\mathbf{S}_i \tag{2.6}$$

Because coherent components account for wave features, the distinction between coherent and incoherent components is necessary. The sum of coherent and incoherent components gives the total intensity of electric fields. Phase terms of the field allow the consideration of wave features; for instance, in-phase and out-of-phase lead to constructive and destructive interference, respectively. The coherent components retain phase terms in the summation of ensemble averages before calculation of the complex modulus. Therefore, the coherent components are able to account for wave features. On the other hand, the incoherent components represent an algebraic sum of the complex

modulus $|E|^2$. As a result, information about phase is lost, and wave features cannot be explained with the incoherent components. Coherent and incoherent components of the Stoke vectors are expressed by

$$\mathbf{S}_{coh} = \begin{bmatrix} I_{coh} \\ Q_{coh} \\ U_{coh} \\ V_{coh} \end{bmatrix} = \begin{bmatrix} \langle E_p \rangle \langle E_p^* \rangle + \langle E_s \rangle \langle E_s^* \rangle \\ \langle E_p \rangle \langle E_p^* \rangle - \langle E_s \rangle \langle E_s^* \rangle \\ \langle E_p \rangle \langle E_s^* \rangle + \langle E_s \rangle \langle E_p^* \rangle \\ i\langle E_p \rangle \langle E_s^* \rangle - i\langle E_s \rangle \langle E_p^* \rangle \end{bmatrix} \tag{2.7a}$$

$$\mathbf{S}_{inc} = \mathbf{S} - \mathbf{S}_{coh} \tag{2.7b}$$

The coherent and incoherent components of the Mueller matrix can be calculated from those of the incident and reflected Stokes vectors as well.

2.2 Statistical Descriptions of Surface Roughness

No two rough surfaces are identical, and a rough surface often is referred to a random process. Because of random nature, statistical descriptions are important to characterize a rough surface [5,37]. The continuous profile $\xi(\mathbf{r})$ of a rough surface represents the variation of roughness height from a smooth mean plane $\xi(\mathbf{r}) = 0$, and statistical distributions and parameters are calculated from the profile. The most basic function is the height distribution function (HDF), which gives a probability that roughness height lies between ξ and ξ+dξ. A histogram to represent the frequency of height is calculated from the profile, and the histogram becomes the HDF $p_h(\xi)$ after normalization. The moments of HDF yield various roughness parameters.

$$\left\langle \xi^n \right\rangle = \int_{-\infty}^{\infty} \xi^n p_h(\xi)\,\mathrm{d}\xi \tag{2.8}$$

The first-order moment is a mean of roughness, and the second-order moment defines the rms roughness σ. The third-order moment divided by σ^3 gives a skewness of roughness, and similarly the fourth-order moment normalized with the rms roughness becomes a kurtosis. The Gaussian HDF is expressed by

$$p_h(\xi) = \frac{1}{\sqrt{2\pi\sigma^2}} \exp\left(-\frac{\xi^2}{2\sigma^2}\right) \tag{2.9}$$

The autocorrelation function (ACF) represents lateral scales of roughness whereas the HDF does vertical scales. The ACF, $C(\mathbf{r})$, is defined by

$$C(\mathbf{r}) = \frac{\left\langle \xi(\mathbf{r}')\xi(\mathbf{r}+\mathbf{r}') \right\rangle}{\sigma^2} \tag{2.10}$$

The ACF of rough surfaces generally decays to zero as $\mathbf{r}$ increases with $C(0)=1$. The unnormalized ACF is called the autocovariance function $\sigma^2 C(\mathbf{r})$. The Gaussian ACF is

$$C(x,y) = \exp\left(-\frac{x^2}{\tau_x^2} - \frac{y^2}{\tau_y^2}\right) \tag{2.11}$$

Because the Gaussian ACF is isotropic, the autocorrelation lengths τ_x and τ_y in x and y directions are the same as τ. Since the rms roughness σ and the autocorrelation length τ respectively represent vertical and horizontal roughness scales, their ratio is related with steepness of surface roughness.

Steepness is usually described by the slope distribution function (SDF) $p_s(\zeta)$ that is similarly calculated as the HDF. However, the SDF for a 2D surface is generally

represented as a 2D histogram of slopes in x and y directions ($\zeta_x = \partial\xi / \partial x$ and $\zeta_y = \partial\xi / \partial y$) because slopes depend on a direction. The Gaussian SDF is

$$p_s\left(\zeta_x, \zeta_y\right) = \frac{1}{2\pi w_x w_y} \exp\left(-\frac{\zeta_x^2}{2w_x^2} - \frac{\zeta_y^2}{2w_y^2} \right) \tag{2.12}$$

where w_x and w_y are the rms slopes in x and y directions and isotropy results in their equality to the rms slope w. The relation between the rms slope and the ratio of rms roughness and autocorrelation length can be derived as $w = \sqrt{2}\sigma / \tau$ if a surface roughness follows Gaussian statistics. Although many studies used the Gaussian SDF, some studies [12,38] assumed that the tangent of inclination angles, $\tan\alpha$, follows a Gaussian distribution. The inclination angle α represents an angle between a microfacet normal vector and the z-axis, and thus $\tan\alpha = \sqrt{\zeta_x^2 + \zeta_y^2}$. If this surface is isotropic, its SDF in terms of ζ_x and ζ_y can be obtained using the Jacobian transformation [39].

$$p_s\left(\zeta_x, \zeta_y\right) = \frac{1}{\left(2\pi\right)^{3/2} w \sqrt{\zeta_x^2 + \zeta_y^2}} \exp\left(-\frac{\zeta_x^2 + \zeta_y^2}{2w^2} \right) \tag{2.13}$$

In the above equation, w means the rms value of $\tan\alpha$. The SDF in Equation 2.13 is called the Rayleigh distribution function and describes non-Gaussian slope distributions with a sharper peak if the same value of the rms slope is applied to both Equations 2.12 and 2.13.

The power spectrum or power spectral density function is another description of rough surfaces, which contains the information of both vertical and lateral roughness

scales in the Fourier space. The power spectrum $P(\mathbf{k})$ is defined as the Fourier transform of the autocovariance function and expressed by

$$P(\mathbf{k}) = \frac{\sigma^2}{(2\pi)^2}\int_{-\infty}^{\infty} C(\mathbf{r})\exp(i\mathbf{k}\cdot\mathbf{r})\,\mathrm{d}\mathbf{r} = \frac{1}{(2\pi l)^2}\left|\int_{-\infty}^{\infty}\xi(\mathbf{r})\exp(i\mathbf{k}\cdot\mathbf{r})\,\mathrm{d}\mathbf{r}\right|^2 \qquad (2.14)$$

where l denotes surface length. The power spectrum is a nonnegative, real function, and its integration in the Fourier space gives the variance σ^2 . The power spectrum corresponding to the Gaussian ACF is

$$P(k_x, k_y) = \frac{\sigma^2\tau_x\tau_y}{4\pi}\exp\left(-\frac{k_x^2\tau_x^2 + k_y^2\tau_y^2}{4}\right) \qquad (2.15)$$

Meanwhile, the characteristic function of roughness height $\chi(k)$ means the average of $\exp(ik\xi)$

$$\chi(k) = \langle\exp(ik\xi)\rangle = \int_{-\infty}^{\infty} p_h(\xi)\exp(ik\xi)\,\mathrm{d}\xi. \qquad (2.16)$$

The characteristic function is equal to the Fourier transform of the HDF and contains the same information. The Gaussian characteristic function for 1D surfaces is

$$\chi(k) = \exp\left(-\frac{\sigma^2 k^2}{2}\right) \qquad (2.17)$$

The numerical generation of rough surfaces with the same statistics is important for the study related with rough surfaces. Such a numerical rough surface is referred to as a surface realization, and the spectral method is commonly used [5,40,41]. In the spectral method, the discrete Fourier function of a surface profile $H(k_{x_m}, k_{y_n})$ can be defined with the power spectrum, or equivalently with both the ACF and the rms roughness.

$$H\left(k_{x_m},k_{y_n}\right)=2\pi l\sqrt{P\left(k_{x_m},k_{y_n}\right)}\begin{cases}\dfrac{N\left(0,1\right)+iN\left(0,1\right)}{\sqrt{2}} & m,n\neq 0,\dfrac{N}{2}\\ N\left(0,1\right) & m \text{ or } n=0,\dfrac{N}{2}\end{cases} \tag{2.18}$$

$$k_{x_m}=\frac{2\pi m}{l},\ k_{y_n}=\frac{2\pi n}{l}$$

Here, N stands for the number of nodes, and $N\left(0,1\right)$ denotes random numbers that follow the Gaussian distribution with zero mean and unit variance. For negative values of m and n, the complex conjugate of H is used. The inverse Fourier transform of H yields the surface profile $\xi\left(x,y\right)$.

$$z=\xi\left(x,y\right)=\frac{1}{l^2}\sum_{m=-N/2}^{N/2-1}\sum_{n=-N/2}^{N/2-1}H\left(k_{x_m},k_{y_n}\right)\exp\left(ik_{x_m}x+ik_{y_n}y\right) \tag{2.19}$$

If the power spectrum used in Equation 2.18 is Gaussian, the surface realization is often referred as the Gaussian process. In this thesis, the Gaussian process will be simply referred to as the Gaussian surface.

2.3 Rigorous Wave Scattering Theory

A rigorous approach to scattering from rough surfaces is to solve Maxwell's equations by virtue of differential or integral numerical schemes. Rigorous solutions provide the scattered field for a surface realization, and scattering properties are statistically obtained from an ensemble average. The boundary integral method, based on the extinction theorem and Green's theorem, are most commonly applied to surface scattering problems. Early studies using the boundary integral method were mainly interested in accounting for backscattering enhancement by dealing with 1D perfectly conducting surfaces [10,42]. Afterwards, the boundary integral method was extended to

scattering from dielectric surfaces [11] and thin-film coated surfaces [43,44]. In the following, formulation of the boundary integral method for scattering from a 1D dielectric surface is introduced based on Refs. [10,11].

Scattering of waves with *s* polarization (TE wave) is only formulated because of the analogy between two polarizations, and final formulation for *p* polarization (TM wave) will be presented later. Figure 2.2 illustrates a scattering geometry, where a monochromatic plane wave $\mathbf{E}_i(\mathbf{r}) = \hat{j}E_i e^{i\mathbf{k}_i\cdot\mathbf{r}}$ from a semi-infinite vacuum (V_0) with a wave vector $\mathbf{k}_i$ is incident on a 1D dielectric rough surface. Due to roughness at the interface $z = \xi(x)$, the incident light is scattered to the vacuum with a wave vector $\mathbf{k}_r$. At a given wave number $k = 2\pi/\lambda$, wave vectors are given as follows:

$$\mathbf{k}_i = k(\sin\theta_i, 0, -\cos\theta_i) \tag{2.20a}$$

$$\mathbf{k}_r = k(\sin\theta_r, 0, \cos\theta_r) \tag{2.20b}$$

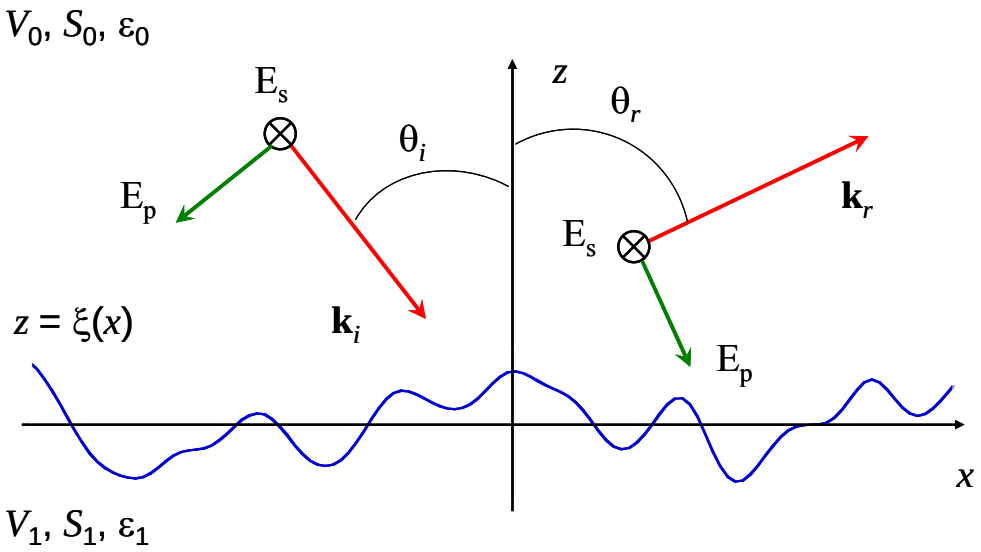

Figure 2.2 Scattering geometry of a 1D rough surface. The surface profile $\xi(x)$ separates the half-space $z < \xi(x)$, filled with an isotropic and homogeneous medium (V_1), from vacuum (V_0).

The vacuum and the dielectric medium have dielectric constants, $\varepsilon_0 = 1$ and $\varepsilon_1(\lambda)$, respectively, and both media are surrounded by semi-infinite surfaces S_0 and S_1, respectively.

Solutions of the following Helmholtz equations give the field scattered from the rough surface.

$$\nabla^2 E_0(\mathbf{r}) + k^2 E_0(\mathbf{r}) = 0, \qquad z > \xi(x), (\mathbf{r} \in V_0) \tag{2.21a}$$

$$\nabla^2 E_1(\mathbf{r}) + \varepsilon_1 k^2 E_1(\mathbf{r}) = 0, \qquad z < \xi(x), (\mathbf{r} \in V_1) \tag{2.21b}$$

In the above equations, E_0 and E_1 are electric fields in the vacuum and the dielectric media, respectively. Their boundary conditions at the interface $z = \xi(x)$ are

$$E_0(\mathbf{r}) = E_1(\mathbf{r}) \tag{2.22a}$$

$$\mathbf{n} \cdot \nabla E_0(\mathbf{r}) = \mathbf{n} \cdot \nabla E_1(\mathbf{r}) \tag{2.22b}$$

where the outward normal vector at the interface is denoted by $\mathbf{n} = (-\zeta, 1)/\gamma$ with $\gamma = \sqrt{1+\zeta^2}$. By virtue of Green's functions at each medium G_0 and G_1, two Helmholtz equations in Equations 2.21 become

$$G_0(\mathbf{r},\mathbf{r}')\nabla^2_{\mathbf{r}'} E_0(\mathbf{r}') - E_0(\mathbf{r}')\nabla^2_{\mathbf{r}'} G_0(\mathbf{r},\mathbf{r}') = 4\pi\delta(|\mathbf{r}-\mathbf{r}'|) E_0(\mathbf{r}') \tag{2.23a}$$

$$G_1(\mathbf{r},\mathbf{r}')\nabla^2_{\mathbf{r}'} E_1(\mathbf{r}') - E_1(\mathbf{r}')\nabla^2_{\mathbf{r}'} G_1(\mathbf{r},\mathbf{r}') = 4\pi\delta(|\mathbf{r}-\mathbf{r}'|) E_1(\mathbf{r}') \tag{2.23b}$$

Green functions are given by the zeroth-order Hankel function of the first kind:

$$G_0(\mathbf{r},\mathbf{r}') = \pi i H_0^{(1)}(k|\mathbf{r}-\mathbf{r}'|) \tag{2.24a}$$

$$G_1(\mathbf{r},\mathbf{r}') = \pi i H_0^{(1)}(\sqrt{\varepsilon_1} k|\mathbf{r}-\mathbf{r}'|) \tag{2.24b}$$

Green's theorem provides four surface integral equations from Equations 2.23, depending on the two position vectors $\mathbf{r}'$ and $\mathbf{r}$. Since the reflected field ($\mathbf{r} \in V_0$) is of interest, only two equations suffice. The first equation expresses the field $E_0(\mathbf{r})$ obtained from the integration over vacuum ($\mathbf{r}' \in V_0$) in Equation 2.23a, resulting in the following surface integral.

$$\frac{1}{4\pi}\int_{S_0} d\mathbf{S}' \cdot \left[G_0(\mathbf{r},\mathbf{r}') \nabla_{\mathbf{r}'} E_0(\mathbf{r}') - E_0(\mathbf{r}') \nabla_{\mathbf{r}'} G_0(\mathbf{r},\mathbf{r}') \right] = E_0(\mathbf{r}), \quad (\mathbf{r} \in V_0) \quad (2.25)$$

The surface surrounding vacuum S_0 can be decomposed into two parts, a upper hemisphere of infinite radius S_∞ and the rough interface $\xi(x)$.

$$\int_{S_0} d\mathbf{S}' = \int_{S_\infty} d\mathbf{S}' + \int_{\xi(x)} d\mathbf{S}' = \int_{S_\infty} d\mathbf{S}' - \int_{\xi(x)} \mathbf{n}\gamma' dx' \quad (2.26)$$

Note that the integral along the rough surface (dS') is related with that along the mean surface (dx') such that $d\mathbf{S}' = -\mathbf{n}\gamma' dx'$. Since the field in V_0 is considered as the sum of incident and reflected fields, i.e., $E_0 = E_i + E_r$, the integral over the upper hemisphere is

$$\int_{S_\infty} d\mathbf{S}' \cdot \left[G_0 \nabla E_0 - E_0 \nabla G_0 \right] = 4\pi E_i \quad (2.27)$$

By the introduction of Equations 2.26 and 2.27, Equation 2.25 becomes

$$E_i(\mathbf{r}) + \frac{1}{4\pi}\int_{-\infty}^{\infty} \gamma' dx' \left[E_0(\mathbf{r}') \frac{\partial G_0(\mathbf{r},\mathbf{r}')}{\partial n'} - G_0(\mathbf{r},\mathbf{r}') \frac{\partial E_0(\mathbf{r}')}{\partial n'} \right] = E_0(\mathbf{r}), \ (\mathbf{r} \in V_0) \quad (2.28)$$

This equation shows the reflected field in vacuum $E_0(\mathbf{r})$ consists of two contributions; one from the incident field $E_i(\mathbf{r})$ and the other from the reflected field $E_r(\mathbf{r})$ that is the integral on the left hand side. Furthermore, this equation is a mathematical expression of Huygens' principle, which states each element of a wave-front may be regarded as the

center of a secondary disturbance which gives rise to spherical wavelets, and the position of the wave-front at any later time is the envelope of all such wavelets [6,35].

On the other hand, the second equation for the field $E_1(\mathbf{r})$ is obtained from the integration over the volume of the dielectric medium V_1. The similar procedure results in an integral equation for the dielectric medium ($\mathbf{r}' \in V_1$). Unlike vacuum, no incidence wave in V_1 exists, and thus the equation equivalent to Equation 2.27 is

$$\int_{S_\infty} d\mathbf{S}' \cdot \left[G_1 \nabla E_1 - E_1 \nabla G_1 \right] = 0 \tag{2.29}$$

As a result, the counterpart to Equation 2.28 is

$$-\frac{1}{4\pi} \int_{-\infty}^{\infty} \gamma' dx' \left[E_1(\mathbf{r}') \frac{\partial G_1(\mathbf{r}, \mathbf{r}')}{\partial n} - G_1(\mathbf{r}, \mathbf{r}') \frac{\partial E_1(\mathbf{r}')}{\partial n} \right] = 0, \quad (\mathbf{r} \in V_0) \tag{2.30}$$

This equation is one of the extinction theorem equations [6]. The coupled equations, Equations 2.28 and 2.30, are used to obtain the reflected fields.

Two unknown surface source functions can be defined for solutions of Equations 2.28 and 2.30, based on the boundary conditions in Equations 2.22.

$$E(x) = E_0(x) = E_1(x) \tag{2.31a}$$

$$F(x) = \gamma \frac{\partial E_0(x)}{\partial n} = \gamma \frac{\partial E_1(x)}{\partial n} \tag{2.31b}$$

When $\mathbf{r}$ approaches to the interface $\xi(x)$, Equations 2.28 and 2.30 can be expressed with E and F

$$E_i(x) + \frac{1}{4\pi} \int_{-\infty}^{\infty} dx' \left[E(x') \left\{ \frac{\partial G_0}{\partial z'} - \xi'(x') \frac{\partial G_0}{\partial x'} \right\} - G_0 F(x') \right] = E(x) \tag{2.32a}$$

$$-\frac{1}{4\pi} \int_{-\infty}^{\infty} dx' \left[E(x') \left\{ \frac{\partial G_1}{\partial z'} - \xi'(x') \frac{\partial G_1}{\partial x'} \right\} - G_1 F(x') \right] = 0 \tag{2.32b}$$

Since the reflected field at a far distance, i.e., $|\mathbf{r}-\mathbf{r}'|\to\infty$ is of interest, the Hankel function can be approximated as $H_0^{(1)}(x)\approx\sqrt{2/\pi x}e^{i(x-\pi/4)}$ for a 1D surface. With the surface profile of a surface realization, the two coupled equations of Equation 2.32 can numerically be solved for E and F in a matrix form. Once E and F are known, the reflected field E_r is obtained from the integration in Equation 2.28.

$$E_r(\mathbf{r})=\frac{e^{i(kr-\pi/4)}}{2\sqrt{2\pi kr}}\int_{-\infty}^{\infty}dx'\left\{k\left[\cos\theta_r-\xi'(x')\sin\theta_r\right]E(x')-iF(x')\right\}e^{-i\mathbf{k}_r\cdot\mathbf{r}'} \quad (2.33)$$

After the ensemble average over many surface realizations, the BRDF ($f_{r,s}$) for *s* polarization according to the definition in Equation 2.2 can be written as

$$\begin{aligned} f_{r,s}&=\frac{\left\langle\left|E_{r,s}\right|^2\right\rangle}{\left|E_{i,s}\right|^2 l\cos\theta_i\cos\theta_r}=\frac{1}{8\pi kl\cos\theta_i\cos\theta_r}\\ &\times\left\langle\left|\Delta x\sum_{n=1}^{N}\left\{k\left[\cos\theta_r-\xi'(x_n)\sin\theta_r\right]E_n-iF_n\right\}e^{\left\{\left[-ik\left[x_n\sin\theta_r+\xi(x_n)\cos\theta_r\right]\right]\right\}}\right|^2\right\rangle \end{aligned} \quad (2.34)$$

For *p* polarization (TM wave), the magnetic field and its derivative replace the electric field and its derivative in Helmholtz equations of Equations 2.21. The source functions for *p* polarization are defined as H and $L=\frac{\gamma}{\varepsilon_1}\frac{\partial H}{\partial n}$ in Equations 2.31. After similar formulation, the equations equivalent to Equations 2.32 for *p* polarization are derived. The expressions for $H_r(\mathbf{r})$ and $f_{r,p}$ corresponding to Equations 2.33 and 2.34 remain the same, except that E and F are replaced with H and L, respectively.

2.4 Approximate Wave Scattering Theory

High complexity in formulation and overwhelming requirement in computation prevent the rigorous approaches from being easily applied to 2D surfaces [9]. Furthermore, analytical approximations are still of great importance not only because of easiness and flexibility for applications but also because of physical insight analytical approximations provide. Two fundamental approximations are the small perturbation method (SPM) and the Kirchhoff approximation (KA) [7]. SPM, often called the Rayleigh or Rayleigh-Rice method, is applicable for surfaces with a small rms roughness with respect to the wavelength of interest [5]. On the other hand, KA, also known as the physical-optics or tangent-plane approximation, is valid for large radii of curvature or locally smooth surfaces [4]. In a short wavelength regime, KA reduces to the geometric-optics or ray-optics approximation (GOA) [12]. Even if GOA and KA predicts different BRDFs, both yield the same reflectance if only first-order scattering is involved [45].

The major drawback for approximate methods is difficulty in precisely determining their validity domains. Many studies have been devoted to identifying the validity domain by comparing with rigorous approaches [11,14,46-49]. Nevertheless, the validity domain does not always give a quantitative criterion to select a proper approximation for various scattering problems. Most validity domains are established for 1D perfectly conducting surfaces with Gaussian surfaces due to the limitations of rigorous approaches. Even for 1D surfaces, enormous computational requirements do not allow rigorous solutions for all ranges of roughness parameters. Furthermore, different studies have established different criterions to determine the validity domain of an

approximation. Therefore, care must be taken when an approximate method is selected to deal with a surface scattering problem.

Despite difficulties in identifying the validity domains, those for SPM, KA, and GOA are illustrated as a rough guideline in Figure 2.3. Given values of roughness parameters do not mean absolute boundaries, but they are useful for relative comparison of each domain. SPM is applicable when the rms roughness is small compared to the wavelength whereas KA is valid for surfaces with large roughness and small steepness. The validity domain of GOA is obtained when multiple scattering is considered, otherwise it is included in that of KA, i.e., $\sigma/\tau < 0.2$. SPM and KA have been improved, and many other approximate methods based on both have been developed [7].

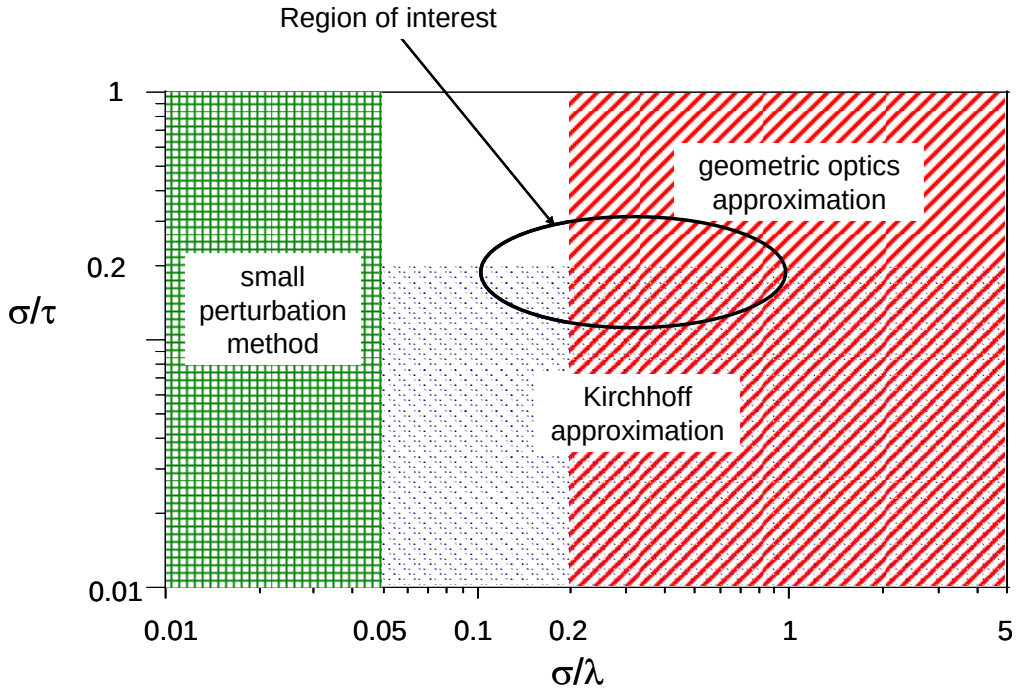

Figure 2.3 Validity domains of approximate methods. In general, the rms roughness of silicon wafers is less than 1μm and their autocorrelation length is several micrometers. The wavelength for radiation thermometry in RTP is recommended to be less than 1μm. Based on the roughness parameters and the wavelength, the region of interest is illustrated.

Approximate methods have been extended to the scattering from surfaces with thin-film coatings as well [50-53]. These improvements and modifications make it difficult to assess the applicability of approximations. Furthermore, the validity domain may depend on more variables such as the incidence angle and the optical constants of a material.

The wavelength recommended for radiation thermometers in RTP is less than 1 μm [22], while roughness parameters of silicon wafers are generally in the order of micrometers or hundreds of nanometers. The values of σ/λ and σ/τ suggest that either KA or GOA should be applicable to modeling silicon surface BRDFs. Therefore, modeling approaches in this thesis largely rely on KA and GOA. Because analytical BRDF models based on GOA can be derived from KA, only the theory of KA is explained in the following. GOA will be explained in Chapter 4 when the Monte Carlo ray-tracing methods are developed.

In KA, the coupled integral equations of Equations 2.32 are not solved to obtain the source functions E and F. Instead, the field at any point of the surface is assumed to be the sum of an incident field and the reflected field that is multiplied with Fresnel's reflection coefficient R of the tangent plane at a considered point. The fields at the tangent plane $E_t(\mathbf{r})$ are therefore given as

$$E_t(\mathbf{r}) = (1+R)E_i(\mathbf{r}) \tag{2.35a}$$

$$\frac{\partial E_t(\mathbf{r})}{\partial n} = i\mathbf{k}_i \cdot \mathbf{n}(1-R)E_i(\mathbf{r}) \tag{2.35b}$$

In KA, calculation of Fresnel's reflection coefficient determines a polarization state.

Because KA can be straightforwardly extended from 1D surfaces to 2D surfaces unlike the boundary integral method, the application for 2D rough surfaces is discussed

below. 2D Green's function for the vacuum $G_0(\mathbf{r},\mathbf{r}') = e^{ik|\mathbf{r}-\mathbf{r}'|}/|\mathbf{r}-\mathbf{r}'|$, and its far-field expressions are

$$G_0(\mathbf{r},\mathbf{r}') \approx \frac{e^{i(kr-\mathbf{k}_r\cdot\mathbf{r}')}}{r} \tag{2.36a}$$

$$\frac{\partial G_0(\mathbf{r},\mathbf{r}')}{\partial n} \approx \frac{-ie^{ikr}}{r}(\mathbf{n}\cdot\mathbf{k}_r)e^{-i\mathbf{k}_r\cdot\mathbf{r}'} \tag{2.36b}$$

With the introduction of Equations 2.36 and the incident field $E_i = e^{i\mathbf{k}_i\cdot\mathbf{r}}$, the reflected field corresponding to Equation 2.33 is

$$E_r(\mathbf{r}) = \frac{ie^{ikr}}{4\pi r}\int\left[\left(R\mathbf{k}^- - \mathbf{k}^+\right)\cdot\mathbf{n}\right]e^{i\mathbf{k}^-\cdot\mathbf{r}'}\mathrm{d}S' \tag{2.37}$$

where $\mathbf{k}^- = \mathbf{k}_i - \mathbf{k}_r$ and $\mathbf{k}^+ = \mathbf{k}_i + \mathbf{k}_r$. KA itself does not provide analytical expressions, and a numerical integration is necessary for evaluating Equation 2.37. Analytical formulae are usually derived with the assumption of constant reflection coefficients for the two cases of Gaussian surfaces: slightly or very rough surfaces. A parameter *g* can be defined as $k^2\sigma^2(\cos\theta_i + \cos\theta_r)^2$ to measure the extent of surface roughness compared to a wavelength.

For a slightly rough surface ($g \ll 1$), both coherent and incoherent components commonly are present. The coherent field can be expressed by

$$\langle E_r \rangle = \frac{-ie^{ikr}}{4\pi r}\left(k_z^+ - Rk_z^-\right)l^2\chi\left(k_z^-\right)\frac{\sin\left(k_x^- l/2\right)}{\left(k_x^- l/2\right)}\frac{\sin\left(k_y^- l/2\right)}{\left(k_y^- l/2\right)} = \chi\left(k_z^-\right)\hat{E}_0 \tag{2.38}$$

where $\hat{E}_0$ signifies the intensity reflected from a smooth surface. Components of the vector $\mathbf{k}^-$ are denoted by k_x^-, k_y^-, and k_z^-. Equation 2.38, therefore, implies that the

coherent field intensity is proportional to the intensity reflected from a smooth surface. On the other hand, the incoherent intensity is

$$\left\langle I_{r,inc} \right\rangle = \frac{l^2 R^2}{4r^2} \left| \mathbf{k}^- \right|^4 P\left(k_x^-, k_y^- \right) \tag{2.39}$$

With the power spectrum in Equation 2.15 and the characteristic function in Equation 2.17 for a Gaussian surface, the sum of coherent and incoherent intensities becomes

$$\left\langle I_r \right\rangle = \left\langle I_{r,coh} \right\rangle + \left\langle I_{r,inc} \right\rangle = \hat{I}_0 e^{-g} + \frac{l^2 \tau^2 \sigma^2 R^2}{16\pi r^2} \left| \mathbf{k}^- \right|^4 \exp\left[-\frac{\left(k_x^- \right)^2 + \left(k_y^- \right)^2}{4} \tau^2 \right] \tag{2.40}$$

where $\hat{I}_0$ means the intensity reflected from a smooth surface.

For very rough surfaces ($g \gg 1$), the coherent component in Equation 2.38 is insignificant, and the incoherent component is dominant. The intensity reflected from a Gaussian surface can be expressed as follows:

$$\left\langle I_r \right\rangle \approx \left\langle I_{r,inc} \right\rangle = \frac{l^2 R^2}{4r^2} \frac{\left| \mathbf{k}^- \right|^4}{\left(k_z^- \right)^4} p_s\left(\frac{k_x^-}{k_z^-}, \frac{k_y^-}{k_z^-} \right) = \frac{l^2 R^2}{8\pi w^2 r^2} \frac{\left| \mathbf{k}^- \right|^4}{\left(k_z^- \right)^4} \exp\left(-\frac{\zeta_x^2 + \zeta_y^2}{2w^2} \right) \tag{2.41}$$

Relations of $\zeta_x = k_x^- / k_z^-$ and $\zeta_y = k_y^- / k_z^-$ are used in Equation 2.41. The reflected field is independent of the wavelength of incidence, which means that KA is reduced to GOA in a short wavelength limit. While the power incident on a 1D surface is $\left| E_i \right|^2 l \cos\theta_i$, that on a 2D surface is $\left| E_i \right|^2 l^2 \cos\theta_i$. Accordingly, the BRDF of a 2D surface is obtained from the relation of $f_r = r^2 \left\langle I_r \right\rangle / \left(\left| E_i \right|^2 l^2 \cos\theta_i \cos\theta_r \right)$.

CHAPTER 3

SAMPLE CHARACTERIZATION AND RADIATIVE PROPERTY MEASUREMENT

This chapter presents basic information about bare silicon wafers. Deposition of gold and silicon dioxide coatings onto the samples and measurement of coating thickness are described. Topography measurement using an AFM is explained. Important roughness statistics calculated from the topography measurements are discussed, with focus on anisotropic features of roughness. An optical scatterometer developed for BRDF measurements in Ref. [54], specifically the three-axis automated scatterometer (TAAS), is introduced. When surfaces possess antireflection coatings, TAAS measurements revealed fluctuation due to small signal-to-noise ratios. Therefore, a procedure to enhance the signal-to-noise ratio is developed. An integrating sphere is adopted for emittance measurements, and its experimental setup connected with monochromatic light sources is described. Based on integrating sphere theory, measurement equation for center-mount configuration is derived.

3.1 Sample Preparation and Roughness Characterization

Two silicon samples (Si-1 and Si-2) were selected from commercial wafers, and they are in the same batch of some wafers studied by Zhu and Zhang [28]. The 100 mm diameter wafers are <100> single crystalline and grown with the Czochralski process. Si-1 is highly pure while Si-2 is lightly boron-doped (*p*-type). Basic information about the two bare silicon samples is listed in Table 3.1. Si-1 and Si-2 were diced into 25 × 25 mm^2

square pieces. Two gold samples (Au-1 and Au-2) were prepared by depositing a gold film with an e-beam evaporator (CVC SC 5000), and deposition was conducted onto each piece of Si-1 and Si-2 at the same time. A quartz crystal microbalance monitor displayed the film thickness during deposition within 10% relative uncertainty. A 20 nm thick titanium film was deposited directly onto the silicon substrate to prevent the gold film from peeling off, and then an approximately 100 nm thick gold film was deposited.

Similarly, the rough sides of Si-1 and Si-2 were coated with silicon dioxide films by a plasma-enhanced chemical vapor depositor (PECVD). Rough surfaces were simultaneously placed into a deposition chamber together with several small pieces of smooth silicon surfaces so that the same coating thickness was deposited to different specimens. The same procedure was repeated with different deposition time to obtain three different coating thicknesses. Coating thicknesses were measured at 20 different points on the reference samples with a Nanospec 3000 optical profilometer made by Nanometrics Inc. This optical profilometer measures the reflectance in a wavelength range from 400 to 800 nm, and the measured reflectance is fitted with an analytical

Table 3.1 Basic information about silicon wafers.

Sample	Si-1	Si-2
Crystalline orientation	<100>	<100>
Growth method	Czochralski	Czochralski
Doping type	P	P
Resistivity, Ω·cm	4310 - 6970	10 - 40
Thickness, μm	525	500

formula by adjusting the phase shift between the two return beams: one from the film-substrate interface and the other from the air-film interface. Coating thickness can be determined using the measured phase shift of the reflected light once film refractive index is known. The measured silicon dioxide coating thicknesses are 107.2 ± 0.3 nm, 216.5 ± 0.5 nm, and 324.6 ± 2.1 nm, with a reproducibility of 0.2 nm.

As mentioned in Section 2.2, a surface profile $\xi(\mathbf{r})$ is required for calculation of statistical distribution functions and roughness parameters. Zhu and Zhang demonstrated that an optical interferometric profilometer is not suitable for silicon surface roughness and measured topography using an AFM in the contact mode with silicon nitride tips, whose radius is less than 60 nm [28]. In the contact mode, however, lateral or shear forces can distort surface features and reduce spatial resolution. Thus, deep valleys may not be correctly measured, resulting in spurious distributions for precipitous slopes. In the present work, the tapping mode with silicon-based cantilevers that have a sharper tip radius around 10 nm was employed to measure precipitous slopes. At the expense of scanning speed, an AFM in the tapping mode with sharper tips allows measurement of precipitous slopes. Driving frequencies were set to 95% of mechanical resonance frequency of the cantilevers around 170 kHz, and scan rates along a line were set to 0.15 Hz to achieve a good piezo-control of AFM. Meanwhile, according to the instrument specifications, AFM measurement uncertainty of is estimated to be 3% both vertically and horizontally.

In topography measurement for BRDF modeling, a scan area should be much greater than the autocorrelation length, and a lateral resolution should be much smaller than the autocorrelation length [27,28,55]. Roughness statistics obtained from small area

Table 3.2 Roughness statistics of bare silicon surfaces.

Sample	Si-1	Si-2
σ, μm	0.51 ± 0.03	0.63 ± 0.04
w (along row/column)	0.28 ± 0.01	0.47 ± 0.04
w (along diagonals)	0.28 ± 0.01	0.47 ± 0.04
τ, μm (along row/column)	4.4 ± 0.4	3.1 ± 0.2
τ, μm (along diagonals)	4.3 ± 0.4	3.1 ± 0.2

topographic data do not describe an actual surface, and a bad resolution does not capture roughness features correctly. Besides, the geometric-optics approximation assumes that roughness features are sufficiently larger than the incident wavelength and ignores wave effects due to small features, suggesting that a lateral resolution can be comparable to the wavelength of interest. Since the autocorrelation length of silicon wafer roughness is in the order of several micrometers and the wavelength less than 1 μm is of interest in the present study, a 100×100 μm^2 area scanned in a <110> direction was stored in a 512×512 array.

Rough surfaces, Si-1 and Si-2, were characterized with an AFM made by Digital Instruments (Dimension 3100 SPM). The surfaces of Si-1 and Si-2 were scanned five times each and roughness statistics were calculated with five topographic data. The height distribution functions (HDF) of the two samples are presented in Figure 3.1. Both HDFs look very similar to each other and resemble a Gaussian function although they have small negative values of skewness. The negative skewness indicates that the silicon samples possess a larger number of deep valleys and a smaller number of high peaks than

Gaussian surfaces. The rms roughnesses of Si-1 and Si-2 are 0.51 μm and 0.63 μm, respectively, indicating that Si-2 is rougher than Si-1 (refer to Table 3.2). The HDFs of the two samples obtained in Figure 3.1 are very similar to those in the previous work [28].

The slope distribution functions (SDF) and their contour plots for Si-1 and Si-2 are plotted in Figure 3.2. Both SDFs are non-Gaussian and anisotropic while the anisotropy of Si-1 is not as striking as that of Si-2. The SDF of Si-1 in Figure 3.2a shows only one dominant peak at the center, which implies that a large number of microfacets are slightly tilted. The SDF of Si-2 also has a dominant peak at the center, though smaller than that of Si-1. Moreover, four large side peaks at $|\zeta_x| \approx |\zeta_y| \approx 0.36$, and three small side peaks at $|\zeta_x| \approx |\zeta_y| \approx 1.09$ appear in Figure 3.2b. The contour plot clearly shows the three small side peaks although one is very small and not resolved in the contour plot. Zhu and Zhang [28] demonstrated that the large and small side peaks are respectively associated with the formation of {311} and {111} planes during chemical etching in (100) crystalline wafers. Their measurement did not distinctly resolve the small side

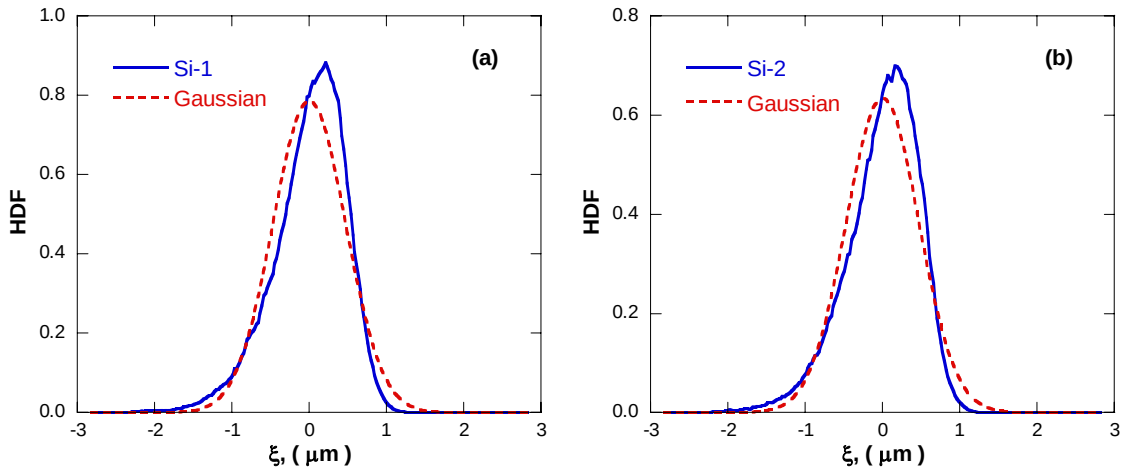

Figure 3.1 Height distribution functions of Si-1 and Si-2 and Gaussian height distribution functions with the same rms roughness. (a) Si-1; (b) Si-2.

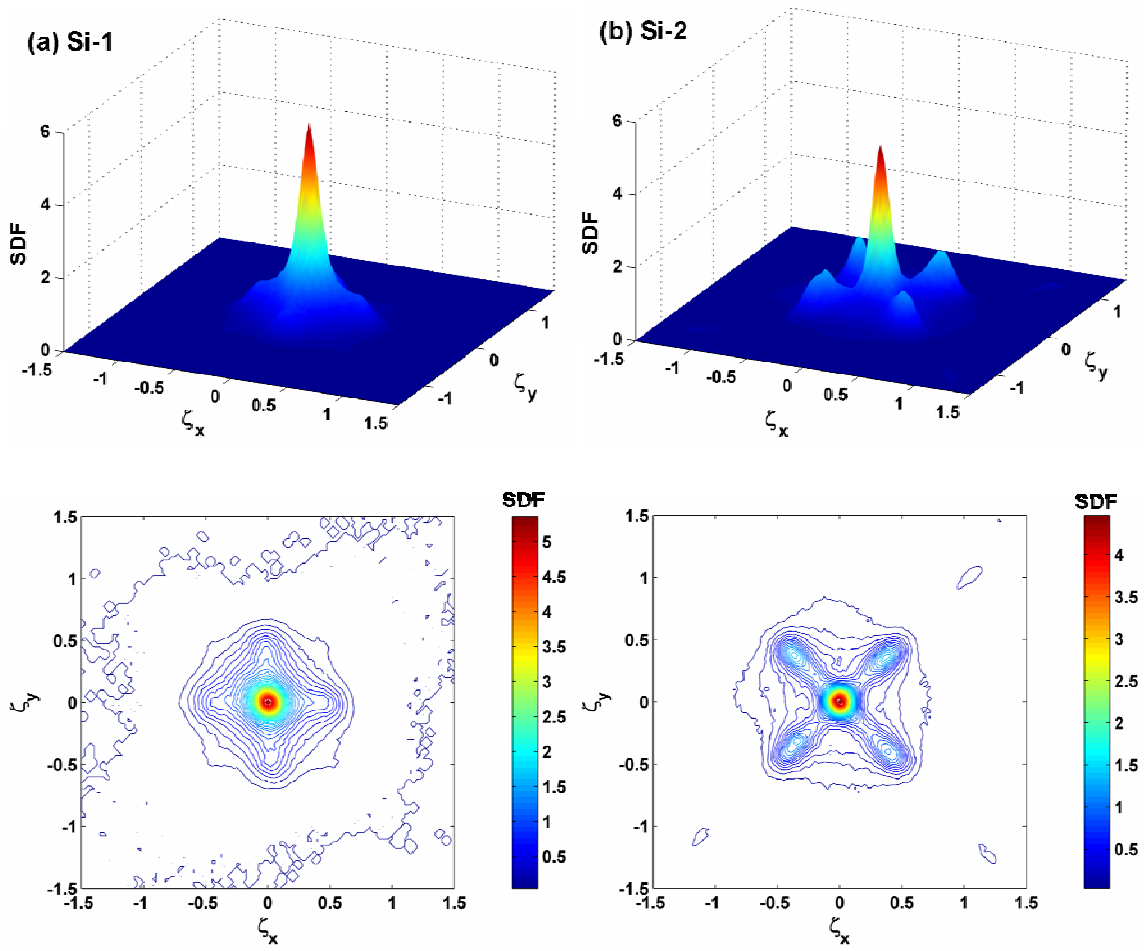

Figure 3.2 2D slope distribution functions in 3D plot (upper) and contour plot (lower). (a) Si-1; (b) Si-2.

peaks due to the artifacts of AFM measurements, but the new measurement in Figure 3.2b clearly reveals the small side peaks. The large and small side peaks in the SDF correspond to microfacets with inclination angles of 27.1° and 57.0°. According to crystallography of silicon, the angles formed by {311} and {111} planes with respect to the (100) surface are 25.2° and 54.7°. The large and small side peaks should appear at $|\zeta_x| = |\zeta_y| = 0.33$ and $|\zeta_x| = |\zeta_y| = 1.0$ in SDF. These values are smaller than the slopes and angles obtained from the AFM measurements. The differences in peak slopes are larger than the 3% uncertainty in the AFM measurements. The resolution may not be good enough to measure actual surface topography. Various artifacts, such as tip convolution due to finite tip sizes and various tip shapes, or tip sliding in the tapping mode may be responsible for the differences as well [56,57].

The 2D autocorrelation functions (ACF) of Si-1 and Si-2 were calculated. Based on the four-fold symmetry of Si-1 and Si-2, as shown in Figure 3.2, ACF cross sections along row ($x = 0$) and column ($y = 0$) are averaged and presented in Figure 3.3. In the same fashion, cross sections along two diagonals ($x = y$ and $x = -y$) appear in Figure 3.3. Therefore, "row/column" and "diagonals" in the legend signify $\phi = 0°$ and $\phi = 45°$ on the mean plane, respectively. As the distance along a given direction *r* increases, the ACFs decay from 1 at the origin. Although the SDFs of the two samples reveal anisotropy in Figure 3.2, the ACFs do not show noticeable anisotropy. A horizontal bar in Figure 3.3 represents a value of 1/*e* so that intersection points with the ACF indicate the autocorrelation length τ. As shown in Table 3.2, the autocorrelation length of Si-1 is larger than that of Si-2, the autocorrelation lengths depend little on the scanning direction or the azimuthal angle. As the rms slope *w* of Si-2 is larger than that of Si-1, $\sqrt{2}\sigma/\tau$

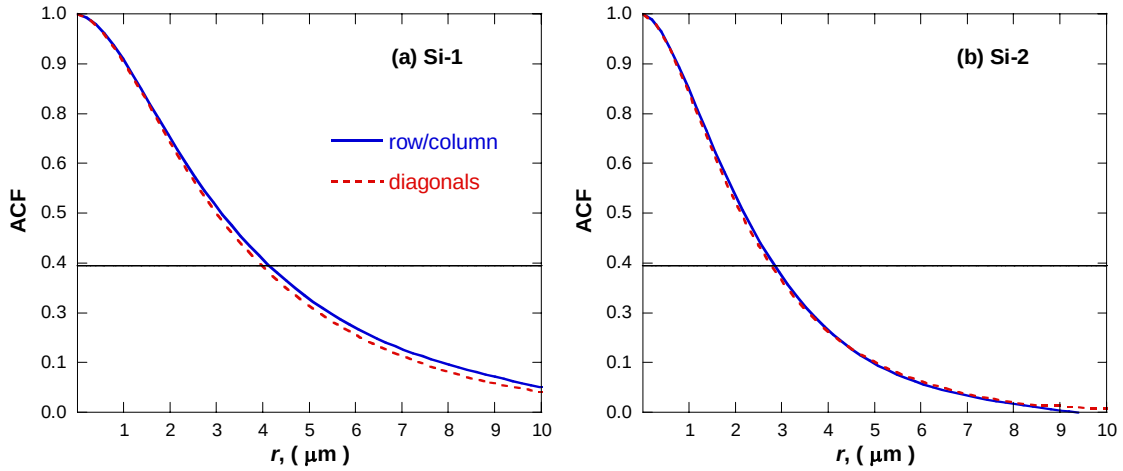

Figure 3.3 Autocorrelation functions along row and column directions or two diagonal directions. (a) Si-1; (b) Si-2. Horizontal lines indicate the value of 1/*e* so that the intersection with the autocorrelation function is the autocorrelation length.

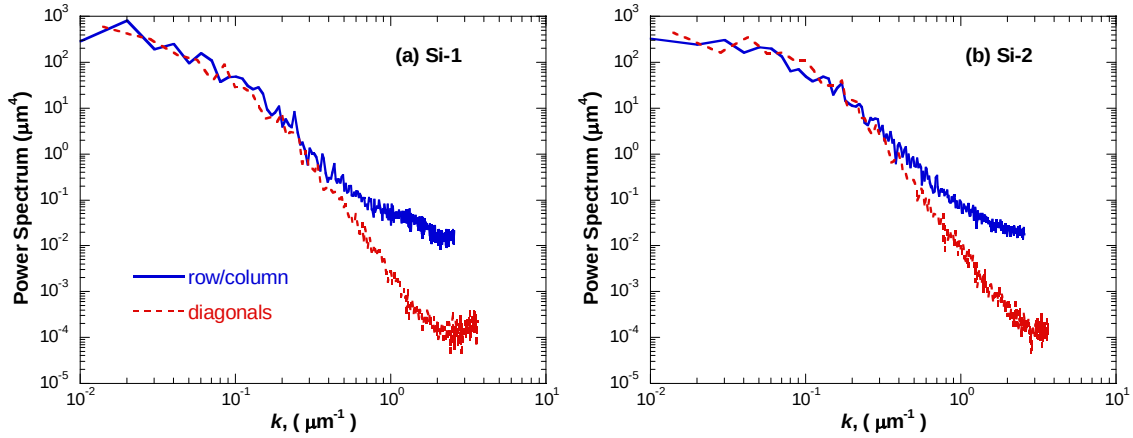

Figure 3.4 Power spectra along row and column directions or two diagonal directions. (a) Si-1; (b) Si-2.

value of Si-2 is also larger even though the equality of $w = \sqrt{2}\sigma/\tau$ that a Gaussian surface follows does not hold.

Figure 3.4 illustrates power spectrum cross sections of Si-1 and Si-2, which were obtained from the similar average calculation as in Figure 3.3. Unlike other statistical distribution functions, the power spectrum curves in Figure 3.4 fluctuate more severely. It seems that more surface topography measurements are necessary for the power spectrum. At small wave numbers *k*, anisotropic features of the power spectrum for both samples are not significant. However, at large wave numbers, both power spectra strongly depend on the scanning direction. Interestingly, the power spectrum of Si-1 also reveals strong anisotropy, which is not distinguishable from anisotropy in the power spectrum of Si-2.

Since the gold samples were made by depositing thin films onto the bare silicon surfaces, it is expected that the SDF does not change much before and after deposition. Topography measurements of Au-1 and Au-2 were obtained with the same AFM two times each. Because roughness parameters do not depend on the scanning direction

Table 3.3 Coating thickness and roughness statistics of coated surfaces.

Sample	Coating material	Coating thickness, μm	σ, μm	*w*	τ, μm
Si-1	Au	100	0.50	0.29	4.0
	SiO_2	107.2 ± 0.3	N/A	N/A	N/A
	SiO_2	216.5 ± 0.5	0.52	0.28	4.1
	SiO_2	324.6 ± 2.1	0.51	0.28	4.5
Si-2	Au	100	0.65	0.50	3.0
	SiO_2	107.2 ± 0.3	N/A	N/A	N/A
	SiO_2	216.5 ± 0.5	0.65	0.50	3.1
	SiO_2	324.6 ± 2.1	0.69	0.52	3.1

significantly, only the average roughness statistics are listed in Table 3.3. The HDF or SDF of Au-1 and Au-2 dose not change noticeably from the HDF or SDF of Si-1 and Si-2. The increase of w and the decrease of τ for Au-1 and Au-2, compared to those of Si-1 and Si-2, imply that the 100 nm thick gold coating roughens bare silicon surfaces. However, roughness parameters of gold-coated surfaces are within standard deviations of the bare silicon surface measurements. Accordingly, it is assumed that Si-1 and Au-1 or Si-2 and Au-2 have the same surface statistics despite the presence of gold coating.

Because the roughness statistics of approximately 100 nm thick gold coatings are essentially the same as those of bare substrates, only silicon surfaces with 216.5 and 324.6 nm thick silicon dioxide coatings were measured three times each. Table 3.3 summarizes averaged roughness parameters of coated surfaces. Since $\sigma = 0.51 \pm 0.03$ and $w = 0.28 \pm 0.01$ for bare Si-1 in Table 3.1, a uniform coating thickness is a good assumption for Si-1 when $h = 216.5$ nm and $h = 324.6$ nm. However, the averaged σ and w of Si-2 seem to increase gradually with coating thickness h. When $h = 216.5$ nm, the values of σ and w are within their ranges for bare Si-2 ($\sigma = 0.63 \pm 0.04$ and $w = 0.47 \pm 0.04$). However, when $h = 324.6$ nm, the values of σ and w are slightly larger than those for bare Si-2, respectively.

3.2 Optical Scatterometer for BRDF Measurement

Instruments for BRDF measurement are usually called as optical scatterometer or reflectometer. Different types of optical scatterometers are available for various industry and research applications [58-60]. Although system configuration changes depending on the purpose of instruments, optical scatterometers have several essential components such

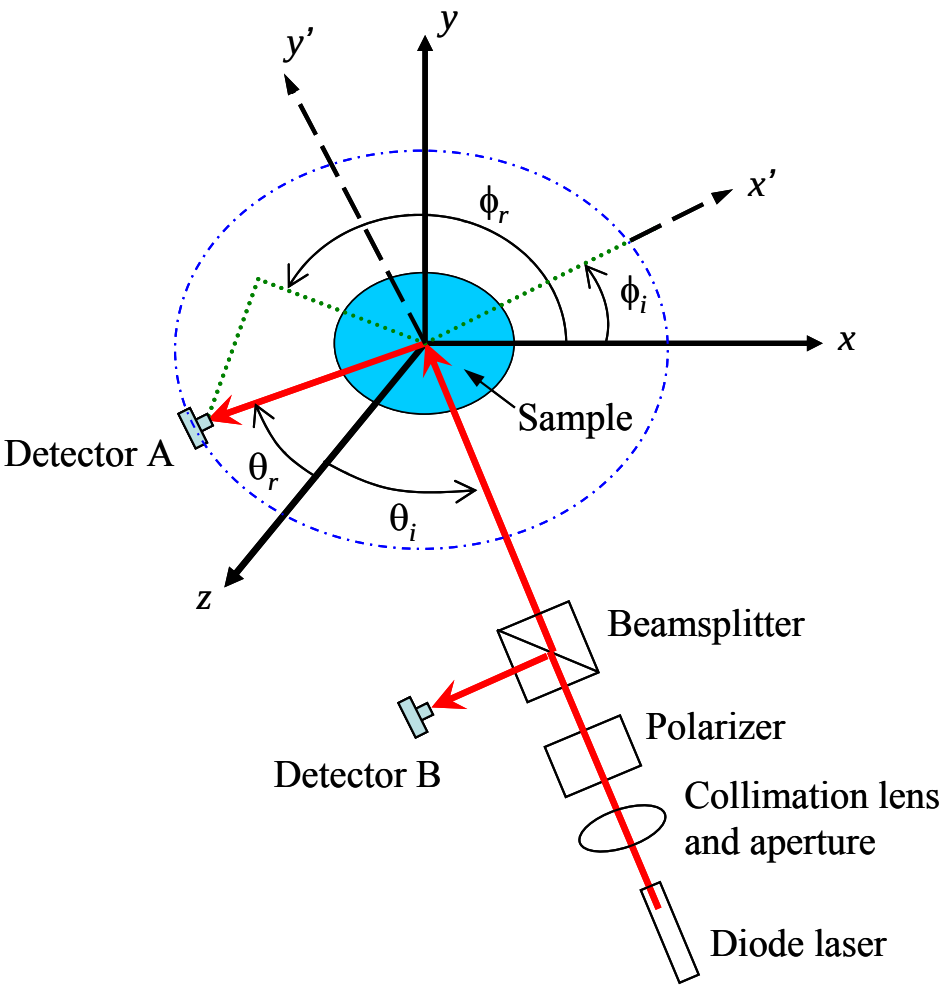

Figure 3.5 Schematic of the TAAS. Here, a sample is vertically mounted, and the laser beam is parallel to the optical table, which is in the *x*-*z* plane. Rotation of the sample around the *y* axis changes θ_i, and rotation of detector A in the *x*-*z* plane changes θ_r. ϕ_i can be changed by rotating the sample around the *z* axis.

as goniometric table, light source, detector, and data acquisition system. Among several instruments, the Spectral Tri-function Automated Reference Reflectometer (STARR) at the National Institute of Standards and Technology (NIST) is a high-accuracy reference instrument for the in-plane BRDF measurement in the visible and near-infrared regions [58]. Although STAAR is a reference reflectometer, it cannot measure the out-of-plane BRDF because of only two rotary stages available. In other words, it is impossible to investigate the dependence of light scattering on azimuthal angles with STAAR. This type of scatterometer cannot be applied for anisotropic surfaces.

In the present work, the TAAS is used for BRDF measures [54], and Figure 3.5 illustrates its optical setup. A sample is vertically mounted, and three rotary stages, automatically controlled by a computer, are used to change incidence and reflection directions. One rotates the sample around the *y* axis to change the incidence angle θ_i, another rotates detector A in the *x*-*z* (horizontal) plane to change the reflection angle θ_r, and the third rotates the arm of detector A out of the *x*-*z* plane to change the azimuthal angle ϕ_r. Manual rotation of the sample on a sample holder around the *z* axis adjusts the azimuthal angle ϕ_i. The incident laser beam is parallel to the optical table (*x*-*z* plane). A diode laser system serves as an optical source, and a lock-in amplifier connected with a diode laser controller modulates the output optical power at 400 Hz. The diode laser is mounted on a thermoelectrically controlled stage to provide power stability within a standard deviation of 0.2%. An optical fiber is used to provide flexibility for optical access and alignment. The light from the output end of the fiber is in the horizontal plane.

The beam first passes through a collimator with a pair of lenses and a small aperture. A linear polarizer mounted on a dial allows the selection of polarization for

light incident on the sample. The beamsplitter then divides the laser beam into two passes: one goes to the sample and the other to a stationary reference detector B. The light scattered by the sample is measured by detector A. The power collected at each detector is sent to two trans-impedance pre-amplifiers with nine decades of amplification range. The pre-amplifier has a linear frequency response from DC up to a certain maximum frequency that is much greater than 400 Hz. The lock-in amplifier only picks up the phase-locked signals at 400 Hz, thereby eliminating background radiation or stray light effects without using a chopper. The measurement equation for the TAAS is

$$f_r\left(\theta_i, \phi_i, \theta_r, \phi_r\right) = C_I \frac{V_A}{V_B \cos\theta_r \Delta\omega_r} \tag{3.1}$$

where V_A and V_B are outputs of detectors A and B, respectively, and the reflection solid angle $\Delta\omega_r$ is 1.84×10^{-4} sr as determined by the area of a precision-machined aperture in front of the detector and the distance between this aperture and the beam spot on the sample. An instrument constant C_I compensates a beamsplitter ratio and sensitivity difference in the two detectors. The BRDF within ±2.5° of the retroreflection direction ($\theta_r = \theta_i$ and $\phi_r = \phi_i$) cannot be measured since the movable detector blocks the incident beam. In all BRDF measurements, V_A and V_B are averaged over ten consecutive measurements at a given position to reduce the random error. The relative uncertainty of the TAAS is estimated to be 5% for the BRDF greater than 0.01 by intercomparison with a reference standard instrument [54].

Although a diode laser serves as a stable light source with the rms power fluctuation less than 0.2% [54], it may not be suitable for measuring the BRDF of surfaces with antireflection coatings because of its small power. The output power from the diode laser after the connected optical fiber is usually less than 2 mW. The

collimation lens and aperture reduce the optical power by approximately 50%. The beamsplitter has a transmittance of near 50%. The polarizer has a transmittance of 20% for incidence that is randomly polarized or linearly polarized at 45° with respect to the selected polarization (0° and 90° for *p* and *s* polarization, respectively). In previous measurements, the power reaching a sample could be as low as 0.05 mW for a certain polarization. Because surfaces with SiO_2 coatings have a much smaller reflectance than the uncoated Si surfaces due to the reduction of reflectance by a low coating refractive index, similarly to the antireflection effect [61], the reflected power reaching detector A can be very low. If the signal is too weak compared to the noise level, the measurement standard deviation can be very large, resulting in random fluctuations in the BRDF values. As an example, Figure 3.6 shows the measured BRDF of Si-1 coated with a SiO_2 film of $h = 107.2$ nm at normal incidence for *s* polarization. In the earlier measurement,

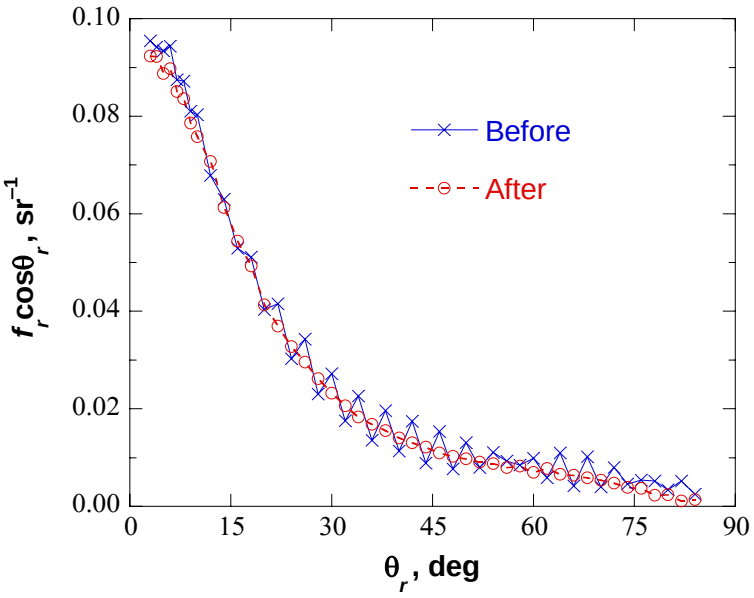

Figure 3.6 Effectiveness of the procedure to improve the signal-to-noise ratio for BRDF measurements. The BRDF of Si-1 with 107.2 nm thick SiO_2 coating is presented. Before: measurements taken earlier without applying the procedure; after: results after reduction of the standard deviation.

the measured BRDF value fluctuated when $f_r \cos\theta_r$ was less than 0.04 due to the large standard deviation. A procedure was developed to enhance the signal level in the measurements of small BRDFs as explained below [62].

In earlier measurements, the gain of pre-amplifiers was set to be the same for all θ_r values. In order to take full advantage of pre-amplifiers' dynamic range, manual adjustment is necessary for large θ_r when the reflected power is small. The gain ratio has been carefully calibrated and shown to be linear. The use of a large gain can provide sufficient signal to the lock-in amplifier, which will filter out the noise from the phase-locked signal. Notice that the diode laser output is linearly polarized, but the orientation of polarization at the end of an optical fiber depends on how the fiber is positioned. Therefore, the linear polarizer is essential to provide either *s*- or *p*-polarized light to the sample. When the polarization of the diode laser is parallel to that of the polarizer, the output power is maximized for a given polarization but minimized for the other. In previous measurements, an effort was made to position the fiber such that the power reaching the sample would be approximately equal when the linear polarizer is rotated between 0° and 90° to switch the polarization state. In the present work, however, the laser power is maximized for individual polarization by repositioning the optical fiber each time when the polarizer is rotated. It should be emphasized that the polarization state of the laser coming out from the fiber affects the signal-to-noise ratio but does not affect the actual polarization of the light reaching the sample. Once the fiber position is fixed, the laser output is very stable in terms of both the power and polarization. Furthermore, the original beamsplitter with a transmittance of about 50% was replaced with one that has a transmittance greater than 90%. The signal-to-noise ratio

improvement, by properly selecting the pre-amplifier gain and optimizing the optical efficiency of the laser power to the sample, has resulted in a much lower standard deviation, which is approximately 10% when $f_r \cos\theta_r = 0.001$, as can be seen from Figure 3.6. Further investigation confirmed that the relative standard deviation is less than 1% when $f_r \cos\theta_r > 0.01$ and less than 10% when $f_r \cos\theta_r > 0.001$.

3.3 Integrating Sphere for Emittance Measurement

The TAAS enables BRDF measurements over the whole hemisphere so that emittance can be calculated from the measured BRDF. However, such a large amount of measurements is practically not feasible. Therefore, an integrating sphere is used for reflectance measurements in a wavelength region from 400 to 1000 nm, and the emittance is deduced from the measured reflectance based on Kirchhoff's law. Figure 3.7 shows the experimental setup for spectral radiative property measurements with a custom-designed integrating sphere from Sphere Optics, Inc. [63]. The inner wall of the 200-mm-diameter sphere is coated with polytetrafluoroethylene (PTFE), which is a nearly diffuse material with a reflectance of approximately 0.99 in the wavelength region of interest [64]. A center-mount scheme was adopted in the present work for emittance measurements at different incidence angles [65,66]. The entrance aperture has a diameter D_e = 25 mm. A silicon detector was mounted at the bottom of the sphere with a baffle in front of it to block radiation directly from the sample. The sample can be rotated out of the beam path for reference measurement, in which light hits the back sphere wall. Sample measurement can be taken after it is confirmed that all light hits the sample

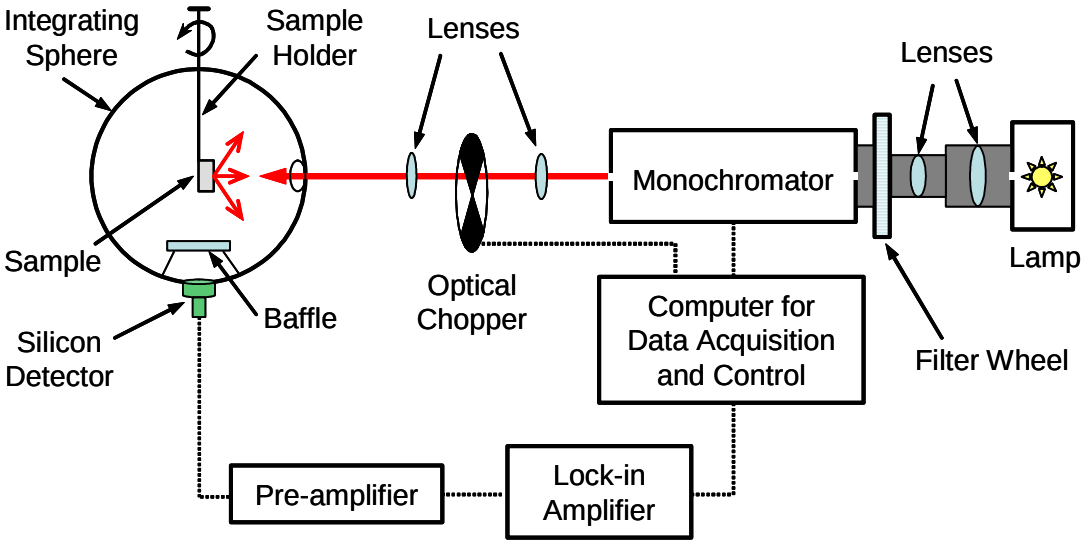

Figure 3.7 Schematic of the setup for spectral radiative property measurements. The light source consists of a tungsten halogen lamp, a filter wheel, and a monochromator. The light exiting the aperture of the monochromator is focused to a sample mounted in the middle of an integrating sphere. The light reflected by sphere walls is collected by a silicon detector located at the bottom of the sphere under a baffle, which prevents direct reflection from the sample to the detector.

surface. The ratio between reference and sample measurements allows the deduction of reflectance as will be discussed later.

A monochromator (Oriel Instruments Cornerstone 130) with a tungsten halogen lamp serves as the light source in a wavelength region from 400 to 1000 nm. The rms power fluctuation of the monochromator is less than 1%. Two lenses inside light shields focus the emission from the lamp on the monochromator entrance slit, and the light from the exit slit has 130 mm focal length. A 1200 lines/mm grating provides a resolution of 10 nm at the 500 nm wavelength when combined with 1.56 mm wide entrance and exit slits. In order to reduce beam dimension, the exit slit was blocked on its upper and lower parts to confine a vertical opening to approximately 3.1 mm. Light passing a collimating lens, which has 25 mm diameter and 100 mm focal length, and a chopper is refocused to the sample by a second lens with 250 mm focal length. The beam spot size on the sample is approximately 5×10 mm^2. The chopper is synchronized to a lock-in amplifier (EG&G 7265DSP) at 400 Hz. A thermoelectrically-cooled diode laser at 635 nm wavelength is also used for emittance measurements at different incidence angles because of its small beam size (3 mm diameter). Furthermore, the diode laser provides higher and more stable optical power than the monochromator connected with a lamp, resulting in noise reduction. The incidence angle is determined by manual rotation of the sample holder. A lock-in amplifier is connected to a diode laser controller to modulate the frequency electrically without the chopper. A linear polarizer can be placed between the diode laser and the integrating sphere to measure the reflectance for *p* or *s* polarization individually.

The incident light undergoes multiple reflections inside the sphere, and a part of reflected power reaches the silicon detector. Then, the detected signal is sent to the lock-

in amplifier, while passing through a trans-impedance pre-amplifier with a wide amplification range. The pre-amplifier is optimized to amplify signals to the working range of the lock-in amplifier so that the lock-in amplifier efficiently selects the phase-locked signals and filters out noises. Additional information about the diode laser system and electronics is described in Ref. [54]. Both data acquisition from the lock-in amplifier and monochromator operation are digitally controlled under a LabView environment.

With sample and reference measurements, reflectance calculation of an opaque sample is based on integrating sphere theory, which is predicated on two basic assumptions: first, that the integrating sphere interior is a perfect sphere; and second, that the interior sphere coating is perfectly diffuse [66,67]. When the incident beam with a radiant power Φ_i hits the sphere wall, the radiant power that reaches the detector after multiple reflections inside the sphere is

$$\Phi_w = \frac{F\mathcal{R}_w}{1-\bar{\mathcal{R}}_w}\Phi_i \tag{3.2}$$

where $\mathcal{R}_w$ and $\bar{\mathcal{R}}_{\mathrm{w}}$ represent the sphere wall reflectance and the average sphere wall reflectance, respectively. The view factor from the sphere wall to the detector is denoted by F, which is $D_d^2 / 4D_{sp}^2$ in terms of detector and sphere diameters if baffle, sample, and entrance aperture effects are neglected.

When the light is incident on the sample, the first reflection has a larger chance to escape from the entrance aperture. It is absolutely necessary to tilt the sample if the surface is smooth or has a large reflection peak. Even if the sample reflects diffusely, the view factor from the sample to the aperture is roughly four times greater than that from the wall to the aperture because the sample is mounted at the center. With an assumption

that sample rotation does not affect the average sphere wall reflectance $\bar{\mathcal{R}}_w$ and the view factor from the wall to the detector F, the total radiant power that reaches the detector for sample measurement is

$$\Phi_s = \frac{F\mathcal{R}_s(1-\eta)\mathcal{R}_w}{1-\bar{\mathcal{R}}_w}\Phi_i \tag{3.3}$$

where $\mathcal{R}_s$ is the sample reflectance of and η is light fraction leaving the sample directly to the entrance aperture. The term of $(1-\eta)\mathcal{R}_w$ equals to the average wall reflectance that receives the first reflection from the sample. Although it is common practice to ignore the baffle, its effect is considered only for the first reflection in the derivation of Equation 3.3: the first reflection from the sample does not reach the detector [67].

If the detector sensitivity is independent of direction and incoming radiant power, the output signal will be proportional to the incoming power. From Equations 3.2 and 3.3, the detector output ratio is related with the sample reflectance $\mathcal{R}_s$ by

$$\frac{V_s}{V_w} = \frac{\Phi_s}{\Phi_w} = (1-\eta)\mathcal{R}_s \tag{3.4}$$

which is the measurement equation of the integrating sphere used in the present work. Theoretically, the correction factor can be calculated from the BRDF f_r.

$$\eta = \frac{\int_{\omega_e} f_r(\theta_i,\phi_i,\theta_r,\phi_r)\cos\theta_r d\omega_r}{\int_{2\pi} f_r(\theta_i,\phi_i,\theta_r,\phi_r)\cos\theta_r d\omega_r} \tag{3.5}$$

The numerator represents the directional-conical reflectance from the sample towards the solid angle of the entrance aperture ω_e, while the denominator is the sample reflectance, as shown in Equation 2.3. For a finite beam size, Equation 3.5 needs to be integrated over the illuminated area as well, which is not done in the present study for simplicity. If a

sample is specular and tilted to hit the wall rather than the aperture, $\eta = 0$ and no correction is needed. For a diffuse sample, η is reduced to the view factor from the sample to the entrance aperture as $\eta = D_e^2 \Big/ \left(D_e^2 + D_{sp}^2 \right) = 0.015$. The samples of interest are however neither specular nor diffuse, and correction factor calculation from a known sample BRDF is necessary. When sample emittances are compared in Chapter 8, correction factor calculation will be explained.

Although the derivation of Equation 3.4 is based on opaque samples, this measurement equation can be used for emittance measurements of semitransparent materials by replacing the right side of Equation 3.4 with $(1-\eta)\mathcal{R}_s + \mathcal{T}_s = \mathcal{R}_s + \mathcal{T}_s - \eta'$, where $\eta' = \eta \mathcal{R}_s$ is a new correction factor that equals to the numerator of Equation 3.5. Accordingly, the detector output ratio gives the sum of reflectance and transmittance. The emittance can be calculated according to Kirchhoff's law in Equation 2.4.

CHAPTER 4

DEVELOPMENT OF MONTE CARLO RAY-TRACING METHODS

This chapter begins with introduction of GOA, on which Monte Carlo ray-tracing methods are based. Two ray-tracing techniques can be distinguished by how to simulate rough surfaces: the surface generation method (SGM) [16,68] and the microfacet slope method (MSM) [38,69]. The Monte Carlo ray-tracing method generally refers to SGM, and basic algorithm of SGM is summarized. MSM was proposed to simulate surface roughness in terms of the normal vector of microfacets so that wafer transmittance can be modeled [38]. However, MSM must be developed further in order to obey the reciprocity principle and agree with analytical BRDF models for first-order scattering. A weight function is introduced to the SDF to correct MSM. Furthermore, the validity domain of MSM is identified by the comparison with SGM and the rigorous approach presented in Section 2.3. Finally, microfacet reflectivity calculation is modified in ray-tracing algorithms to take the change of polarization states, i.e., depolarization into account.

4.1 Geometric-Optics Approximation and Surface Generation Method

Although the analytical BRDF formula in GOA can be derived from KA as shown in Equation 2.41, it does not capture fundamental characteristics of GOA. In a short wavelength limit $\lambda \to 0$, Maxwell's equations are reduced to an equation that defines a constant optical path, and surfaces of a constant optical path form geometrical wave-fronts [35]. The propagating direction of waves is normal to the wave front, and a geometrical concept of light ray describes physical laws. Based on GOA, therefore, ray-

tracing methods have been widely used for many radiative and optical problems when the characteristic length scales are sufficiently larger than the wavelength of interest. Ray-tracing methods can be applied for surface scattering problems when a rough surface is regarded as an aggregate of small and smooth surfaces, called as microfacets. As shown in Figure 4.1, incident rays are directed towards evenly spaced nodes $[x_i, 0]$ at a mean plane $\xi(x) = 0$, but they intersect with the rough interface at a point different from the target point. The intersection point is numerically determined with the geometry of a rough surface profile $z = \xi(x)$ and the wavevector of incident rays. At the intersected microfacet, the incident ray is specularly reflected. Upon the reflection, the energy of every incoming ray is reduced by the microfacet reflectivity, which refers to the reflectivity calculated at a local coordinate system of microfacets. With a large number of rays being traced, radiative properties are calculated from an algebraic sum of the ray energy.

In GOA, ray tracing is performed theoretically or numerically without considering wave interference effects. Theoretical ray-tracing results in the expression in Equation 2.41, which allows convenient BRDF calculation. However, most analytical models deal

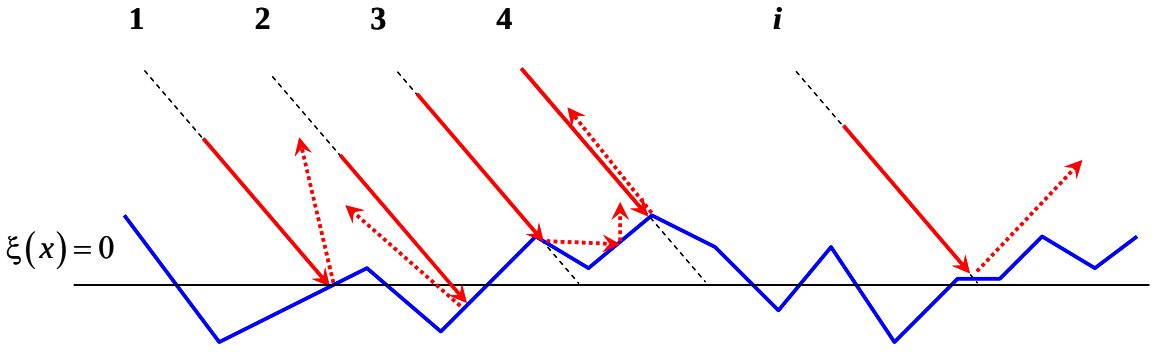

Figure 4.1 Ray tracing between microfacets. Based on GOA, a rough surface is assumed to be comprised of small and smooth surfaces called microfacets.

with first-order scattering only. Although some analytical expressions deal with multiple scattering, additional assumptions are made and the model cannot fully capture the characteristics of multiple scattering [12,17]. Multiple scattering becomes significant for surfaces with large slopes or for large angles of incidence or reflection. Even for first-order scattering, moreover, some analytical BRDF models do not satisfy the energy conservation. For instance, a perfectly reflecting surface reflectance is not equal to unity.

The Monte Carlo method, on the other hand, numerically traces a large number of rays until each ray leaves a rough surface. The surface realization, usually with the spectral method described in Section 2.2, is required in advance. A surface realization provides the physical location and orientation of the microfacet that an incoming ray strikes, and accordingly the origin and direction of reflection can be determined. This common ray-tracing method refers to SGM. Because all the incident ray bundles are considered, the conservation of energy is inherently observed. SGM also allows the complete treatment of multiple scattering [16,38,47,68], which distinguishes GOA from other approaches. The rigorous solution of Equations 2.32 includes multiple scattering, but it does not separate first-order scattering and multiple scattering from total scattering. KA in Equation 2.37 accounts for only first-order scattering. Multiple scattering in KA is modeled from a viewpoint of GOA by the use of a geometrical shadowing function or a surface realization.

4.2 Microfacet Slope Method

If SGM is applied for modeling wafer transmittance, numerically generated surface length should be much larger than wafer thickness, which is not feasible.

Therefore, Zhou and Zhang [38] developed MSM to model radiative properties of semitransparent wafers. For modeling the transmittance, rays must be traced inside a material as well as between microfacets. MSM takes advantage of a basic concept of GOA; for an incoming ray, only the normal vector of a microfacet determines the ray reflection direction and the reflectivity according to Fresnel's formula. Surface realization is not necessary; rather, microfacet orientation is generated, based on the SDF, for each incoming ray. Because a surface profile does not exist in MSM, the optical path of a propagating ray and whether the ray re-strikes the surface cannot be directly determined. Hence, MSM relies on a shadowing function, which determines the probability that a reflected ray re-strikes another surface facet, to model multiple scattering.

Even though MSM is developed for semitransparent wafers, the BRDF and BTDF calculated with MSM do not obey the reciprocity principle, which states that the BRDF and BTDF remain the same when the incidence and reflection directions are interchanged; $f_r\left(\theta_i,\phi_i,\theta_r,\phi_r\right)=f_r\left(\theta_r,\phi_r,\theta_i,\phi_i\right)$ [1]. Furthermore, the BRDF calculated with MSM does not agree with analytical BRDF models even if first-order scattering is dominant. Therefore, a weight function, which takes into account the projected area of a microfacet, is introduced to the SDF for observation of the reciprocity principle and agreement with analytical models [70].

In MSM, the SDF is unique statistical information about surface roughness statistics when the normal vector of a microfacet is generated for every incoming ray without surface realizations. Each microfacet is assumed to have the same projected area to the *x*-*y* plane A_0. However, all microfacets do not have the same hitting opportunity

for an incoming ray with a unit directional vector $\mathbf{s}_i$ due to the difference in the area projected into the incoming ray direction A_i. Figure 4.2 shows two microfacets with the same area A. The microfacet in Figure 4.2a has a larger projected area A_i and hence a larger chance to intersect the incoming ray than that shown in Figure 4.2b. Therefore, for the same value in the SDF, the probability that determines the normal vector of microfacets should be proportional to the projected area. Furthermore, if $\mathbf{n}\cdot\mathbf{s}_i \geq 0$, the incoming ray has no chance to reach the microfacet. Consequently, the weighted SDF determines the probability to generate the normal vector of microfacets.

$$p_w(\zeta_x,\zeta_y) = \frac{\Gamma \exp[-(\zeta_x^2+\zeta_y^2)/2w^2]}{\iint \Gamma \exp[-(\zeta_x^2+\zeta_y^2)/2w^2]\mathrm{d}\zeta_x\mathrm{d}\zeta_y} \tag{4.1}$$

The weight function Γ is defined as $\Gamma = A_i/A_0 = -\mathbf{n}\cdot\mathbf{s}_i/\mathbf{n}\cdot\mathbf{z}$ when $\mathbf{n}\cdot\mathbf{s}_i < 0$ and $\Gamma = 0$ when $\mathbf{n}\cdot\mathbf{s}_i \geq 0$. The weighted SDF is not limited to the incident rays, but also applies whenever the reflected and refracted rays strike an interface.

The rejection method is used to determine the normal vector of microfacets that follow the weighted SDF in Equation 4.1 with random numbers since the indefinite

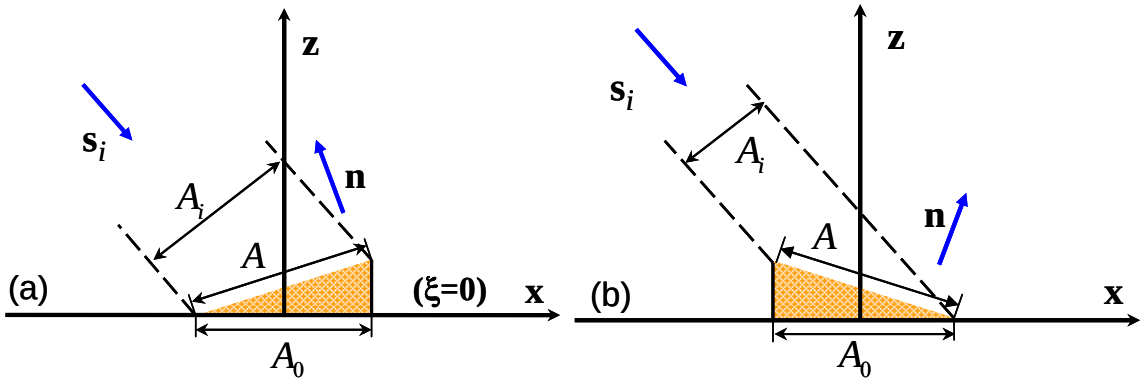

Figure 4.2 Effect of the projected area on the probability for an incoming ray to hit a microfacet when $\mathbf{n}\cdot\mathbf{s}_i < 0$. (a) $s_x \cdot n_x < 0$; (b) $s_x \cdot n_x > 0$.

integral and inverse function of the weighted SDF are difficult to obtain [39]. The rejection method requires a comparison function $g\left(\zeta_x,\zeta_y\right)$ that must have greater values in the whole domain than the weighted SDF and be applicable to the transformation method. A comparison function is chosen as a product of the Gaussian SDF $p_s\left(\zeta_x,\zeta_y\right)$ in Equation 2.12 with a multiplying constant, which depends on the incident direction, to ensure $g\left(\zeta_x,\zeta_y\right)\geq p_w\left(\zeta_x,\zeta_y\right)$. From the transformation method, the microfacet slopes that follow the Gaussian distribution are determined by two random numbers, R_1 and R_2:

$$\zeta_{x0}=w\sqrt{-2\ln R_1}\cos\left(2\pi R_2\right) \tag{4.2a}$$

$$\zeta_{y0}=w\sqrt{-2\ln R_1}\sin\left(2\pi R_2\right) \tag{4.2b}$$

Another random number R_3 is subsequently generated. The two variables ζ_{x0} and ζ_{y0} are accepted if the following inequality is satisfied:

$$R_3\leq p_w\left(\zeta_{x0},\zeta_{y0}\right)/g\left(\zeta_{x0},\zeta_{y0}\right) \tag{4.3}$$

Otherwise, they are rejected, and two new variables are created according to Equation 4.2 until this inequality holds. Although the original set of variables ζ_{x0} and ζ_{y0} follows the Gaussian distribution, the accepted set of variables satisfies the weighted SDF given in Equation 4.1. The normal vector of microfacets is calculated from the accepted slopes.

The in-plane BRDFs of a Gaussian surface computed with the weighted SDF are compared with the analytical model in Equation 2.41 for a perfectly conducting surface with $\sigma/\tau=0.1$ (or $w=0.14$) in Figure 4.3 to verify the introduction of a weight function. The in-plane BRDF refers to the BRDF in the plane of incidence ($\phi_r=\phi_i$ or $\phi_r=\phi_i+180°$), and the observation angle θ_{obs} is defined as θ_r when $\phi_r=\phi_i+180°$ and

$-\theta_r$ when $\phi_r = \phi_i$. Figure 4.3 shows excellent agreements between MSM and analytical model. However, if the Gaussian SDF is used without correction for the projected area, deviation is obvious at large incidence angles. Furthermore, BRDFs and BTDFs calculated with the weighted SDF obey the reciprocity principle within the numerical uncertainty. The agreement with the reciprocity principle and the analytical model demonstrates that the MSM using the weighted SDF correctly models surface roughness.

MSM corrected with the weighted SDF is further compared with both SGM and the rigorous approach with 1D Gaussian surfaces [71]. Figure 4.4 shows BRDFs of a surface with $\sigma/\tau = 1$ and $\sigma/\lambda = 2$, in which "EM" stands for numerical solution of electromagnetic waves. Contributions of first-order scattering and multiple scattering in the SGM and MSM simulation results were separated (not presented). Although first-order contributions from SGM and MSM are very close, MSM predicts a larger contribution from multiple scattering than SGM does. Since at normal incidence shadowing does not occur in first-order scattering, the comparison in Figure 4.4a

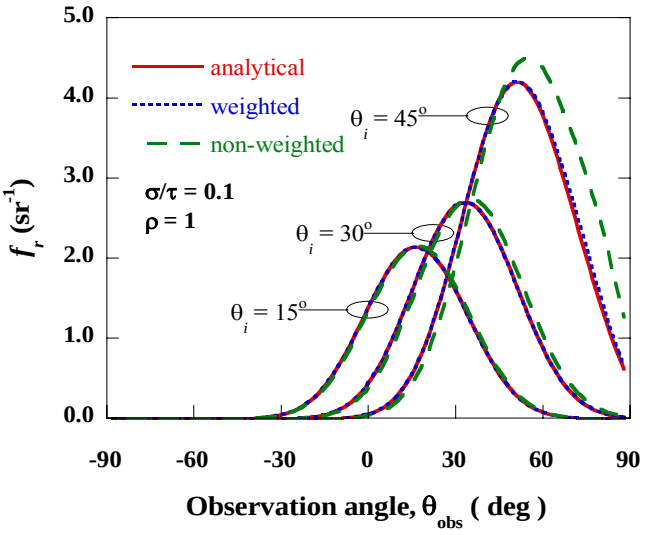

Figure 4.3 Comparison of MSM with the analytical model for a 1D perfectly conducting surface with $\sigma/\tau = 0.1$.

demonstrates that MSM has a limitation in modeling re-striking when σ/τ is large. The reason may be due to limitation of the shadowing function that does not consider the correlation between height and slope [72]. In addition, the generation of the second microfacet, which intercepts the reflected bundle from the first microfacet, is independent of the first microfacet. No correlation between microfacets may affect the prediction of multiple scattering. Usually, the contribution of multiple scattering predicted by MSM is higher than that by SGM.

In order to investigate the limitation of MSM with regard to the shadowing effect, the simulation is repeated at $\theta_i = 30°$. As shown in Figure 4.4b, the MSM result significantly deviates from the EM-wave solution. The BRDF curves predicted by MSM look similar in Figure 4.4a even though the incidence angle changes from 0° to 30°. On the other hand, SGM generally agrees with the rigorous approach even though it fails to predict the backscattering peak around $\theta_r = -\theta_i$. The shadowing effect may not be fully represented in MSM, and thus the error associated with re-striking may increase with the

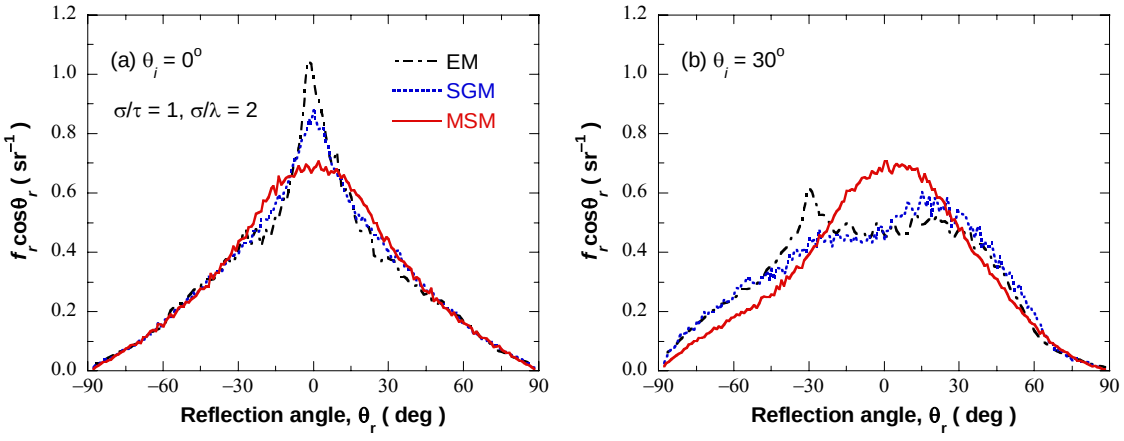

Figure 4.4 BRDFs calculated from the rigorous approach, SGM, and MSM for a 1D rough surface with $\sigma/\tau = 1$ and $\sigma/\lambda = 2$. (a) $\theta_i = 0°$; (b) $\theta_i = 30°$.

incidence angle. A shadowing function imposes limitations on MSM in terms of multiple scattering modeling because only surface realization allows accurate determination of shadowing and re-striking. Further comparisons show that MSM can result in reasonable agreement with the EM-wave solution when $\sigma/\tau < 1$ within the validity domain of SGM at normal incidence [47]. However, the validity domain of MSM becomes more limited at oblique incidence.

4.3 Consideration of Depolarization

The incident light may be decomposed into two linear polarizations: *s* polarization (TE wave) and *p* polarization (TM wave). The electric field or the magnetic field is perpendicular to the plane of incidence for *s* polarization or *p* polarization, respectively. Because of random microfacet orientation in a 2D rough surface, the incident polarization state changes upon reflection. As a result, the polarization of the scattered wave is different from that of the incident wave, i.e., depolarization occurs. However, most published works using the Monte Carlo method do not consider the polarization effect when they predict BRDFs or calculate the radiative heat transfer between rough surfaces. They are interested in radiative properties of isotropic surfaces for random polarization. They assumed that changes between the two polarizations counterbalances each other due to randomness of the scattering events and thus ignored depolarization. However, when radiative properties are studied for a specific polarization, depolarization must be considered even for isotropic surfaces. Furthermore, properties of anisotropic surfaces may necessitate the consideration of depolarization because the counterbalance between polarization states may not hold depending on the degree of anisotropy. Therefore, the

Monte Carlo method is extended to taking into account the change of the polarization state so that radiative properties of anisotropic surfaces are accurately modeled and studied for individual polarization [73]. Depolarization can be considered in ray-tracing algorithms when the microfacet reflectivity, ρ, is calculated.

In a 2D rough surface, even though the incident light is purely *s* or *p* polarized, both polarization components generally coexist in the local coordinates of a microfacet. The geometrical relations between wave vectors and polarization vectors delineate the contribution of each polarization to the microfacet reflectivity. Unit vectors in the direction of incidence and reflection, $\mathbf{s}_i$ and $\mathbf{s}_r$, may be expressed in terms of the zenith angles (θ_i and θ_r) and azimuthal angles (ϕ_i and ϕ_r) in the following manner; refer to Figure 2.1.

$$\mathbf{s}_i = \begin{pmatrix} -\sin\theta_i \cos\phi_i \\ -\sin\theta_i \sin\phi_i \\ -\cos\theta_i \end{pmatrix}, \qquad \mathbf{s}_r = \begin{pmatrix} \sin\theta_r \cos\phi_r \\ \sin\theta_r \sin\phi_r \\ \cos\theta_r \end{pmatrix} \tag{4.4}$$

In global coordinates, the vectors $\mathbf{s}_i$ and $\mathbf{z}$ define the plane of incidence, and the vectors $\mathbf{s}_r$ and $\mathbf{z}$ define the plane of reflection. A unit vector $\mathbf{h}_i$ perpendicular and a unit vector $\mathbf{v}_i$ parallel to the plane of incidence characterize the two polarizations of the incident wave. Here, $\mathbf{h}_i$ indicates the electric field for *s* polarization and $\mathbf{v}_i$ for *p* polarization. Similarly, unit vectors $\mathbf{h}_r$ and $\mathbf{v}_r$ represent the two polarizations of the reflected wave. Hence,

$$\mathbf{h}_i = \frac{\mathbf{z}\times\mathbf{s}_i}{|\mathbf{z}\times\mathbf{s}_i|} = \begin{pmatrix} \sin\phi_i \\ -\cos\phi_i \\ 0 \end{pmatrix}, \qquad \mathbf{h}_r = \frac{\mathbf{z}\times\mathbf{s}_r}{|\mathbf{z}\times\mathbf{s}_r|} = \begin{pmatrix} -\sin\phi_r \\ \cos\phi_r \\ 0 \end{pmatrix} \tag{4.5}$$

$$\mathbf{v}_i = \mathbf{h}_i \times \mathbf{s}_i = \begin{pmatrix} \cos\theta_i \cos\phi_i \\ \cos\theta_i \sin\phi_i \\ -\sin\theta_i \end{pmatrix}, \qquad \mathbf{v}_r = \mathbf{h}_r \times \mathbf{s}_r = \begin{pmatrix} \cos\theta_r \cos\phi_r \\ \cos\theta_r \sin\phi_r \\ -\sin\theta_r \end{pmatrix} \tag{4.6}$$

Microfacet reflectivity calculation involves two conversions of the polarization components. The *s*- and *p*-polarization components of incidence defined in the global coordinates are first converted to counterparts in the local coordinates. The local polarization components are respectively multiplied by Fresnel's reflection coefficients, and then converted to the global components. Accordingly, the microfacet reflectivities for co-polarization and cross-polarization can be expressed by [74,75]

$$\rho_{ss} = \left|\left(\mathbf{v}_r \cdot \mathbf{s}_i\right)\left(\mathbf{v}_i \cdot \mathbf{s}_r\right) R_s + \left(\mathbf{h}_r \cdot \mathbf{s}_i\right)\left(\mathbf{h}_i \cdot \mathbf{s}_r\right) R_p\right|^2 / \left|\mathbf{s}_i \times \mathbf{s}_r\right|^4 \tag{4.7a}$$

$$\rho_{sp} = \left|\left(\mathbf{h}_r \cdot \mathbf{s}_i\right)\left(\mathbf{v}_i \cdot \mathbf{s}_r\right) R_s - \left(\mathbf{v}_r \cdot \mathbf{s}_i\right)\left(\mathbf{h}_i \cdot \mathbf{s}_r\right) R_p\right|^2 / \left|\mathbf{s}_i \times \mathbf{s}_r\right|^4 \tag{4.7b}$$

$$\rho_{ps} = \left|\left(\mathbf{v}_r \cdot \mathbf{s}_i\right)\left(\mathbf{h}_i \cdot \mathbf{s}_r\right) R_s - \left(\mathbf{h}_r \cdot \mathbf{s}_i\right)\left(\mathbf{v}_i \cdot \mathbf{s}_r\right) R_p\right|^2 / \left|\mathbf{s}_i \times \mathbf{s}_r\right|^4 \tag{4.7c}$$

$$\rho_{pp} = \left|\left(\mathbf{h}_r \cdot \mathbf{s}_i\right)\left(\mathbf{h}_i \cdot \mathbf{s}_r\right) R_s + \left(\mathbf{v}_r \cdot \mathbf{s}_i\right)\left(\mathbf{v}_i \cdot \mathbf{s}_r\right) R_p\right|^2 / \left|\mathbf{s}_i \times \mathbf{s}_r\right|^4 \tag{4.7d}$$

In the microfacet reflectivities, subscripts *s* and *p* stand for each polarization while the first and second subscripts stand for the incidence and the reflection, respectively. In a special case where the planes of incidence and reflection are identical, the polarization state is maintained for either *s* or *p* polarization if only first-order scattering is involved. Therefore, the vectors $\mathbf{h}_i$ and $\mathbf{h}_r$ are parallel or antiparallel; consequently, $\mathbf{h}_i \cdot \mathbf{s}_r = 0$ and $\mathbf{h}_r \cdot \mathbf{s}_i = 0$. From Equation 4.7, ρ_{sp} and ρ_{ps} vanish, while $\rho_{ss} = \left|R_s\right|^2$ and $\rho_{pp} = \left|R_p\right|^2$. The corresponding BRDF becomes the in-plane BRDF. However, the cross-polarization term is generally nonzero even for in-plane BRDF when multiple scattering occurs.

In terms of the microfacet reflectivities, the reflected energies $G_{r,s}$ and $G_{r,p}$ are related to the incident energies $G_{i,s}$ and $G_{i,p}$ by

$$\begin{bmatrix} G_{r,s} \\ G_{r,p} \end{bmatrix} = \begin{bmatrix} \rho_{ss} & \rho_{ps} \\ \rho_{sp} & \rho_{pp} \end{bmatrix} \begin{bmatrix} G_{i,s} \\ G_{i,p} \end{bmatrix} \tag{4.8}$$

To facilitate calculation, the incident energy of each ray is set to unity such that $\left(G_{i,s}, G_{i,p}\right) = (1,0)$ for s polarization, $\left(G_{i,s}, G_{i,p}\right) = (0,1)$ for p polarization, and $\left(G_{i,s}, G_{i,p}\right) = (0.5, 0.5)$ for random polarization (i.e., unpolarized incidence). For the first reflection, $G_{r,s}$ and $G_{r,p}$ are calculated from Equation 4.8. For multiple reflections, the previously reflected energies are substituted for $G_{i,s}$ and $G_{i,p}$, and the next reflected energy is updated according to Equation 4.8. After a large number of ray bundles are traced for each polarization, the BRDF can be calculated in terms of the energies of the ray bundles [1]:

$$f_r\left(\lambda, \theta_i, \phi_i; \theta_r, \phi_r\right) = \frac{1}{G_i\left(\theta_i, \phi_i\right)} \frac{\Delta G_r\left(\theta_r, \phi_r\right)}{\cos\theta_r \Delta\omega_r} \tag{4.9}$$

where $G_i\left(\theta_i, \phi_i\right)$ is the total energy of the incident ray bundles and $\Delta G_r\left(\theta_r, \phi_r\right)$ is the energy of ray bundles leaving the surface within the solid angle $\Delta\omega_r$ in the direction $\left(\theta_r, \phi_r\right)$.

CHAPTER 5

ANISOTROPICALLY ROUGH SURFACE SIMULATION

SGM and MSM developed in Chapter 4 still need to assume that surface roughness follows known statistics such as Gaussian statistics. Anisotropic roughness effects on radiative properties cannot be investigated until rough surfaces are simulated based on the topography measurements described in Chapter 3. Therefore, SGM and MSM are further developed to model anisotropic roughness, separately, for their different ray-tracing algorithms. To validate the development of ray-tracing methods, predicted BRDFs of bare and gold-coated silicon surfaces are compared with TAAS measurements at a wavelength of 635 nm.

5.1 Incorporation of Topography Measurement

Zhu and Zhang incorporated anisotropic SDFs obtained from AFM measurements into an analytical BRDF model [27,28]. They demonstrated that anisotropic roughness effect is so significant that the BRDF of anisotropic silicon wafers changes drastically and it cannot be approximated as that of Gaussian surfaces. However, due to limitations of the analytical approach, only in-plane BRDFs with first-order scattering were studied in the works of Zhu and Zhang [27,28]. Therefore, ray-tracing algorithms with the Monte Carlo method are developed so that specific surface topography measurement can be employed without any assumption on roughness statistics. The ray-tracing algorithm to incorporate topography measurements is developed separately for both SGM and MSM when rough surfaces are simulated [73].

A common method for surface realizations in SGM is the spectral method, which is summarized in Section 2.2. A statistical function required for the spectral method is the power spectrum that is the Fourier transform of the autocovariance function $\sigma^2 C(\mathbf{r})$. Therefore, once an rms roughness and an autocorrelation length are specified, Gaussian surfaces can be generated using the Gaussian autocorrelation function in Equation 2.11. The spectral method is applicable for surface realizations regardless of whether the autocorrelation function is Gaussian or not [76]. However, the spectral method is not applicable for an anisotropic surface generation although the power spectrum and the autocorrelation function of the anisotropic surface can be obtained from surface topography measurements, as demonstrated in Section 3.1. In the present work, anisotropic roughness is modeled by directly tracing rays on the surface profile that the AFM measurement provides without surface realization. The surface topographic data were stored in a 2D array of surface height, which can be conveniently incorporated into the SGM algorithm. In fact, Knotts et al. used a similar approach for better agreement with experiment [77]. They fabricated 1D randomly rough surfaces to compare theory and experiment in light scattering. They measured the topography of fabricated surfaces with a stylus profilometer and found that the measured surface statistics are not consistent with Gaussian statistics in higher-order moments of the height distribution function. They found that the prediction based on the direct use of topography measurements yields much better agreement with experiment.

In the method of direct implementation, the number of rays to be traced is limited by the number of topography measurements. A large standard deviation of calculation can potentially occur even after the ensemble average. Therefore, several averaging steps

to reduce numerical fluctuations in SGM calculation are adopted. First, since the gold surfaces maintain the same surface statistics as the bare silicon substrates, all seven sets of topographic data including the gold surfaces are used. A post-processing step that smoothes BRDF curves by averaging the values of nine adjacent nodes is applied after the angular resolution of $\Delta\theta$ and $\Delta\phi$ is set to 1°. Particularly for in-plane BRDFs, values are further averaged based on the four-fold symmetry of the SDFs in Figure 3.2. The four-fold symmetry implies that the in-plane BRDF along the row ($\phi_i = 0°$) essentially equals to that along the column ($\phi_i = 90°$). The equality also holds for those along the two diagonals ($\phi_i = 45°$ and $135°$). Therefore, calculated in-plane BRDFs for $\phi_i = 0°$ and 90° are averaged and indicated as $\phi_i = 0°$ for the row and column directions. Similarly, calculation results for $\phi_i = 45°$ and 135° are averaged and indicated as $\phi_i = 45°$ for the two diagonal directions.

As discussed in Section 4.2, the rejection method is used for MSM to determine the orientation of microfacets following the weighted SDF with uniform random numbers. Because the rejection method is suitable for any type of distribution function as long as a comparison function is appropriately selected [39], the algorithm previously developed in Section 4.2 is also applicable for the SDF of anisotropic surfaces with a new comparison function. New comparison functions using a Gaussian functional form are selected to be always greater than the weighted SDF of anisotropic surfaces by adjusting both an rms value of the Gaussian function and a multiplying constant. The rejection method requires much more time for anisotropic surfaces than for Gaussian surfaces. The large difference between a weighted SDF and a comparison function increases the probability that a

microfacet generated with uniform random numbers is rejected until another microfacet is accepted. Meanwhile, for consistency with SGM, the averaged SDF of the seven measurements is used in MSM, and the same averaging steps are applied after calculation.

The shadowing function is not available for anisotropic surfaces, and multiple scattering modeling with a shadowing function for an anisotropic surface introduces further approximation. Nevertheless, the Smith shadowing function *S* [72] is adopted in MSM, and it is given by

$$S(\theta,\mu)=\frac{2\mu\sqrt{\pi}-\mu\sqrt{\pi}\,\mathrm{erfc}(\mu)}{\exp(-\mu^2)+2\mu\sqrt{\pi}-\mu\sqrt{\pi}\,\mathrm{erfc}(\mu)} \qquad 0^\circ \le \theta \le 90^\circ \tag{5.1}$$

where $\mu=\tau\cot\theta(90^\circ-)/2\sigma$ and erfc stands for the complementary error function. Because the Smith shadowing function is derived with Gaussian statistics, the term of $\sqrt{2}\sigma/\tau$ can be replaced with the rms slope *w*. For anisotropic surfaces, the value of $\sqrt{2}\sigma/\tau$, rather than that of *w*, is chosen for the shadowing function because σ and τ specifies the Gaussian autocovariance function required for surface realizations in the spectral method. Furthermore, roughness parameters should be represented as one value for the Smith shadowing function. From the seven topographic data sets, rms roughnesses of Si-1 (or Au-1) and Si-2 (or Au-2) are 0.51 and 0.64, respectively. Similarly, after further averaging over the four representative directions for *w* and τ, $w=0.28$ and $\tau=4.2$ are used for Si-1 (or Au-1) and $w=0.48$ and $\tau=3.1$ for Si-2 (or Au-2).

5.2 BRDF of Bare and Gold-Coated Silicon Surfaces

BRDFs of the silicon surfaces (Si-1 and Si-2) and the gold-coated surfaces (Au-1 and Au-2) are predicted with the Monte Carlo methods developed in the previous

Sections. The prediction is compared with the measurement using the TAAS at a wavelength of 635 nm. Silicon and gold refractive indices are $3.88+0.019i$ and $0.181+3.10i$, respectively, at this wavelength [78]. Therefore, approximately 500 μm thick silicon wafers are opaque to the laser light. For the gold film, 100 nm thickness is much greater than the photon penetration depth of 16 nm. Although local film thickness is reduced by the cosine of the microfacet inclination angle, it remains more than three times the penetration depth up to a 60° inclination angle. Furthermore, since the reflected radiation must travel through the gold film twice, the gold film can be safely regarded as semi-infinite in BRDF measurement and calculation.

With twenty million ray bundles, MSM calculations result in relative standard deviations less than 10% when the calculated values of $f_r \cos\theta_r$ are larger than 0.01. SGM calculations are performed on each of the seven topographic data, and a quarter million ray bundles are used for each surface. The relative standard deviation for SGM is less than 20% when $f_r \cos\theta_r > 0.05$, except around $\theta_r = 0°$ where the calculated BRDF considerably fluctuates due to the small solid angle ($\Delta\omega_r = \sin\theta_r \Delta\theta_r \Delta\phi_r$). It takes 20 minutes for SGM and 40 minutes for MSM to complete the calculation of each sample using a computer with a 3.2 GHz Pentium 4 processor and 2 GB memory. Note that it takes less time for MSM than for SGM to achieve the same standard deviation.

The azimuthal angles ϕ_i and ϕ_r are measured from the *x* axis in the counter-clockwise direction, as shown in Figure 2.1. When $\theta_i = 0°$, both the azimuthal angle of incidence ϕ_i and the plane of incidence become arbitrary. Nevertheless, if θ_i is treated as infinitesimal, ϕ_i can be defined even at $\theta_i = 0°$. Similarly, ϕ_r can be defined as well when

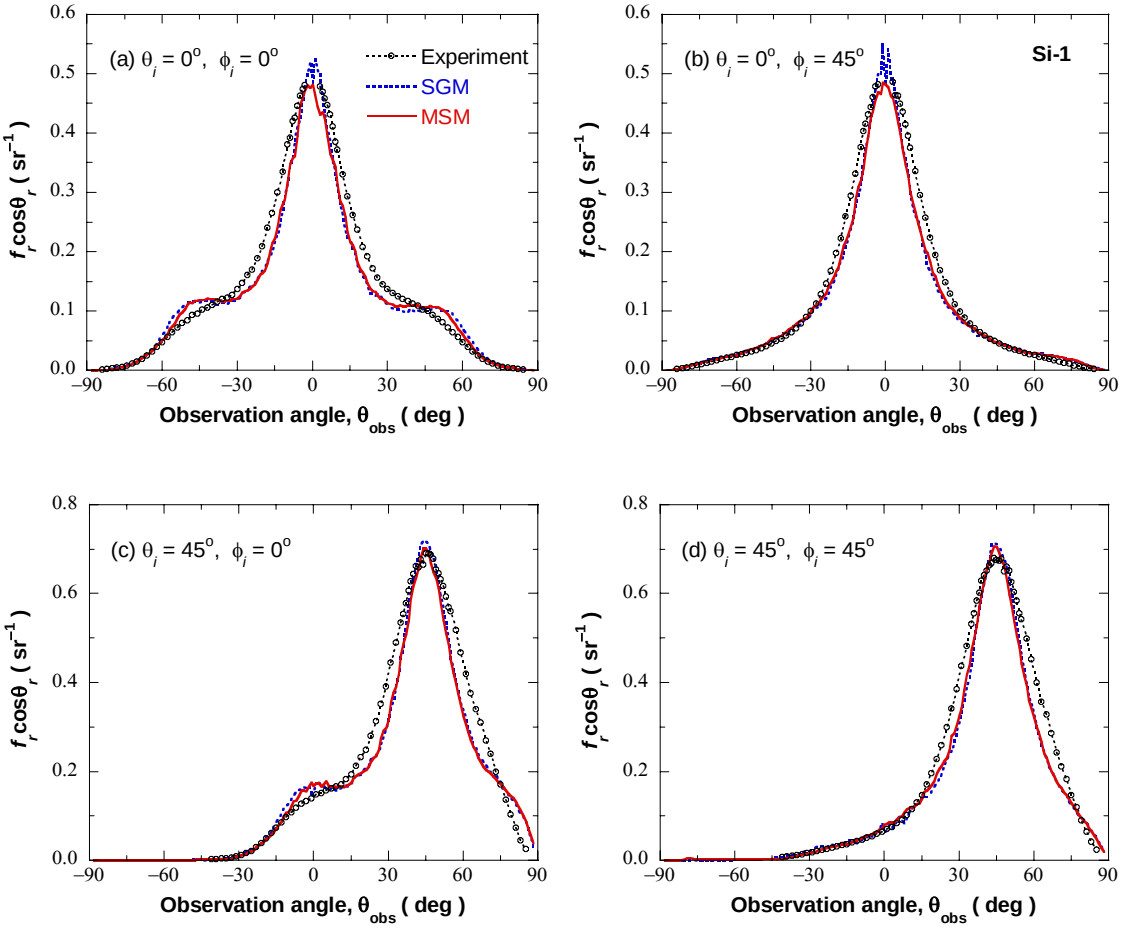

Figure 5.1 In-plane BRDFs of Si-1 for random polarization. (a) $\theta_i = 0°$ and $\phi_i = 0°$; (b) $\theta_i = 0°$ and $\phi_i = 45°$; (c) $\theta_i = 45°$ and $\phi_i = 0°$; (d) $\theta_i = 45°$ and $\phi_i = 45°$.

$\theta_r = 0°$. After the planes of incidence and reflection are identified, two linear polarizations of incidence and the in-plane BRDF ($\phi_r = \phi_i$ or $\phi_i + 180°$) are subsequently defined at $\theta_i = 0°$ and $\theta_r = 0°$.

The in-plane BRDFs of Si-1 for random polarization are compared in Figure 5.1 for different values of θ_i and ϕ_i. Hereafter, the BRDF is presented in terms of $f_r \cos\theta_r$, which is proportional to the reflected energy. Figure 5.1 shows that SGM and MSM essentially yield the same results, which agree reasonably well with measurements for all the cases. Measured and predicted BRDFs agree well at the specular peak $\theta_{obs} = -45°$ for $\theta_i = 45°$. Because the BRDF within ±2.5° in the retroreflection direction cannot be measured with the TAAS, no data are available for $-2.5° < \theta_{obs} < 2.5°$ in Figures 5.1a and 5.1b and for $-47.5° < \theta_{obs} < -42.5°$ in Figures 5.1c and 5.1d. It is well-known that scattering in the retroreflection direction can be greatly enhanced [29]. Thus, any interpolation or extrapolation of the BRDF in this region is not acceptable. Considerable fluctuations of SGM appear around $\theta_{obs} = 0°$ due to the small solid angle. The predicted BRDF curves for $\phi_i = 0°$ in Figures 5.1a and 5.1c have much more distinct shoulders than the measured, which may be caused by the artifacts in the AFM measurements. It should be noted that the reproducibility of the BRDF measurements is very good [54]. Around the specular and retroreflection directions or at large θ_r , wave effects may be sufficient to invalidate GOA. Therefore, the limitation of GOA may be responsible for the overprediction in Figure 5.1c when $\theta_{obs} > 75°$.

Figure 5.2 shows the same comparison for Si-2, which has larger σ and w and is more anisotropic than Si-1. In Figure 5.2a, prediction and measurement agree well,

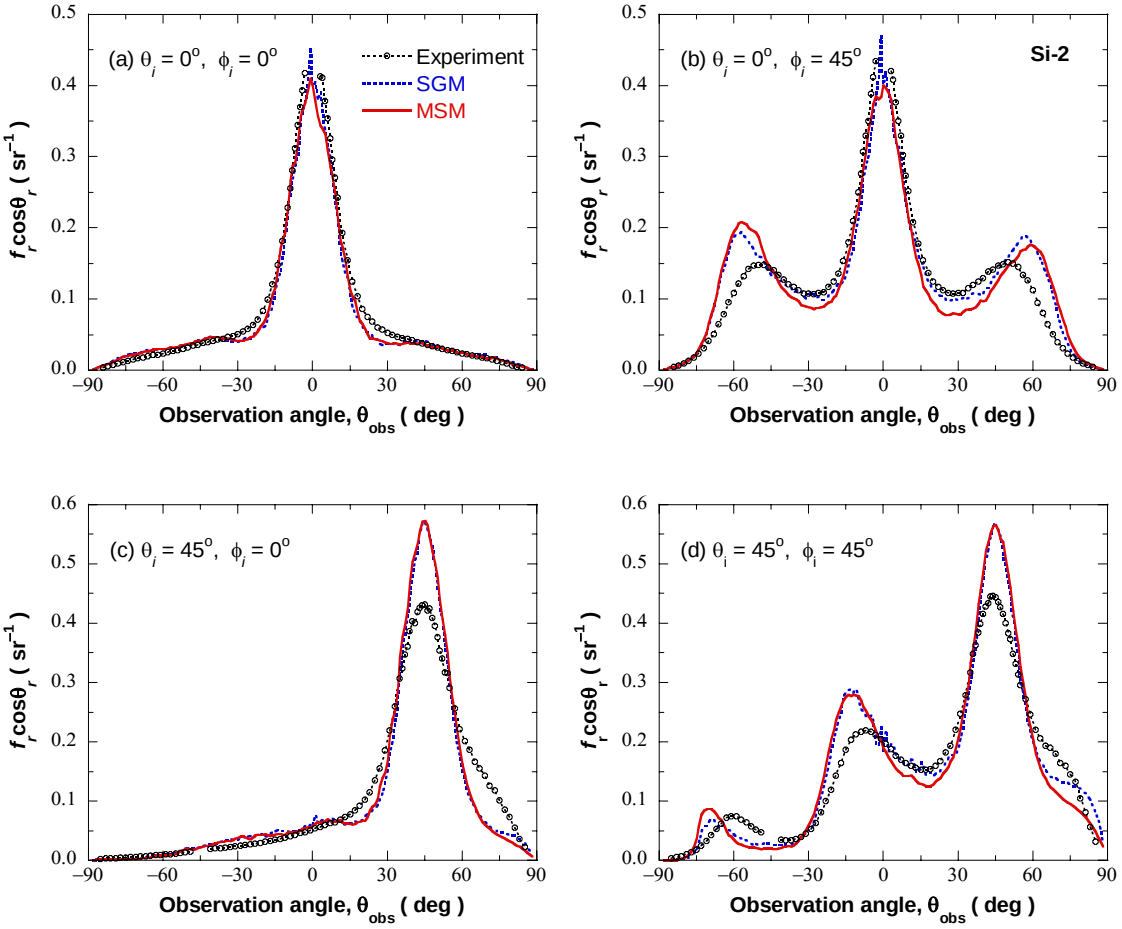

Figure 5.2 In-plane BRDFs of Si-2 for random polarization. (a) $\theta_i = 0°$ and $\phi_i = 0°$; (b) $\theta_i = 0°$ and $\phi_i = 45°$; (c) $\theta_i = 45°$ and $\phi_i = 0°$; (d) $\theta_i = 45°$ and $\phi_i = 45°$.

except near $\theta_{obs} = 0°$, where the measurements within ±2.5° could not be taken and the prediction has large fluctuations. While the Monte Carlo methods capture the general features and trends of the measured BRDF, relatively large discrepancies appear in other cases, especially when side peaks occur. When $\theta_i = 0°$ and $\phi_i = 45°$ in Figure 5.2b, the BRDF curves exhibit two large side peaks. These side peaks are associated with the side peaks in the SDF of Si-2 at $|\zeta_x| \approx |\zeta_y| \approx 0.36$; see Figure 3.2b. The Monte Carlo methods also predict the side peaks in the BRDF, but they fail to predict their position and magnitude accurately. The predicted side peaks are located on the average at $\theta_r = 57°$ whereas the measured are at 50°. The inclination angle of microfacets is half of θ_r at $\theta_i = 0°$ from the viewpoint of GOA. Therefore, the measured side peaks in the BRDF correspond to an inclination angle of 25°, which is very close to the angle of 25.2° between any of the four {311} planes and the (100) plane. On the other hand, the predicted side peaks correspond to an inclination angle of 28.5°. Although the angle calculated from the five AFM measurements for Si-2 is 27.1°, it is slightly increased to 27.9° after the additional average with the two AFM measurements for Au-2. The small difference of 0.6° indicates that the Monte Carlo methods are consistent with the AFM measurements. Consequently, side peak positions obtained from BRDF measurements is more reliable than those predicted by the Monte Carlo methods using the AFM measurements. Due to the artifacts in the AFM measurements, BRDF values may be overpredicted when $50° < |\theta_{obs}| < 80°$ and underpredicted when $15° < |\theta_{obs}| < 50°$ (noticeably for MSM) in Figure 5.2b.

When $\theta_i = 45°$ in Figures 5.2c and 5.2d, the two Monte Carlo methods noticeably overpredict BRDFs around the specular peak and underpredict at large observation angles. The overprediction is approximately 27%, presumably because the decrease in the optical roughness, defined as $\sigma \cos\theta_i / \lambda$, has invalidated the assumptions made in GOA. The underprediction at $60° < \theta_{obs} < 85°$ may result from the artifacts in the AFM measurements and the limitation of GOA. In Figure 5.2d, MSM yields smaller values at large θ_{obs} than SGM. Multiple scattering is usually significant at large reflection angles and causes the difference between SGM and MSM, which will be discussed later. When $\theta_i = 45°$ and $\phi_i = 45°$, a small side peak appears at $\theta_{obs} = -60°$ in the measured BRDF curve and at $\theta_{obs} = -70°$ in the predicted curves in Figure 5.2d. Since the small side peak corresponds to microfacets having {111} orientation with an inclination angle of 54.7°, a small side peak of BRDF should occur at $\theta_{obs} = -54.7 \times 2 + 45 = -64.4°$ if geometric optics is valid. Small side peak locations in the measured BRDF deviate from the predicted angles based on the crystalline orientation by 4.4°, which is significantly worse than the agreement for the large side peaks. Meanwhile, the additional average with the two AFM measurements for Au-2 has increased to the angle corresponding to the small side peaks from 57.0° to 57.3°. The value of 57.3° and the observation angle of -70° also indicate the consistency between the Monte Carlo methods and the AFM measurements.

Multiple scattering effects on the BRDF were investigated using SGM, which is more accurate since it does not employ the shadowing function. Only the results for Si-2 at $\theta_i = 45°$ and $\phi_i = 45°$ are shown in Figure 5.3 for each polarization to illustrate the contribution of multiple scattering. The component of multiple scattering for *s*

polarization is discernable, albeit small. Due to the small contribution of multiple scattering for *p* polarization, the component of multiple scattering in Figure 5.3b is magnified by a factor of 10. As the local incidence angle increases, $\rho_{ss} = |R_s|^2$ monotonically increases, whereas $\rho_{pp} = |R_p|^2$ decreases to zero at the Brewster angle, which is 75.5° for silicon at 635 nm wavelength, and increases rapidly beyond the Brewster angle. If the reflectivity is small, the energy of ray bundles experiencing multiple scattering will be further reduced. Thus, multiple scattering is insignificant for *p* polarization. The decrease of ρ_{pp} also explains why the specular peak for *p* polarization is greatly reduced and becomes comparable to the large side peak, as seen from Figure 5.3b. The contribution of multiple scattering to the reflectance is 6% for *s* polarization and 3% for *p* polarization, resulting in 4.5% for random polarization. The modeling also shows that the contribution of multiple scattering to the reflectance is less than 3% for Si-

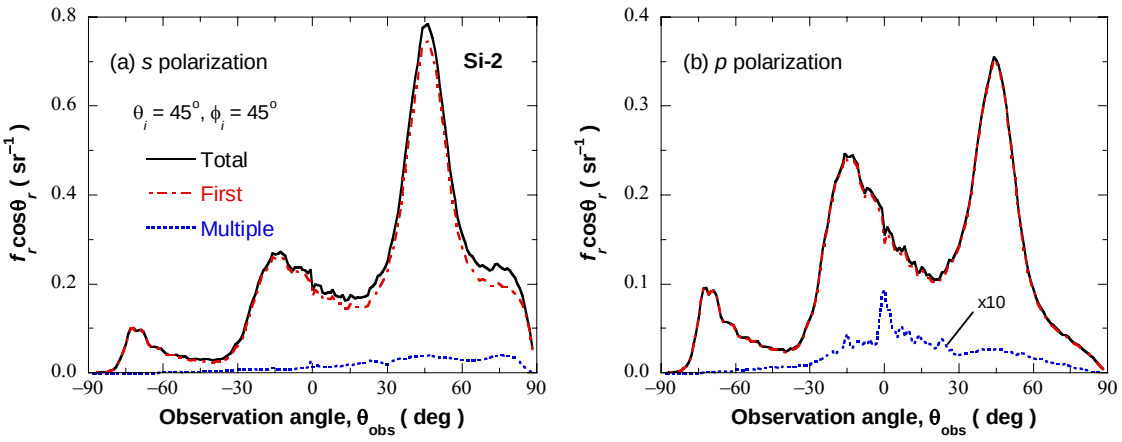

Figure 5.3 Predicted first-order scattering and multiple scattering for the in-plane BRDF of Si-2 at $\theta_i = 45°$ and $\phi_i = 45°$. (a) *s* polarization; (b) *p* polarization, where the contribution of multiple scattering is magnified by a factor of 10 to make it clear.

1 in the case of random polarization. The different contribution of multiple scattering for Si-1 and Si-2 is consistent with their different slope distributions. For the Au surfaces, on the other hand, multiple scattering contributes to the reflectance by less than 5% for Au-1 and by approximately 9% for Au-2, regardless of the polarization, because gold reflectivity is high and the difference between ρ_{ss} and ρ_{pp} is small.

The slight increase in multiple scattering at large θ_{obs}, as shown in Figure 5.3, partially accounts for the disagreement between MSM and SGM predictions as shown in Figure 5.2. The disagreement between MSM and SGM is largely caused by the methods' differences in handling multiple scattering. The introduction of a shadowing function allows MSM to include re-striking to some extent, but it is not possible to fully account for the shadowing effect [38,71]. At $\theta_i = 45°$ and $\phi_i = 45°$, MSM predicted that multiple scattering contributes to the reflectance of Si-2 by 11% for *s* polarization and 5% for *p* polarization. For Au-2, MSM predicted that the contribution of multiple scattering to the reflectance is 16% for either polarization. The shadowing function overpredicts multiple scattering, which is consistent with the discussion in Figure 4.4, resulting in smaller BRDFs at large θ_{obs}.

The in-plane BRDFs of Au-1 and Au-2 for random polarization are presented in Figure 5.4 at $\theta_i = 30°$ for two azimuthal incidence angles. The same surface topographic data were used for BRDF calculations of silicon and gold surfaces. Because they possess the same roughness statistics, comparison shows similar trends for silicon and gold surface BRDFs. However, the microfacet reflectivities of silicon and gold are 0.35 and 0.93 at normal incidence, respectively, and accordingly gold surface BRDFs are nearly three times large. Furthermore, the measured BRDF curves of Au-1 exhibit two split

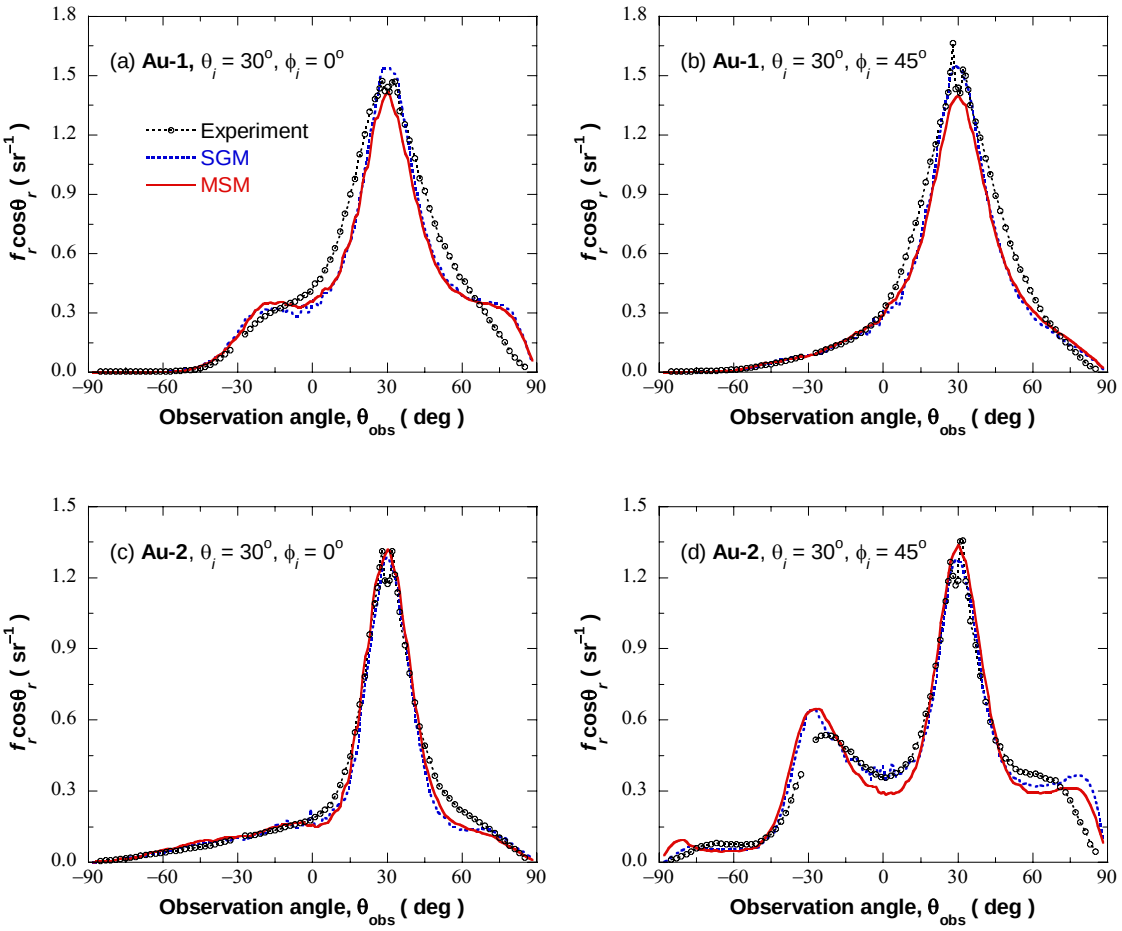

Figure 5.4 In-plane BRDFs of surfaces with gold coating at $\theta_i = 30°$ for random polarization. (a) Au-1 at $\phi_i = 0°$; (b) Au-1 at $\phi_i = 45°$; (c) Au-2 at $\phi_i = 0°$; (b) Au-2 at $\phi_i = 45°$.

peaks around the specular reflection $\theta_{obs} = 30°$, which is more distinct at $\phi_i = 45°$. Similar split peaks are observed for different values of θ_i. The Monte Carlo methods based on GOA do not predict the split peaks. In Figures 5.4c and 5.4d, measurements for Si-2 also display split peaks around the specular direction at both $\phi_i = 0°$ and $\phi_i = 45°$. Hence, wave interference may be important for highly reflecting surfaces. The difference between prediction and measurement around the specular direction in Figures 5.4c and 5.4d is smaller than that in Figures 5.2c and 5.2d because the optical roughness is larger at $\theta_i = 30°$ than at $\theta_i = 45°$. The reflection angle corresponding to the small side peak is very large (around $\theta_{obs} = -80°$), and thus reflected rays are likely to re-strike another microfacet and be redirected. As a result, the small side peak is barely observed in experiment and SGM prediction. However, MSM overpredicts the small side peak in this case because of the difficulty in correctly modeling multiple scattering.

Figure 5.5 shows the measured out-of-plane BRDFs of Si-2 at $\theta_i = 0°$ and $\phi_i = 45°$, along with those predicted by SGM. At this azimuthal angle of incidence, the in-plane BRDF is along $\phi_r = 45°$ and $\phi_r = 225°$. Because of the symmetry, the BRDF curves are only shown for ϕ_r from 0° and 45°. The BRDF depends little on ϕ_r when $\theta_r < 15°$, suggesting that the reflection is nearly isotropic at small θ_r. As θ_r increases, the dependence on ϕ_r increases and then decreases, becoming negligible at $\theta_r > 80°$. For $15° < \theta_r < 80°$, the BRDF increases with ϕ_r since the large side peak in the SDF is located along $\phi_r = 45°$. The BRDF for *s* polarization is greater than that for *p* polarization at $\phi_r = 45°$, and the difference decreases with reducing ϕ_r. The BRDFs for

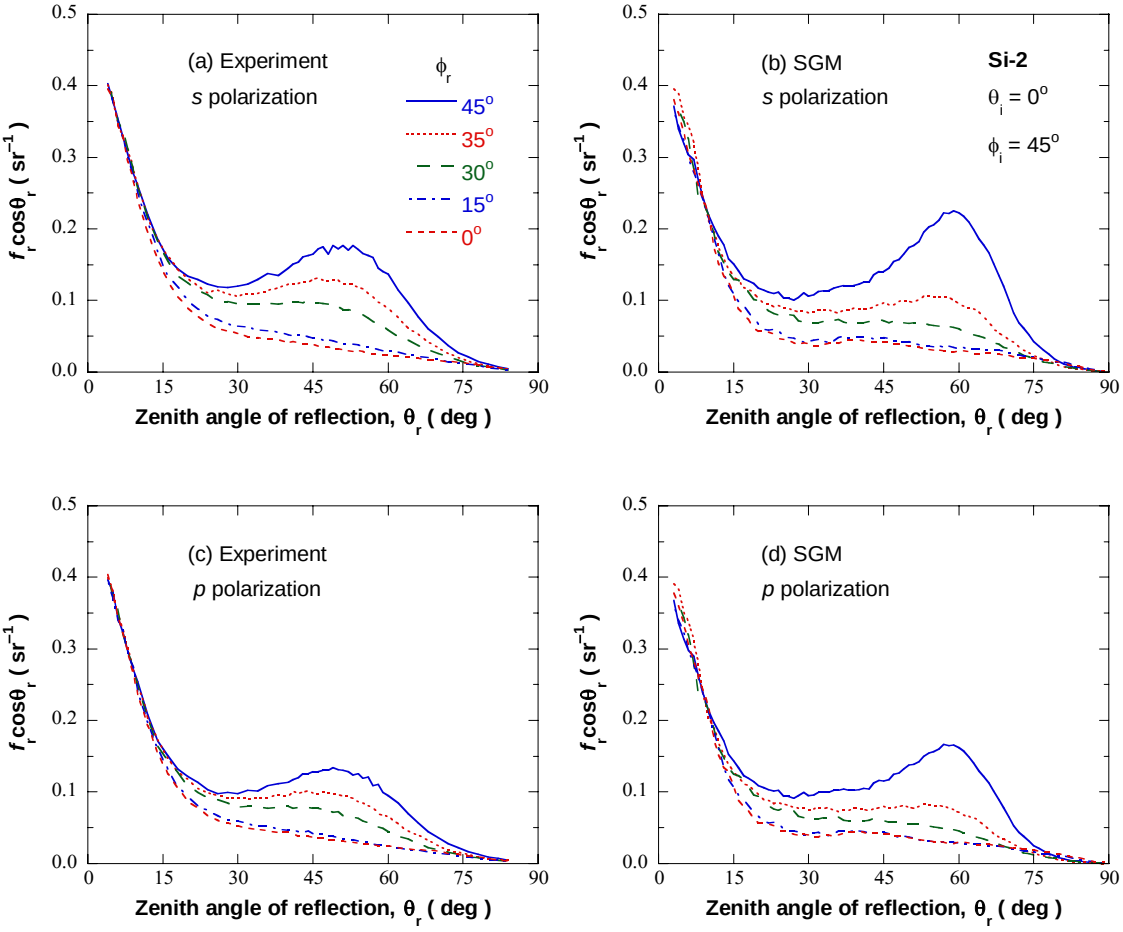

Figure 5.5 Out-of-plane BRDFs of Si-2 at $\theta_i = 0°$ and $\phi_i = 45°$. (a) Experiment for *s* polarization; (b) SGM calculation for *s* polarization; (c) Experiment for *p* polarization; (d) SGM calculation for *p* polarization.

the two polarizations are essentially the same at $\phi_r = 0°$. Microfacet reflectivity explains these trends. For in-plane reflection ($\phi_r = 45°$), $\rho_{ss} = |R_s|^2$ and $\rho_{pp} = |R_p|^2$ while $\rho_{ps} = \rho_{sp} = 0$. Then, $G_r = G_{r,s} + G_{r,p} = \rho_{ss}$ for *s* polarization, and $G_r = \rho_{pp}$ for *p* polarization from Equation 4.8. This result leads to a larger BRDF for *s* polarization than for *p* polarization at $\phi_r = 45°$. For out-of-plane reflection $(\phi_i \neq \phi_r)$, depolarization occurs and increases with $|\phi_i - \phi_r|$. For $\theta_i = 0°$ and $\phi_i = 45°$, $\mathbf{h}_r \cdot \mathbf{s}_i = 0$ and $\mathbf{h}_i \cdot \mathbf{s}_r = -\mathbf{v}_i \cdot \mathbf{s}_r$ at $\phi_r = 0°$. Substitution of these relations to Equation 4.7 gives $\rho_{pp} = \rho_{sp} = |R_p|^2$ and $\rho_{ss} = \rho_{ps} = |R_s|^2$. Consequently, $G_r = |R_p|^2 + |R_s|^2$ is the same for either incident polarization. In other words, although the incidence is purely *s* or *p* polarized, it is evenly decomposed into *s* and *p* components in the local coordinates of the microfacet; thus, the BRDFs at $\phi_r = 0°$ are the same for both polarizations. The predicted BRDFs also indicate the same trend as the measured. Because depolarization is considered, the Monte Carlo methods can account for BRDF dependence on the polarization. Besides good agreements, prediction shows notable disagreement around the side peaks for $\phi_r = 45°$, similar to the observations made earlier with Figure 5.2b.

The out-of-plane BRDFs of Au-1 and Au-2 predicted with MSM at $\theta_i = 30°$ are presented in Figure 5.6 as contour plots in a polar coordinate system. MSM was chosen because it reduces numerical fluctuations with small standard deviations. In these plots, the radial and azimuthal coordinates respectively correspond to θ_r and ϕ_r, and the *z* axis represents $f_r \cos\theta_r$. Because first-order scattering is dominant, all the BRDFs resemble the contour plot of SDFs in Figure 3.2. BRDF dependence on ϕ_r around the specular

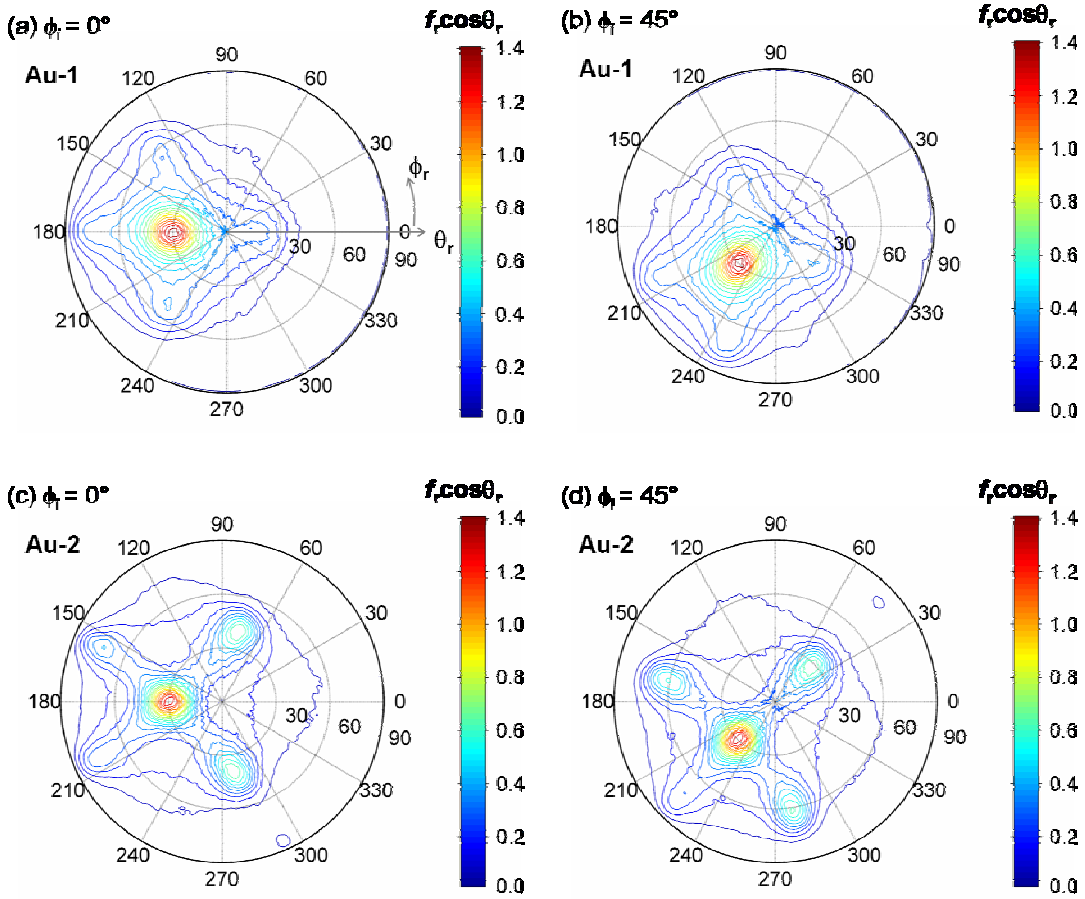

Figure 5.6 BRDFs predicted by MSM at $\theta_i = 30°$ for random polarization. (a) Au-1 at $\phi_i = 0°$; (b) Au-1 at $\phi_i = 45°$; (c) Au-2 at $\phi_i = 0°$; (d) Au-2 at $\phi_i = 45°$. In the polar contour plots, the radial coordinate corresponds to θ_r, and the azimuthal coordinate corresponds to ϕ_r.

direction is negligible, but dependence becomes large as angular separation from the specular peak increases. The region where the BRDF is independent of ϕ_r is broader for Au-1 than for Au-2 because Au-1 is not as anisotropic as Au-2. The predicted BRDFs for Au-2 display a strong specular reflection peak along with the four large side peaks associated with {311} planes. In addition, a small side peak associated with a {111} plane appears at large θ_r in Figure 5.6c at $\phi_r = 294°$ and another in Figure 5.6d at $\phi_r = 45°$. The actual magnitude of the small side peaks may be smaller than that predicted by MSM, and their positions may shift towards a smaller θ_r. Nevertheless, Figure 5.6 indicates that the Monte Carlo method is an effective technique to study the BRDF of surfaces with anisotropic roughness.

However, the developed ray-tracing methods do not predict BRDF when wave effects are significant due to the limitation of GOA. The in-plane BRDFs of Si-2 at $\theta_i = 60°$ and $\theta_i = 75°$ for random polarization are presented in Figure 5.7, where only

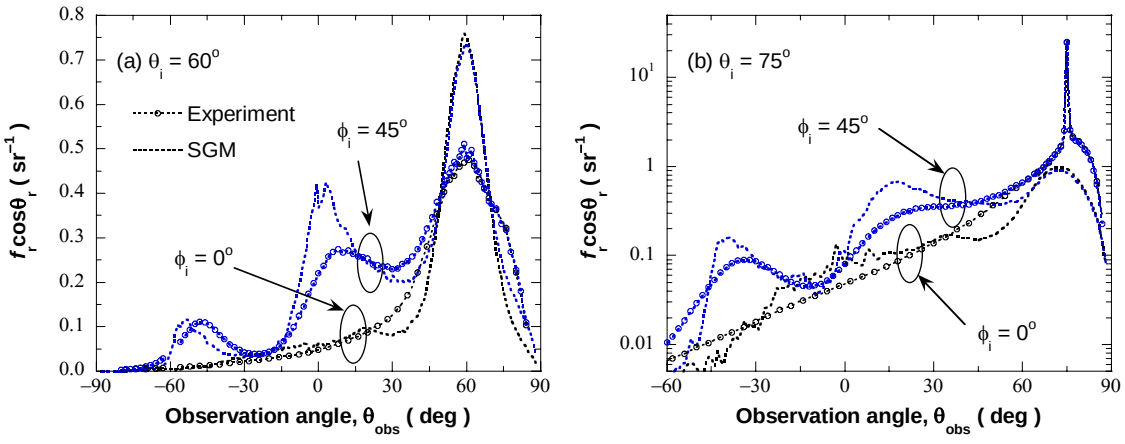

Figure 5.7 In-plane BRDFs of Si-2 for random polarization at large incidence angles. (a) $\theta_i = 60°$; (b) $\theta_i = 75°$. BRDFs are presented in log scale in Figure (b) because of large peaks in experiment.

BRDFs calculated with SGM are plotted. Optical roughness has decreased $\sigma\cos\theta_i/\lambda$, compared to Figure 5.2. Thus, wave features are involved in scattering and SGM does not predict BRDF well. As a result, difference between prediction and measurement in the specular direction is increased significantly. Experiment in Figure 5.7a also indicates split peaks in the specular direction, as shown in Figure 5.4, which justifies that wave effects are more significant at scattering from gold surfaces. At $\theta_i = 75°$ in Figure 5.7b, wave features are dominant such that a narrow specular peak. Note that BRDFs in Figure 5.7b are plotted in log scale because of the large peak. Wave interferences result in the narrow peak, and thus only the coherent component of BRDF can account for its occurrence. Prediction based on the ray-tracing method cannot address such large peaks. Wave effects on radiative properties will be more discussed with distinction of coherent and incoherent components in the following Chapter.

CHAPTER 6

APPLICABILITY OF PHASE RAY-TRACING METHOD

BRDF comparisons in Chapter 5 imply that the ray-tracing method based on geometric optics does not predict radiative properties well when wave features are involved. Some recent studies employed a modified ray-tracing method, which traces the field amplitude and phase rather than energy, to model the Mueller matrix. [79,80]. This method will be referred to as the phase ray-tracing method (PRTM) hereafter because phase is included. PRTM deals with wave interferences as far as smooth surfaces are concerned, but its applicability for modeling wave features in rough surfaces has not been established. Therefore, before PRTM is applied for further development of the ray-tracing methods, this chapter investigates whether PRTM accounts for wave features [81]. Mueller matrix elements calculated from PRTM, SGM, and KA are compared for 1D Gaussian surfaces with small and large roughness parameters. Beyond the evaluation of PRTM's applicability, the comparison will facilitate a fundamental understanding about how wave features affect radiative properties.

6.1 Phase Ray-Tracing Method

Most of the studies relevant to scattering, especially in heat transfer area, treat geometric optics and the ray-tracing method as synonyms [1-3,12,13,82]. Unless specifically mentioned, ray energy is traced. Therefore, the ray-tracing method cannot model the electric field, and it is valid in an incoherent limit (refer to Equations 2.7). Among various types of the ray-tracing method, only the application for scattering is of

interest, and thus SGM will be considered as a representative of the ray-tracing method in this chapter. Bruce introduced PRTM to model the Mueller matrix for rough surfaces with large characteristic lengths because PRTM models the electric field unlike SGM. However, he also regarded PRTM as geometric optics without distinction from SGM [79,80]. PRTM is able to handle some wave features beyond the validity domain of geometric optics. For example, the reflectivity of a smooth surface coated with a thin film can be calculated with the ray-tracing method when ray amplitude and phase difference between rays undergoing multiple reflections within the film is considered [1]. PRTM accounts for wave interferences and covers the regime of thin-film optics in a coherent limit although based on ray concept in geometric optics.

When PRTM is extended to scattering from rough surfaces, the direction of reflected rays is determined in the same fashion as SGM, i.e., specular reflection as discussed in Section 4.1. However, because ray amplitude is traced in PRTM, the amplitude is multiplied by complex Fresnel's reflection coefficient for every reflection, depending on the incident polarization. Phase difference between rays is also calculated

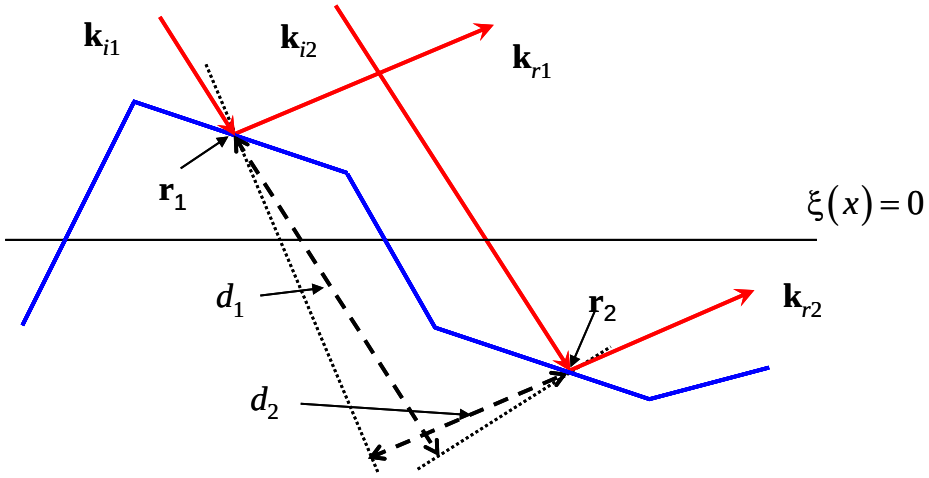

Figure 6.1 Optical path difference between two rays leaving the surface in the same direction.

based on relative difference in optical paths. Figure 6.1 shows the path difference of two rays leaving the surface in the same direction. Then, the phase difference becomes $\delta = \delta_1 - \delta_2 = (\mathbf{k}_i - \mathbf{k}_r) \cdot (\mathbf{r}_1 - \mathbf{r}_2)$, and any increase of traveling distances due to multiple scattering can be added. Because the relative path difference suffices, the path difference can be calculated using a reference point $[0,0]$. Multiplication of amplitude and $\exp(i\delta)$ results in a complex number, and a sum of complex numbers for rays leaving the surface can be interpreted as the reflected field. Since PRTM provides the reflected field, it allows the study of Mueller matrix as well as their coherent components.

Since depolarization does not occur from a 1D surface, reflected fields $E_{r,p}$ and $E_{r,s}$ are related with incident fields $E_{i,p}$ and $E_{i,s}$ via the following matrix formula.

$$\begin{bmatrix} E_{r,p} \\ E_{r,s} \end{bmatrix} = \begin{bmatrix} c_{pp} & 0 \\ 0 & c_{ss} \end{bmatrix} \begin{bmatrix} E_{i,p} \\ E_{i,s} \end{bmatrix} \tag{6.1}$$

The matrix elements c_{pp} and c_{ss} (field scattering coefficients) represent the far-field scattered amplitude for incident *p* and *s* states of unit amplitude, respectively, for a particular surface realization. All the quantities in Equation 6.1 are complex numbers and functions of incidence and reflection angles. The complex modulus of field scattering coefficients, $|c_{pp}|^2$ and $|c_{ss}|^2$, means cross sections of scattering for each polarization.

Since the reflected fields $E_{r,p}$ and $E_{r,s}$ are respectively proportional to the incident fields $E_{i,p}$ and $E_{i,s}$ by the field scattering coefficients c_{pp} and c_{ss} in Equation 6.1, the Mueller matrix elements in Equation 2.6 can be expressed in terms of the field scattering coefficients.

$$m_{11} = \frac{1}{2}\left\langle \left|c_{pp}\right|^2 + \left|c_{ss}\right|^2 \right\rangle \tag{6.2a}$$

$$m_{12} = \frac{1}{2}\left\langle \left|c_{pp}\right|^2 - \left|c_{ss}\right|^2 \right\rangle \tag{6.2b}$$

$$m_{33} = \frac{1}{2}\left\langle c_{pp}c_{ss}^* + c_{pp}^* c_{ss} \right\rangle \tag{6.2c}$$

$$m_{34} = \frac{i}{2}\left\langle c_{pp}^* c_{ss} - c_{pp}c_{ss}^* \right\rangle \tag{6.2d}$$

In calculation, therefore, the field scattering coefficients c_{pp} and c_{ss} can be independently calculated for *p* or *s* polarization of an incident field [79], and the Mueller matrix elements can be obtained according to Equations. 6.2. Then, all the elements are divided by the incident energy $\left|E_i\right|^2 l\cos\theta_i$.

When the incidence is linearly polarized at +45°, i.e., $\mathbf{S} = [1,0,1,0]$, the Stokes vector of the reflected field is $\mathbf{S}_r = [m_{11}, m_{12}, m_{33}, -m_{34}]$. Therefore, the four Muller matrix elements are respectively associated with the Stokes vector elements of the reflected wave when an incident wave with +45° linear polarization is scattered from a 1D rough surface. Similarly to the BRDF, the element m_{11} also describes the incident energy re-distribution after scattering and equals to $f_r \cos\theta_r$. SGM can consider ray energy for the two polarizations (G_p or G_s) separately according to Equation 4.8. Because of specular reflection from microfacets, energy is proportional to intensity and thus SGM calculates only the two Mueller matrix elements, m_{11} and m_{22}.

PRTM violates energy conservation when it is applied for rough surfaces [79,80]. Even for perfectly conducting surfaces, the reflectance obtained from PRTM is not unity.

The reflectance calculated with PRTM depends on surface length or the number of nodes. PRTM cannot be used to calculate any absolute radiative properties. The violation of energy conservation can be understood in terms of Huygens' principle. If a surface is smooth, wave vector difference, $\mathbf{k}_i - \mathbf{k}_r$, is parallel to the *z*-axis due to specular reflection. Position vector difference, $\mathbf{r}_1 - \mathbf{r}_2$, is parallel to the *x*-axis because $\xi(x) = 0$. Therefore, phase difference $\delta = (\mathbf{k}_i - \mathbf{k}_r) \cdot (\mathbf{r}_1 - \mathbf{r}_2)$ vanishes for the reflection from a smooth surface. PRTM inherently obeys Huygens' principle for ray tracing on smooth surfaces, and it is identical to SGM. However, PRTM does not obey Huygens' principle for rough surfaces. From a viewpoint of KA, an incident wave generates current sources for spherical wavelets at an intersected microfacet, and the incident wave amplitude and Fresnel's reflection coefficient determine current source strength. The spherical wavelets affect all points in the vacuum. KA considers all the spherical wavelets generated at the rough surface when the reflected field at a certain direction is calculated, following Huygens' principle. In PRTM, on the other hand, an incident wave generates sources with the same strength as KA. However, the sources give rays instead of spherical wavelets, and ray concept is constantly maintained after the reflection unlike KA, which cannot obey Huygens' principle. PRTM provides only relative radiative properties.

6.2 Mueller Matrix Comparison

For the evaluation of PRTM, the four Mueller matrix elements are compared for 1D silicon and gold surfaces which follow Gaussian statistics. Because 1D surfaces are studied, Green's function in Equation 2.24a with $H_0^{(1)}(x) \approx \sqrt{2/\pi x} e^{i(x-\pi/4)}$ is applied for

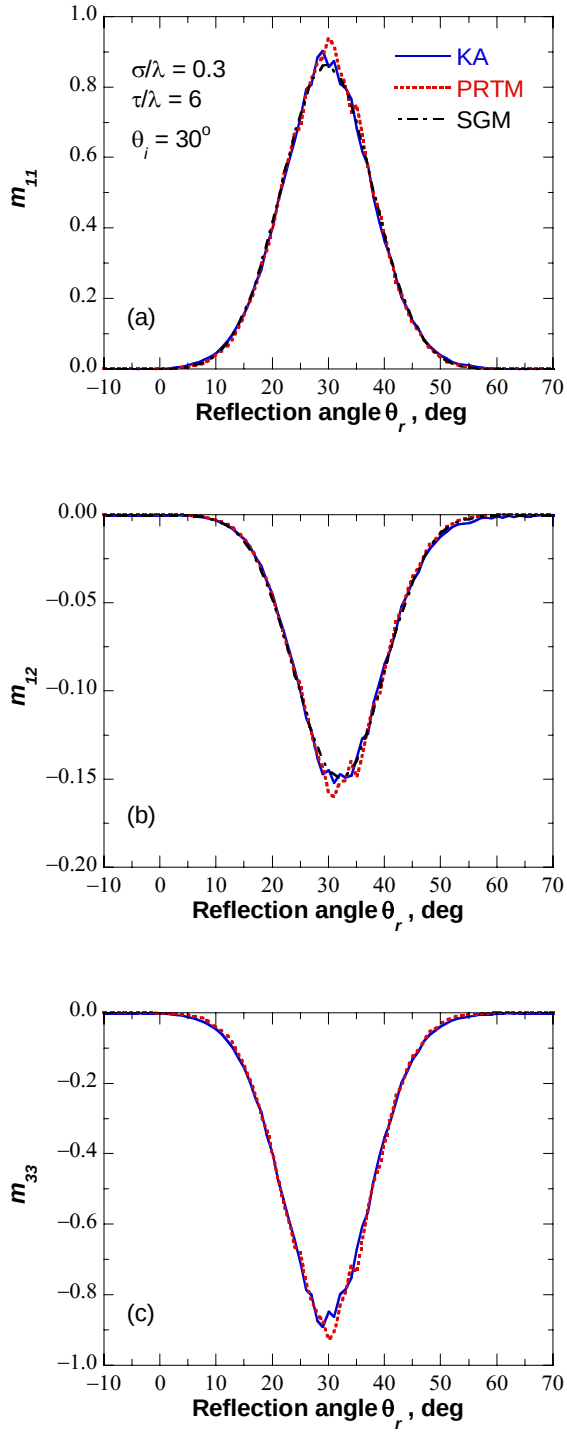

Figure 6.2 Mueller matrix elements for a silicon surface with $\sigma/\lambda = 0.3$ and $\tau/\lambda = 6$ when $\theta_i = 30°$; (a) m_{11}; (b) m_{12}; (c) m_{33}. The elements are calculated from the Kirchhoff approximation (KA), the phase ray-tracing method (PRTM), and the surface generation method (SGM).

KA and an integral equation corresponding to Equation 2.37 is numerically calculated with surface realizations. The incidence wavelength of 2 μm is used, and the complex refractive indices of silicon and gold are $n = 3.449$ and $n = 0.850 + 12.6i$, respectively. Silicon and gold surfaces respectively represent dielectric and highly conducting surfaces. All the elements are obtained from the ensemble average with 2000 surface realizations. Surface realization lengths range from 60λ to 180λ, and each surface is divided into 512 nodes. For comparison with KA and SGM, results obtained from PRTM must be normalized. Bruce normalized the matrix element m_{11} by fitting with measurements at an arbitrary reflection angle and the other elements by dividing with m_{11} [79]. However, in the present work, all the elements are normalized with the reflectance obtained from KA. Note that KA and SGM yield the same reflectance, even if both yield different BRDFs, as far as first-order scattering is involved [45].

Figure 6.2 shows Mueller matrix elements for a rough silicon surface with $\sigma/\lambda = 0.3$ and $\tau/\lambda = 6$ when $\theta_i = 30°$. The element m_{34} is related with the difference in reflected intensities between the right-handed and the left-handed circular polarizations, as defined in Equation 2.5. The circular polarizations can occur when a linearly polarized light is reflected from an absorbing material whose imaginary part of the refractive index is nonzero. Therefore, m_{34} calculations with a dielectric silicon surface result in only numerical fluctuations, so they are not presented in Figure 6.2. Because the small σ/τ^2 ratio indicates small radii of roughness curvature, KA is valid for the studied surface [14,40,46]. For all the elements in Figure 6.2, PRTM gives the same results as KA. The element m_{11} is the sum of reflected intensities from *p* and *s* polarizations and contains the

same information as the BRDF. On the other hand, the element m_{12} represents the difference in reflected intensities between the two polarizations. The intensity of *s* polarization is larger than that of *p* polarization, and thus the element m_{12} is negative. The small σ/τ ratio indicates small roughness slopes. Therefore, the difference between R_p and $-R_s$ is insignificant, and c_{pp} is nearly equal to $-c_{ss}$ as well. As a result, no appreciable difference between m_{11} and $-m_{33}$ is observed. SGM allows only the m_{11} and m_{12} calculations, and those two elements from SGM are compared together in Figures 6.2a and 6.2b. Comparisons demonstrate that SGM is also valid for the given surface. Even though the rms roughness is smaller than the wavelength, the autocorrelation length is large enough to validate SGM.

After incidence angle change from $\theta_i = 30°$ to $\theta_i = 0°$, a similar comparison with the same silicon surface as in Figure 6.2 is presented in Figure 6.3. Again, the difference between m_{11} and $-m_{33}$ is not distinguishable, and the element m_{33} is not presented. Figure 6.3a shows that agreement between KA and PRTM in the element m_{11} is still

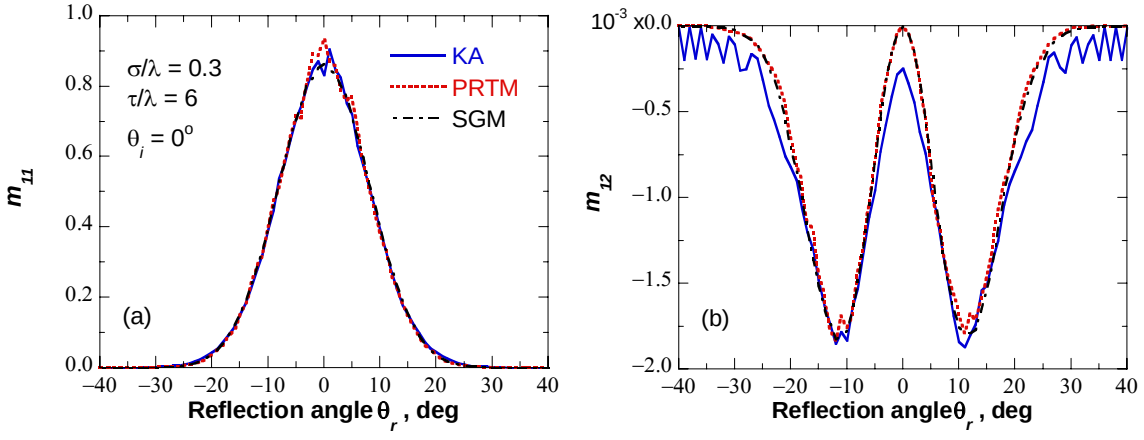

Figure 6.3 Mueller matrix elements for a silicon surface with $\sigma/\lambda = 0.3$ and $\tau/\lambda = 6$ when $\theta_i = 0°$. (a) m_{11}; (b) m_{12}.

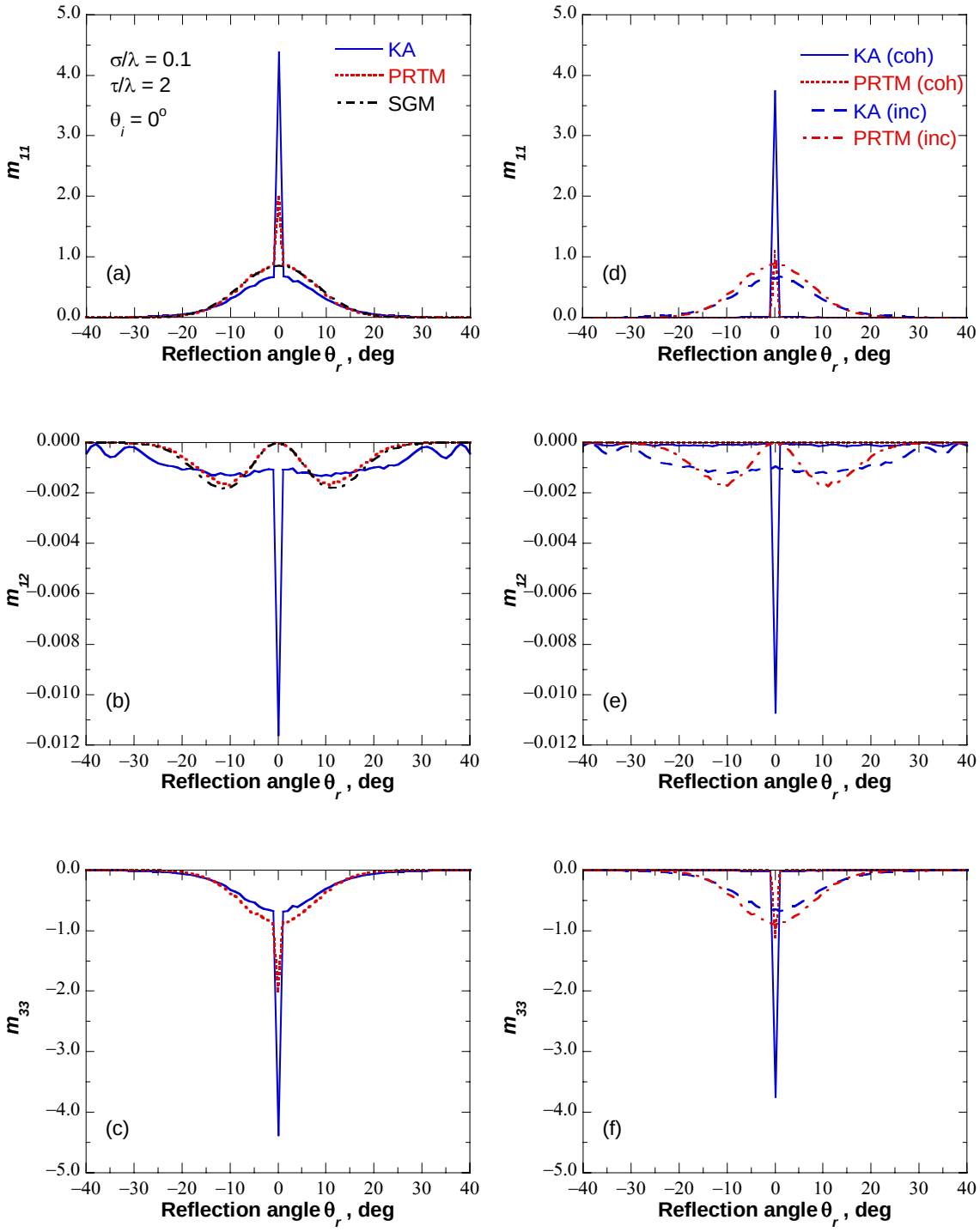

Figure 6.4 Mueller matrix elements for a silicon surface with $\sigma/\lambda = 0.1$ and $\tau/\lambda = 2$ when $\theta_i = 0°$ and their coherent and incoherent components. (a) m_{11}; (b) m_{12}; (c) m_{33}; (d) coherent and incoherent components of m_{11}; (e) coherent and incoherent components of m_{12}; (f) coherent and incoherent components of m_{34}.

good while bell-shaped distributions are maintained as in Figure 6.2a. However, the element m_{12} illustrates two symmetric valleys. The values of m_{12} in Figure 6.3b become smaller than those in Figure 6.2b according to the smaller intensity difference of reflected rays between *p* and *s* polarizations at $\theta_i = 0°$. Slight deviations of PRTM from KA are observed around $\theta_r = 0°$ and $|\theta_r| > 20°$ in Figure 6.3b. KA results oscillate at large reflection angles, and PRTM tends to match with SGM without any oscillation. Despite the small deviations, m_{12} is small and PRTM generally follows KA's trend. Therefore, for the surfaces with large characteristic lengths shown in Figures 6.2 and 6.3, it can be concluded that PRTM is essentially the same results as KA while it is identical to SGM. Coherent and incoherent components of the elements presented in Figures 6.2 and 6.3 are divided according to Equations 2.7. Due to the large rms roughness $\sigma/\lambda = 0.3$, the phase differences rays reflected in the same direction considerably vary. Therefore, coherent components are negligibly small in all the elements presented in Figures 6.2 and 6.3, and incoherent components are dominant. In fact, this observation is expected from the good agreement of SGM with KA.

Left three panels in Figure 6.4 show Mueller matrix elements for a silicon surface with $\sigma/\lambda = 0.1$ and $\tau/\lambda = 2$ when $\theta_i = 0°$. Both roughness parameters are scaled down by factor of 3, compared to those of the surface in Figures 6.2 and 6.3. The element m_{34} is not presented due to its insignificantly small values. KA reveals narrow peaks for all the elements in Figures 6.4a, 6.4b, and 6.4c, unlike the results in Figures 6.2 and 6.3. Note that the BRDF of Si-2 also shows the narrow specular peak in Figure 5.7a. PRTM also predicts narrow peaks in the elements m_{11} and m_{33} except the element m_{12}.

However, the peaks predicted by PRTM are smaller than those predicted by KA, approximately by 46% in Figures 6.4a and 6.4c. Furthermore, PRTM deviates from KA in other angular regions where PRTM matches SGM for the element m_{11}. Figure 6.4b indicates that PRTM completely differs from KA and better agrees with SGM, although m_{12} is small. Meanwhile, when the results in Figures 6.3 and 6.4 are compared, the elements m_{11} and m_{12} calculated by SGM do not change within numerical uncertainties despite the scale-down. Property invariance at a constant σ/τ ratio is a feature of SGM. On the other hand, peak appearance calculated by PRTM in some elements demonstrates difference between PRTM and SGM.

Coherent and incoherent components of the left panel results in Figures 6.4 are divided and presented in the right panel. Note that SGM does not model coherent components. Both KA and PRTM indicate that the narrow peaks of all the elements originate from coherent components, as a result of wave interferences. However, PRTM does not predict accurately incoherent components as well as coherent components in Figures 6.4d and 6.4f. In fact, it is well known that a narrow peak of coherent components in the element m_{11} usually occurs in the specular direction, and the distinction of coherent components has led to various applications. For instance, coherent and incoherent components are respectively approximated as specular and diffuse components of the reflectivity in many radiative heat transfer problems [1-3]. Only coherent components in the specular direction can be used to characterize roughness parameters, optical constants, or material thickness [4,83,84]. PRTM may not be applied for such applications because its inaccurate predicts coherent components of m_{11}. For the element m_{12}, moreover, PRTM does not show any noticeable contribution of coherent

components. With the same surface, coherent and incoherent components are additionally calculated at oblique incidence angles (not presented). In those cases, PRTM predicts coherent peaks smaller than those of KA for the element m_{12}, similarly to the comparisons in Figures 6.4d and 6.4f. Consequently, all comparisons suggest that PRTM predicts coherent components but it does not deal with wave features accurately for rough surfaces. For some elements, PRTM fails to predict coherent components.

So far the Mueller matrix is compared with silicon that is a dielectric material at 2 μm wavelength. Therefore, some comparisons made with gold are presented in Figures 6.5 and 6.6. Since the smooth gold surface reflectivity is 0.98 when $\theta_i < 30°$, gold surfaces may be regarded as perfectly conducting surfaces. With the same roughness parameters and incidence angle as in Figure 6.3, the elements m_{11} and m_{34} are compared in Figure 6.5. The element m_{33} is not presented because of negligible difference between m_{11} and $-m_{33}$. Furthermore, reflected energy difference between *p* and *s* polarizations is also small at normal incidence. Accordingly, m_{12} is very small and not presented. The results in Figure 6.5 have negligible coherent components due to the large rms roughness. The comparison of m_{11} in Figure 6.5a shows good agreement of the three methods. Compared to the results in Figure 6.3a, the element m_{11} of the gold surface is very similar to that of the silicon surface except that values are increased due to the large gold reflectivity. Interestingly, the element m_{34} of the gold surface also exhibits a similar variation as the element m_{12} of silicon surface in Figure 6.3b; a comparable magnitude, oscillation of KA results at large incidence angles, and some deviation at $\theta_r = 0°$. In

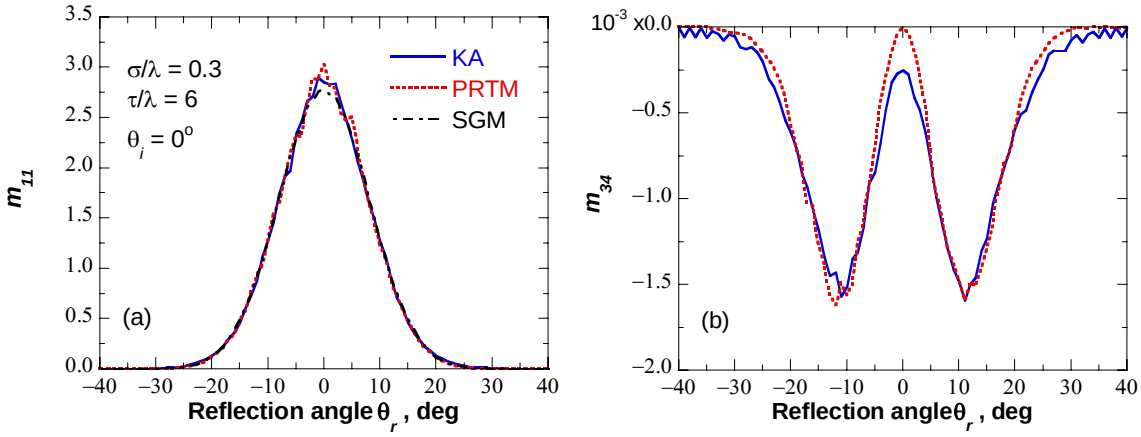

Figure 6.5 Comparison of the Mueller matrix elements for a gold surface with $\sigma/\lambda = 0.3$ and $\tau/\lambda = 6$ when $\theta_i = 0°$. (a) m_{11}; (b) m_{34}.

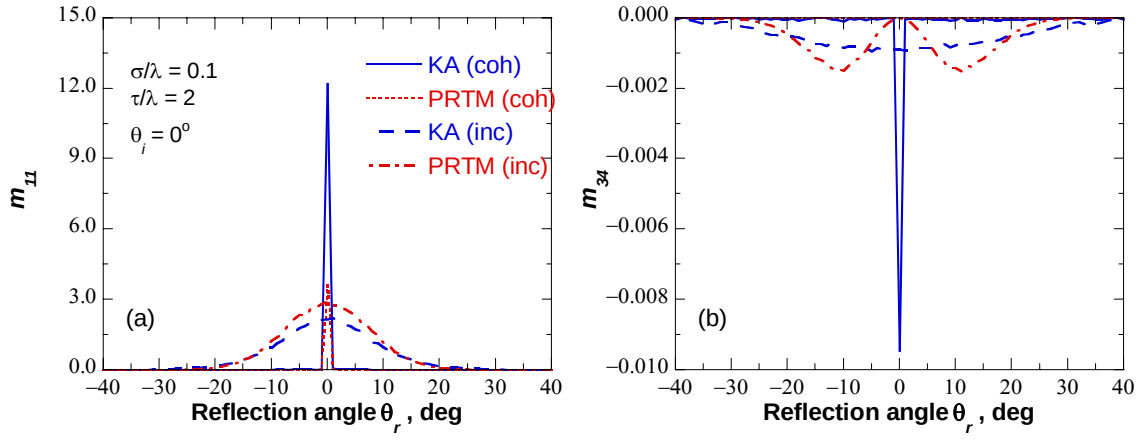

Figure 6.6 Comparison of coherent and incoherent components of the Mueller matrix elements for a gold surface with $\sigma/\lambda = 0.1$ and $\tau/\lambda = 2$ when $\theta_i = 0°$. (a) m_{11}; (b) m_{34}.

conclusion, the comparisons in Figures 6.3 and 6.5 suggest that PRTM is essentially the same as KA for all the four elements in an incoherent limit.

Figure 6.6 shows coherent and incoherent components of the elements m_{11} and m_{34} for a gold surface with $\sigma/\lambda = 0.1$ and $\tau/\lambda = 2$ when $\theta_i = 0°$. Due to the small rms roughness, coherent peaks appear for both elements, which is also true for the element m_{33}. Similarly to the comparisons in Figure 6.4, the narrow peak in the element m_{11} calculated with PRTM is smaller than that calculated with KA. PRTM fails to follow KA's trend in the element m_{34} while it does not predict noticeable coherent components. If the incidence angle is oblique, PRTM shows a coherent peak in the element m_{34} but it still underpredicts the peak. Regardless of surface materials, PRTM does not predict the elements of the Mueller matrix accurately when wave features are involved.

CHAPTER 7

BDRF OF ROUGH SURFACES WITH COATING

In this chapter, an analytical model-based approach, which is free from topography measurement errors, is proposed for the BRDF of rough surfaces with coating. The SDF is obtained from BRDF measurement of uncoated silicon surfaces using an inverse method rather than topography measurement. Then, the obtained SDF is employed into an analytical model, which is based on geometric optics for surface scattering and on thin-film optics for the microfacet reflectivity, for the BRDF of coated surfaces. Predicted and measured BRDFs of silicon surfaces with thin silicon dioxide coating are compared at the wavelength of 635 nm and coating thickness effect on the BRDF is investigated.

7.1 Analytical Model-Based Approach

In Chapter 5, BRDF comparisons suggest that the artifacts of AFM measurements could cause discrepancies between prediction and measurement. It is difficult, however, to distinguish whether modeling errors come from the topography measurements or from the limitation of GOA. If the same approach using topography measurements were applied to the BRDF of coated surfaces, modeled BRDFs would be subjected to three potential errors: topography measurement errors, the inherent limitation of GOA for rough surfaces without coating, and the additional limitation of GOA due to coating. A new modeling approach, which uses the SDF obtained from the BRDF of bare Si surfaces

by virtue of an inverse method rather than the SDF obtained from topography measurement, is proposed [62]. This approach is free from error due to surface characterization and saves time for a large number of surface topography measurements. Since first-order scattering is dominant for Si-1 and Si-2 at incidence angles up to 45° as discussed in Section 5.2, the use of an analytical BRDF model may suffice.

After introduction of the Smith shadowing function *S* to the analytical formula in Equation 2.41, the in-plane BRDF can be expressed as follows [27]:

$$f_r(\theta_i, \phi_i, \theta_r, \phi_r) = \frac{p_s(\zeta_x, \zeta_y) S\left(\theta_i, \sigma/\tau\right) S\left(\theta_r, \sigma/\tau\right)}{4\cos\theta_i \cos\theta_r \cos^4\alpha} \rho(n_s, \psi) \tag{7.1}$$

The slopes in the *x* and *y* directions, ζ_x and ζ_y can be expressed in terms of incidence and reflection angles.

$$\zeta_x = \frac{\partial\xi}{\partial x} = -\frac{\sin\theta_i \cos\phi_i + \sin\theta_r \cos\phi_r}{\cos\theta_i + \cos\theta_r} \tag{7.2a}$$

$$\zeta_y = \frac{\partial\xi}{\partial y} = -\frac{\sin\theta_i \sin\phi_i + \sin\theta_r \sin\phi_r}{\cos\theta_i + \cos\theta_r} \tag{7.2b}$$

The microfacet reflectivity $\rho(n, \psi)$ is the complex modulus of Fresnel's reflection coefficients, where n_s is the complex refractive index of a substrate and ψ is the local incidence angle. Because depolarization does not occur in the in-plane BRDF with first-order scattering, depolarization is not considered at microfacet reflectivity calculation. The microfacet inclination angle α and the local incidence angle ψ are $\alpha = (\theta_i + \theta_r)/2$ and $\psi = |\theta_i - \theta_r|/2$ when $\phi_r = \phi_i$, while $\alpha = |\theta_i - \theta_r|/2$ and $\psi = (\theta_i + \theta_r)/2$ when $\phi_r = \phi_i + 180°$.

In GOA, the extension to coated rough surfaces from opaque rough surfaces is straightforward [51,70]. The presence of coating changes only the microfacet reflectivity with the assumption that interference effects with a thin-film coating can be modeled by thin-film optics. If a film coating is sufficiently thin and possesses uniform thickness, the microfacet reflectivity can be calculated from Airy's formula considering multiple reflections and interferences inside a film as [2]

$$\rho\left(n_f, n_s, \beta\right) = \left| \frac{r_{0f} + r_{fs} e^{-i2\beta}}{1 + r_{0f} r_{fs} e^{-i2\beta}} \right|^2 \tag{7.3}$$

In the above expression, r_{0f} and r_{fs} are Fresnel's reflection coefficients at the air-film and film-substrate interfaces, respectively. The phase shift for a wave traveling through

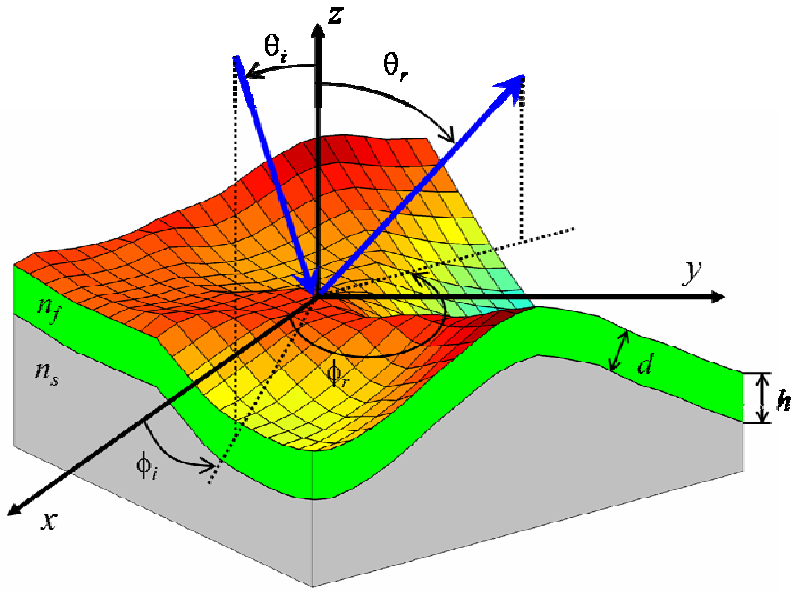

Figure 7.1 Schematic of a thin-film coated rough surface. The *x*-*y* plane is the mean surface of the air-SiO_2 interface. The refractive index of the coating is n_f and that of the substrate is n_s. The substrate is thick enough to be treated as semi-infinite. The average thickness of the coating is *h*, and $d = h\cos\alpha$ is the local film thickness. It is assumed that *h* is uniform, and thus the profile for the air-SiO_2 interface is identical to that of the SiO_2-Si interface.

the film is

$$\beta = \frac{2\pi n_f d \cos\theta_f}{\lambda} \tag{7.4}$$

where θ_f is the refraction angle in the film, defined in the local coordinates, and λ is the wavelength in vacuum. Since the microfacet is tilted by an inclination angle α, the local film thickness d is the projection of h to the microfacet normal, hence, $d = h\cos\alpha$; refer to Figure 7.1. In addition to the assumption of uniform film thickness, the application of Equation 7.3 also implies that microfacets are sufficiently large compared with film thickness and the autocorrelation length is much larger than the rms roughness. Otherwise, the reflected waves by different microfacets may interfere with each other. Zhu et al. [71] regarded this phenomenon as corner effect, which will be significant for the very precipitous surface roughness, relatively thick coatings, and at large incidence or reflection angles.

The inverse method refers to a method to obtain some roughness statistics from optical measurements. For instance, once the BRDF is known, the SDF can be inversely calculated from Equation 7.1 [28]. Therefore, the SDF can be obtained from a bare surface BRDF, and the obtained SDF can be used for modeling a coated surface BRDF. Since Si-1 and Si-2 have anisotropic SDFs, the cross section of the 2D SDF is required for modeling the in-plane BRDF. The in-plane BRDF of anisotropic surfaces at an azimuthal angles of incidence ϕ_i corresponds to the cross section of the 2D SDF in the coordinates rotated by ϕ_i. The rotational transform of coordinates ζ_x and ζ_y by ϕ_i can be performed using the following expressions:

$$\zeta_{x'} = \zeta_x \cos\phi_i + \zeta_y \sin\phi_i \tag{7.5a}$$

$$\zeta_{y'} = \zeta_y \cos\phi_i - \zeta_x \sin\phi_i \tag{7.5b}$$

After the SDF is transformed to new coordinates, $\zeta_{x'}$ and $\zeta_{y'}$, setting of $\zeta_{y'} = 0$ allows cross section calculation corresponding to the in-plane BRDF at ϕ_i.

$$p(\zeta_{x'}, \zeta_{y'} = 0) = \frac{4 f_r(\theta_i, \phi_i, \theta_r; \phi_r) \cos\theta_i \cos\theta_r \cos^4\alpha}{S(\theta_i, \sigma/\tau) S(\theta_r, \sigma/\tau) \rho(n_s, \psi)} \tag{7.6}$$

Since the σ/τ ratio should be known prior to determining $S(\theta_i, \sigma/\tau)$ and $S(\theta_r, \sigma/\tau)$, iteration is required for evaluating Equation 7.6. When the BRDF measured at normal incidence is used, shadowing effect can be minimized. For isotropic surfaces, the cross section of SDF, $p(\zeta_{x'}, \zeta_{y'} = 0)$, from the measured in-plane BRDF for any azimuthal angle suffices to determine σ/τ in iterative calculations. However, for anisotropic surfaces, the 2D SDF should be obtained from the BRDF measured over the hemisphere of reflection. The out-of-plane measurement over the entire hemisphere is extremely time-consuming and not very practical. An alternative method to determine σ/τ is to regard it as a fitting parameter. After obtaining the cross section of SDFs from the in-plane BRDF at normal incidence with Equation 7.6, the in-plane BRDF at oblique incidence calculated with Equation 7.1 can be fit to measurements by changing the parameter σ/τ. In the present work, however, the σ/τ ratios obtained from the AFM measurement ($\sigma/\tau = 0.51/4.3 = 0.12$ for Si-1 and $\sigma/\tau = 0.63/3.1 = 0.20$ for Si-2) are imported from Table 3.2 after assuming that the difference in σ/τ between measured and iteratively calculated values is negligible. Because the BRDF around the retroreflection direction cannot be measured with the TAAS, the SDF from the BRDF measured at $\theta_i = 3°$ is used to patch the SDF within $0° \le \theta_r \le 2°$.

For comparison purposes, the cross sections of the SDF obtained from both AFM and BRDF measurements are presented in Figure 7.2. The AFM results for $\zeta_x = 0$ correspond to the BRDF results for $\phi_i = 0°$, and the AFM results for $\zeta_x = \zeta_y$ correspond to the BRDF results for $\phi_i = 45°$. The cross sections obtained from the two methods have the same trend. As discussed in Section 3.1, tip convolution causes the measured profile to be rougher than the actual profile. Therefore, the cross sections of SDFs obtained from AFM measurements are larger than those from BRDF measurements at large values of $\zeta_{x'}$, and vice versa at small values of $\zeta_{x'}$. Tip convolution effect is more prominent for Si-2. In the BRDF comparison for Si-2 in Figure 5.2b, the size of the large side peaks based on AFM measurements is noticeably larger than the measured value. In Figure 7.2, however, the side peak sizes between AFM measurements and BRDF measurements are comparable to each other while the peak from AFM measurements is still shifted towards large slopes. By using the cross sections of the SDF obtained inversely from BRDF measurements, AFM artifact effects can be eliminated in the proposed approach.

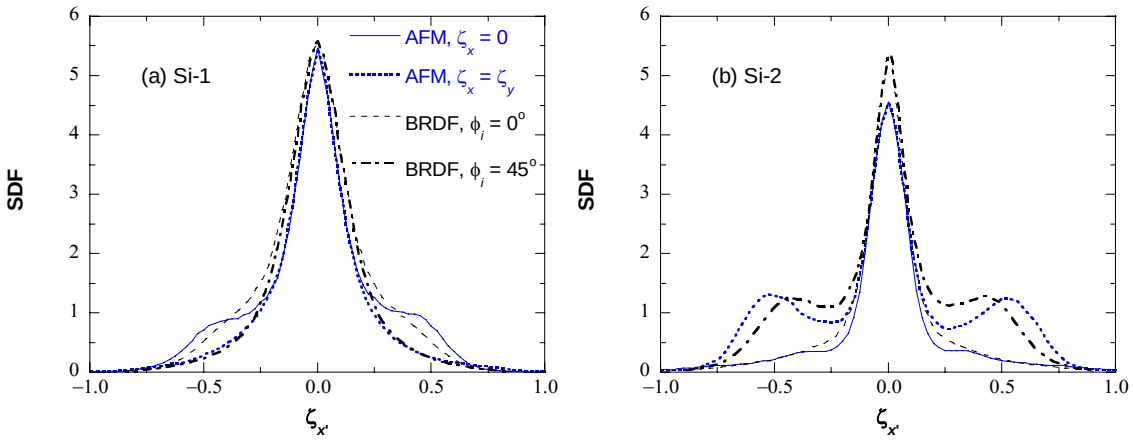

Figure 7.2 Cross sections of the SDF obtained from AFM and BRDF measurements for the bare silicon samples at two different azimuthal angles: (a) Si-1; (b) Si-2.

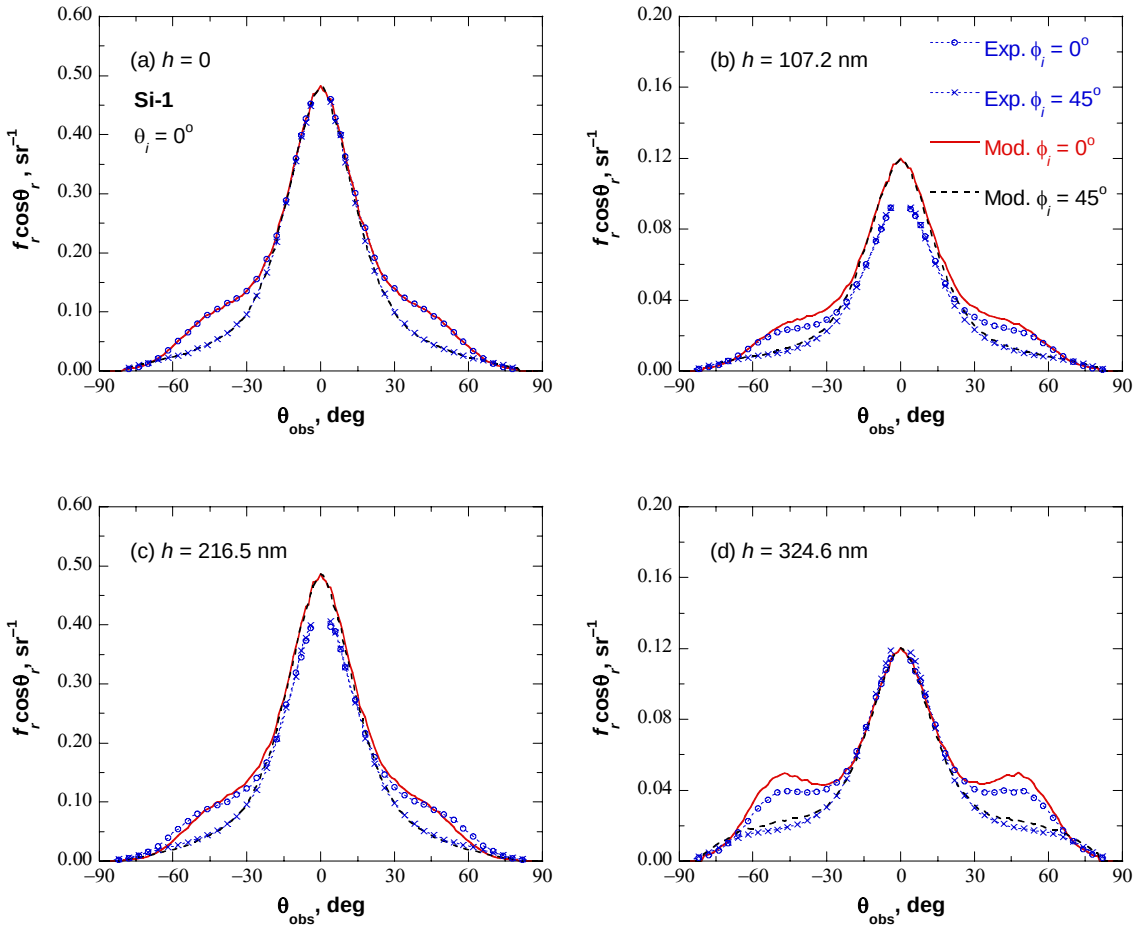

Figure 7.3 In-plane BRDFs of Si-1 for random polarization at $\theta_i = 0°$ with different coating thicknesses. (a) $h = 0$; (b) $h = 107.2$ nm; (c) $h = 216.5$ nm; (d) $h = 324.6$ nm.

7.2 BRDF of Silicon Surfaces with SiO_2 Coating

The BRDF of Si-1 at normal incidence is shown in Figure 7.3 for different coating thicknesses, where the results are averaged over *s* and *p* polarizations. The complex refractive indices of Si and SiO_2 are $(3.88,\ 0.019)$ and $(1.457,\ 0)$, respectively, at the laser wavelength $\lambda = 635$ nm [78]. In the legend, abbreviations of "Exp" and "Mod" stand for experimental and modeling results, respectively. Note that experimental and modeling results are exactly the same when $h = 0$ because SDF cross sections are obtained from the bare silicon surface BRDF. The predicted results agree well with measurements for all thicknesses. Coated surface BRDFs reveal similar anisotropic features to those observed without coating while the predicted BRDF in Figure 7.3d shows a much more distinct shoulder. Around the specular direction ($\theta_{obs} = \theta_i$), the BRDFs depend little on ϕ_i, and disagreement between measurement and prediction is large at $h = 107.2$ nm and $h = 216.5$ nm.

Figure 7.3 shows that BRDF magnitude changes significantly with film thickness. The measured BRDF values around the specular direction in Figures 7.3b and 7.3d are reduced by approximately four times, compared to those in Figure 7.3a, whereas the reduction in Figure 7.3c is insignificant. BRDF change can be explained by the phase shift variation with film thickness. If a surface is smooth, the phase shifts β at normal incidence are 88.5°, 178.8°, and 268.1° for film thicknesses of 107.2, 216.5, and 324.6 nm, respectively. While the local refraction angle is generally nonzero for a rough surface, the normal vector of microfacets is only slightly perturbed from that of a mean plane due to the small rms slope of Si-1. When β is close to 90° ($h = 107.2$ nm) and 270°

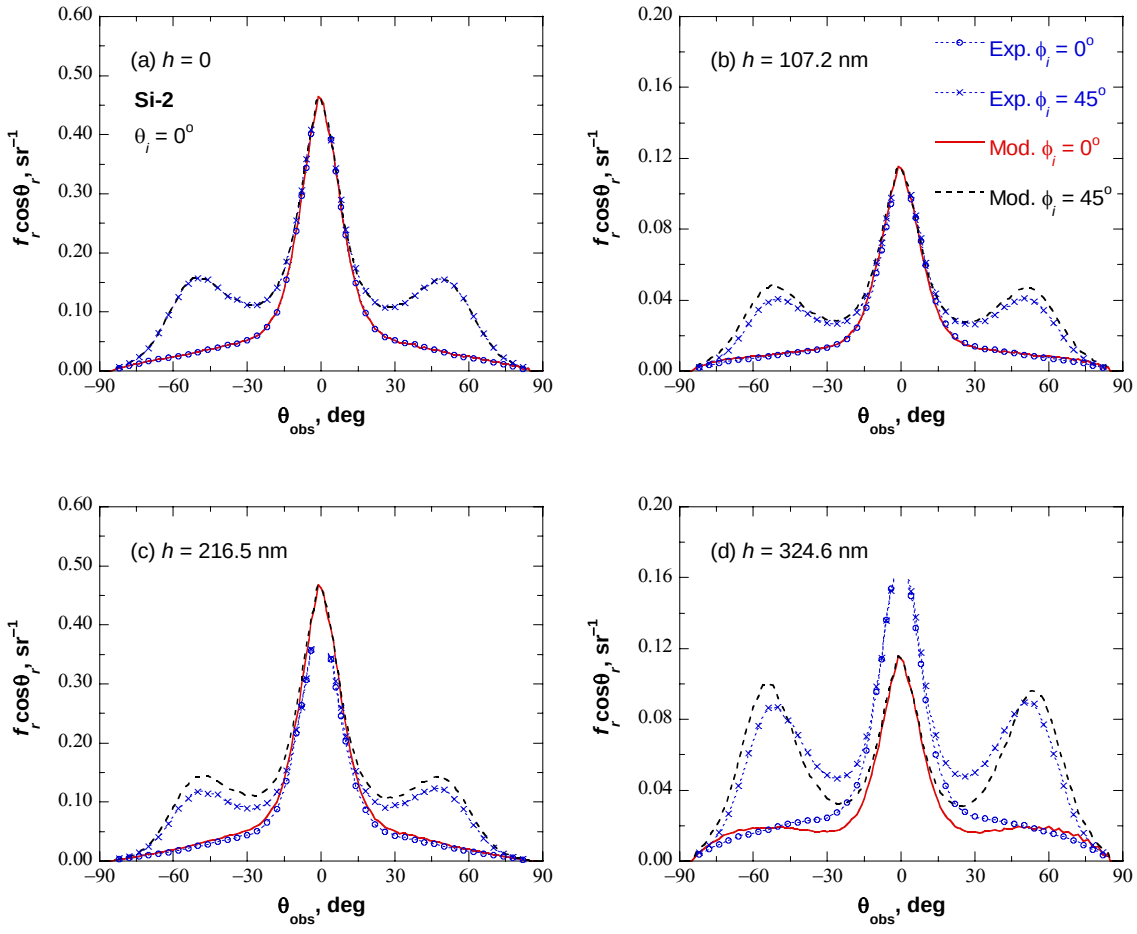

Figure 7.4 In-plane BRDFs of Si-2 for random polarization at $\theta_i = 0°$ with different coating thicknesses. (a) $h = 0$; (b) $h = 107.2$ nm; (c) $h = 216.5$ nm; (d) $h = 324.6$ nm.

($h = 324.6$ nm), destructive interferences within the coating result in microfacet reflectivity and BRDF reductions. On the contrary, when β is close to 180° ($h = 216.5$ nm), constructive interferences prevail and the BRDF values in Figure 7.3c are comparable to that of the bare Si surface. The GOA modeling is expected to be invalid as h becomes large, due to the corner effect. However, the agreement at $h = 324.6$ nm is not the worst. This counter-intuitive result may be related to the interference between scattered waves, which may be dependent on film thickness.

Figure 7.4 shows a similar comparison made with Si-2, whose SDF is strongly anisotropic and exhibits two side peaks along the diagonal directions in the SDF as can be seen from Figure 7.2. The side peaks in the SDF bring about counterparts in the BRDF at approximately $\theta_r = 50°$. While the central peak is much larger in the left panels, the side peaks are more prominent in the right panels. Figures 7.4b and 7.4c show that the GOA model agrees with the experiment at large reflection angles but significantly overpredicts BRDFs when $|\theta_{obs}| \le 15°$. The agreement is the worst for $h = 324.6$ nm, and the prediction is significantly lower than the measurement for $|\theta_{obs}| \le 45°$. Because the microfacets of Si-2 are more precipitous than those of Si-1, the corner effect for such a coating thickness may be significant and responsible for the large disagreement seen in Figure 7.4d. In addition to the corner effect, the profile of the air-film interface may differ from that of the film-substrate interface. The interface variation is likely to take place at a rougher surface and with a larger coating thickness, as shown in Table 3.3. When $h = 324.6$ nm, $\sigma = 0.69$ and $w = 0.52$ are respectively larger than those for bare Si-2

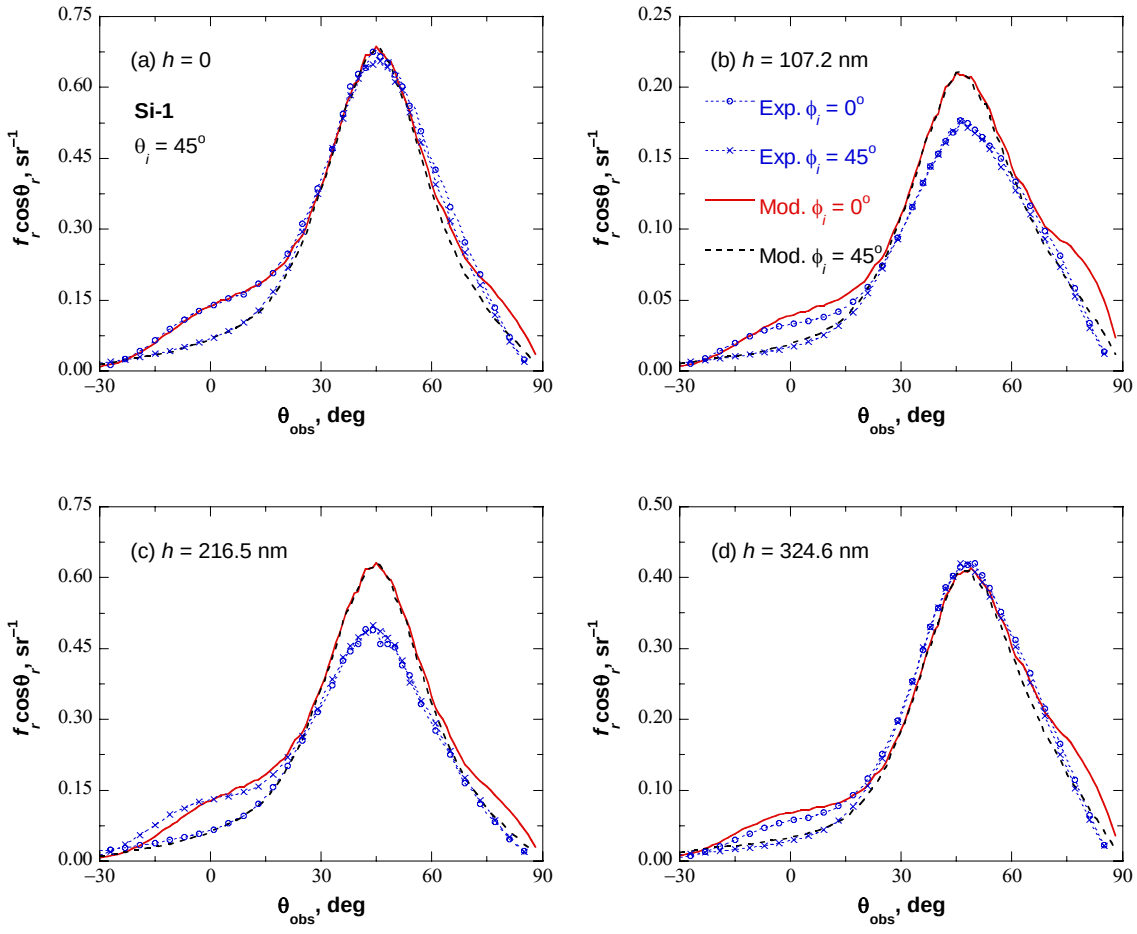

Figure 7.5 In-plane BRDFs of Si-1 for random polarization at $\theta_i = 45°$ with different coating thicknesses. (a) $h = 0$; (b) $h = 107.2$ nm; (c) $h = 216.5$ nm; (d) $h = 324.6$ nm.

($\sigma = 0.63 \pm 0.04$ and $w = 0.47 \pm 0.04$). Consequently, the large disparity observed in Figure 7.4d may be attributed to corner effect and non-uniform coating thickness.

The BRDF of Si-1 at $\theta_i = 45°$ is shown in Figure 7.5 to investigate the BRDF at oblique incidence. The predicted BRDFs at $\theta_{obs} > 50°$ in Figure 7.5a exhibit deviations from the measured values. The GOA modeling is often inaccurate at large reflection angles due to multiple scattering and interference between scattered waves. Because the former is negligible, the latter is likely to be responsible for the deviations. When the coating exists, the deviation along $\phi_i = 0°$ is more distinct. Note that for Si-1 without coatings, the predicted BRDF using the SDF obtained from AFM measurements showed similar deviations at large reflection angles, especially for *s* polarization [28]. Similarly to the results shown in Figure 7.3, the BRDFs in the left panels are larger than those in the right panels. BRDF reduction in Figure 7.5d is not as significant as that in Figure 7.3d. Because of the $\cos\theta_f$ term in Equation 7.4, the phase shift β at $\theta_i = 45°$ is 234.4°, which deviates from 270°. Disagreement around the specular direction is also obvious when $h = 107.2$ nm and $h = 216.5$ nm. Again, a larger film thickness does not always result in a larger disagreement.

Figure 7.6 shows the BRDF of Si-2 at $\theta_i = 45°$. Figure 7.6a illustrates a large disagreement around the specular direction and at large reflection angles even without coating. GOA becomes invalid as the optical roughness, $\sigma\cos\theta_i / \lambda$, decreases [47]. Thus, because the optical roughness at $\theta_i = 45°$ is smaller than that at $\theta_i = 0°$, the large disagreement occurs. Nevertheless, the prediction at $\theta_i = 45°$ for Si-2 is worse than that for Si-1, especially around the specular direction, because the σ/τ ratio of Si-2 is larger

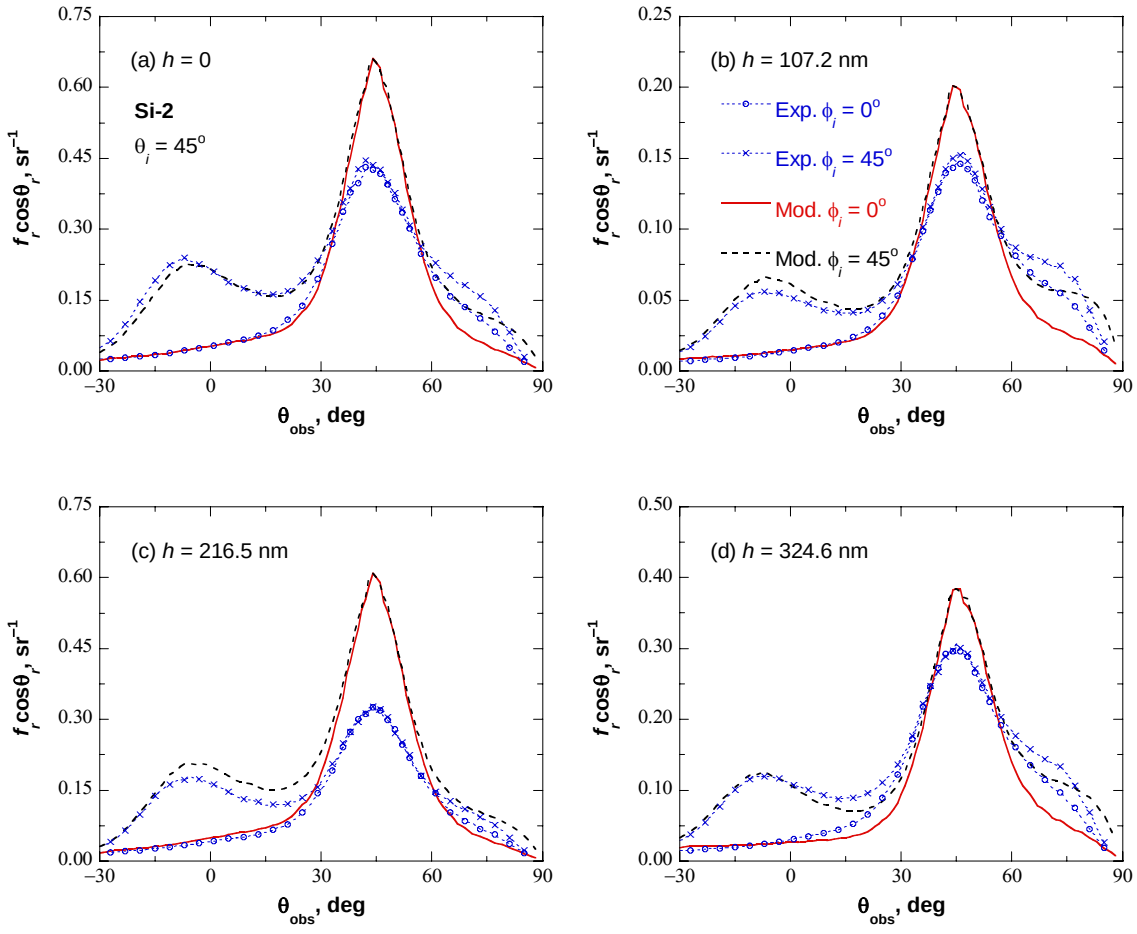

Figure 7.6 In-plane BRDFs of Si-2 for random polarization at $\theta_i = 45°$ with different coating thicknesses. (a) $h = 0$; (b) $h = 107.2$ nm; (c) $h = 216.5$ nm; (d) $h = 324.6$ nm.

($\sigma/\tau = 0.12$ for Si-1 and $\sigma/\tau = 0.20$ for Si-2). Tang et al. [47] suggested the validity domain of GOA as $\sigma\cos\theta_i/\lambda > 0.2$ at $\sigma/\tau = 0.20$ for a 1D perfectly conducting surface. Although Si-2 is within the validity domain of GOA ($\sigma\cos\theta_i/\lambda = 0.7$), it does not ensure good agreement since this regime may not be applicable for a dielectric surface with strong anisotropy such as Si-2. Considering the large disagreement for Si-2 without coating, the additional disagreement caused by coating does not seem as significant. Rather, the predicted and measured BRDFs in Figures 7.6b, 7.6c, and 7.6d agree better than those in Figure 7.6a in some regions. For example, the modeled BRDF in Figure 7.6c agrees better with experiment at $\theta_{obs} \le -10°$ and large θ_{obs}. The relative error at the specular peak is reduced from 53% at $h = 0$ to 35% at $h = 107.2$ nm or to 24% at $h = 324.6$ nm. The modeling results for $h = 324.6$ nm have already a large disagreement at $\theta_i = 0°$ as shown in Figure 7.4d. The disagreement at $\theta_i = 45°$ does not increase much, as can be seen from Figure 7.6d, although the corner effect is expected to be more significant at oblique incidence [71]. Better agreement for coated surfaces at $\theta_i = 45°$ may be attributed to complicated counteraction among the inherent limitation of GOA, the corner effect, and non-uniform coating thickness.

CHAPTER 8

ANISOTROPIC ROUGHNESS EFFECTS ON EMITTANCE

Comparisons in Chapters 5 and 7 demonstrate that anisotropic roughness affects the BRDF significantly and silicon surface roughness cannot be modeled with Gaussian statistics. However, it is not obvious whether anisotropic roughness has a large impact on the emittance because the emittance is obtained from the BRDF integration over the hemisphere. In this chapter, therefore, anisotropic roughness effects on the emittance are studied with SGM calculations based on two different surface simulations; one employs topography measurement of anisotropic surfaces as discussed in Chapter 5 and the other assumes the Gaussian surface with the same rms roughness and autocorrelation length. Predicted emittances are compared with sphere measurements described in Section 3.3 in a wavelength region from 400 to 1000 nm and an angular range from 0° to 60°.

8.1 Uncertainty Estimation of Emittance Measurements

The measurement equation of Equation 3.4 inevitably causes errors in actual measurements because of the assumptions made in integrating sphere theory. General error sources for integrating sphere measurements have been identified and well documented [65,66]. In particular, Edwards carefully examined various error sources for center-mount integrating spheres [65]. Preliminary measurements were made on a double-side-polished silicon wafer, which is lightly doped single crystalline and 200 μm thick, to estimate the emittance measurement uncertainty using the integrating sphere.

The spectral emittance was measured with the monochromator when the sample is tiled to approximately 7°. No polarizer was used because difference between the two polarizations is very small at near normal incidence. Figure 8.1a shows the emittance averaged over five measurements, along with that calculated with silicon optical constants in Ref. [61]. For a smooth sample, $\eta = 0$ and no correction in the measurement equation is necessary. The wafer is opaque except near the wavelength $\lambda = 1000$ nm, where the emittance drops suddenly because the wafer becomes semitransparent. Emittance decrease at short wavelengths is due to an increase of the silicon refractive index. Excellent agreement is observed between experiment and calculation with the largest deviation of 0.008 at 950 nm. Standard deviations for five measurements are less than 0.001. Based on both the 95% confidence level of five measurements and the deviation from the calculations, the expanded uncertainty for measurements at near normal incidence is estimated to be less than 0.010.

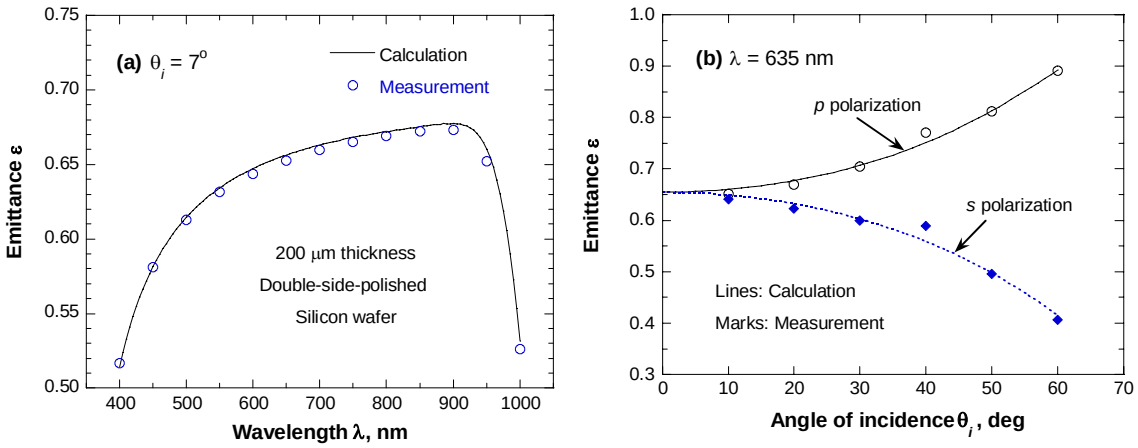

Figure 8.1 Comparison of emittance measurements with theoretical calculations for a double-side-polished wafer of 200 μm thickness. (a) Emittance spectrum at near normal incidence (approximately $\theta_i = 7°$) in the wavelength region from 400 to 1000 nm; (b) Variation of emittance with zenith angles of incidence θ_i at the wavelength of 635 nm for individual polarizations.

Figure 8.1b shows the double-side-polished wafer emittance at different incidence angles measured with the 635 nm diode laser for each polarization. The maximum standard deviation of five measurements increases to 0.005 due to manual sample rotation. Except at an incidence angle of 40°, measurement deviations from theoretical calculations are less than 0.008, which are comparable to those in Figure 8.1a. Exceptionally large errors occur at $\theta_i = 40°$, at which the absolute error becomes 0.020 for *p* polarization and 0.032 for *s* polarization. A supporting rod of the baffle lies between a sphere side wall and the detector; refer to Figure 3.7. Therefore, when the incidence angle is around 45°, the supporting rod screens a part of reflections from the side wall to the detector, resulting in large measurement errors. However, if a rough sample is measured, the errors due to the supporting rod may be reduced because the reflection from rough samples may have large angular spread. Therefore, the expanded uncertainty for directional measurements is estimated to be generally within 0.020.

8.2 Emittance of Bare and SiO_2-Coated Silicon Surfaces

The emittance spectrum of Si-1 for random polarization at near normal incidence is presented in Figure 8.2a. Emittance measurements are compared with results modeled with SGM based on two different surface simulations. The anisotropic modeling uses the AFM topography measurements as discussed in Chapter 5 while the Gaussian modeling uses hypothetical Gaussian surface realizations generated by the spectral method with the same rms roughness and autocorrelation length of the studied surface. The two modeling methods reveal negligibly small difference in the predicted emittance of Si-1. Both modeling results well agree with experiment within the expanded uncertainty of 0.010. It

should be noted that at $\lambda = 1000$ nm, the sample is slightly transparent even though its thickness is 500 μm. SGM cannot model the transmittance, thereby resulting in a slight overprediction. Compared to the emittance of a smooth surface in Figure 8.1a, the results shown in Figure 8.2a suggest that the emittance enhancement is insignificant for Si-1, less than 0.8% in the opaque region and 1.7% at 1000 nm.

According to Equation 3.4, emittance measurement for rough surfaces requires the correction factor η from a known sample BRDF. In the present work, it is assumed that modeling results of the Monte Carlo method in Chapter 5 are correct. Therefore, when the silicon surface reflectance is calculated with the Monte Carlo method, the correction factor is simultaneously calculated based on the solid angle between the beam spot and the entrance aperture. Note that correction factor calculation adds an assumption because a modeled result is not necessarily a true value. The anisotropic modeling shows that the correction factor η for Si-1 at $\theta_i = 7°$ does not change significantly with the

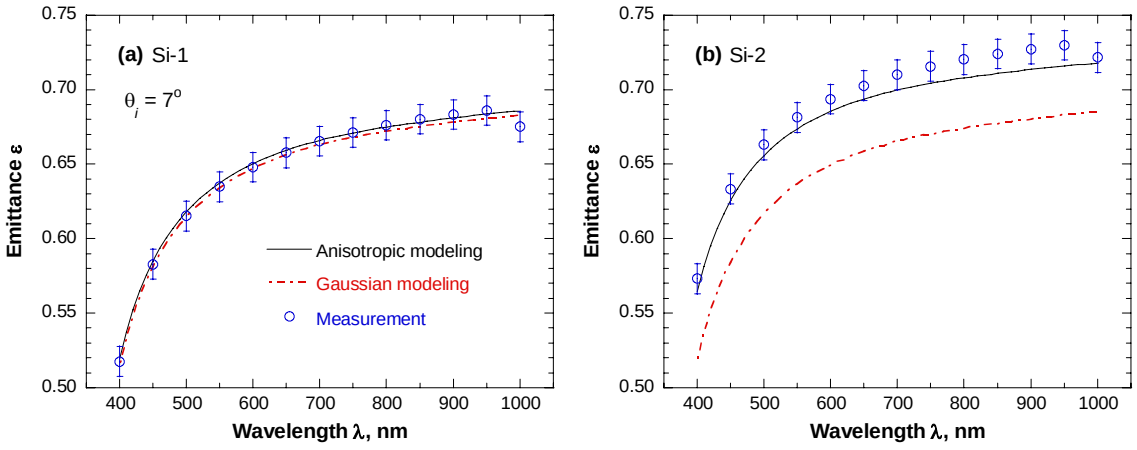

Figure 8.2 Emittance of Si-1 and Si-2 at near normal incidence. (a) Si-1; (b) Si-2. The anisotropic modeling relies on the measured topographic data whereas the Gaussian modeling assumes that the surfaces follow Gaussian statistics with corresponding roughness parameters σ and τ. Error bars indicate measurement uncertainty.

wavelength, and thus a constant value of 0.035 is applied for all the measurements in Figure 8.2a. The correction factor changes absolute values of measured emittance by 0.012 (relatively 1.9%) on the average. Emittance measurements would change by 0.005 under diffuse reflection assumption ($\eta = 0.015$). The 0.007 difference in measurements caused by two correction factors is within the experimental uncertainty. If the Gaussian modeling is used, the correction factor would be 0.055, which could change measurements by 0.020. It is believed that the correction factor based on the anisotropic modeling is more accurate.

Figure 8.2b shows a similar comparison for the emittance of Si-2 at wavelengths from 400 nm to 1000 nm. The correction factor η for all measurements of Si-2 can be approximated as 0.024, which is closer to the diffuse surface correction factor. The Gaussian modeling also yields essentially the same value of η for Si-2. The standard deviation of anisotropic modeling results is approximately 0.008 due to the artifacts in AFM measurements for Si-2. Experiment indicates that Si-2 gives rise to noticeable emittance enhancement. The average enhancement is 0.050 (7.8%), and the maximum is 0.058 (11.3%) at 400 nm. While the anisotropic modeling is in reasonable agreement with the experiment, the Gaussian modeling fails to predict the emittance enhancement.

The anisotropic modeling also predicts the large enhancement for Si-2, but the prediction is consistently lower than the measurement as shown in Figure 8.2b. The standard deviation between anisotropic modeling and measurement is 0.010 (absolute) or 1.5% (relative), which is within the measurement uncertainty. When Si-1 and Si-2 are compared, the difference between anisotropic modeling and measurement is larger for Si-2. The large difference for Si-2 is presumably due to the artifacts in the AFM

measurements and the limitation of GOA. The difference increase between anisotropic modeling and measurement with the wavelength indicates that the limitation of GOA is more dominant at long wavelengths. Meanwhile, the anisotropic modeling calculated with MSM also predicts emittance enhancement with the average difference of 0.004 from SGM. If the sphere measurement and topography measurement uncertainties are considered, it can be concluded that geometric optics is valid for Si-2 in predicting the emittance. This result is consistent with the recent study on the applicability of geometric optics for modeling the emittance [85].

Unlike the anisotropic modeling, the Gaussian modeling underpredicts the emittance of Si-2 by 7.0% on the average and maximum by 10.1% at 400 nm. The emittance enhancement of the Gaussian surface is insignificant, similarly to the emittance of a smooth surface in Figure 8.1a. The large difference between the two modeling results occurs due to the strongly anisotropic roughness of Si-2. The average microfacet inclination angle on the Gaussian surface is 9.7° from the relation of $\sqrt{2}\sigma/\tau$. However, the large and small side peaks in the SDF of Si-2 indicate that Si-2 possesses a larger number of the steep microfacets inclined at 25.2° and 54.7° than the Gaussian surface. Thus, the steep microfacets of Si-2 strengthen the cavity effects to trap incident light by multiple scattering, and the large enhancement cannot be predicted with the Gaussian surface statistics. It is the anisotropic roughness that enhances the emittance of Si-2. Therefore, detailed information on roughness statistics is essential for the accurate prediction of anisotropic surface emittance.

Figure 8.3 shows emittance variation with incidence angles for Si-1 and Si-2 at the 635 nm wavelength. The emittance for each polarization along both the *x* axis (ϕ_i =

0°) and the diagonal direction (ϕ_i = 45°) is measured to examine the dependence of anisotropic surface emittance on azimuthal angles. The correction factor η considerably depends on the zenith angle of incidence θ_i, and its values are tabulated in Table 8.1. The correction factor generally decreases as θ_i increases from a maximum at $\theta_i = 0°$ and becomes insignificant beyond $\theta_i = 30°$. Incident polarization little affects the correction factor.

The measured emittance in Figures 8.3a and 8.3b indicates that the dependence on azimuthal angles is negligible for Si-1 in accordance with the slightly anisotropic SDF. For Si-1, the anisotropic modeling agrees well with measurement although slight disagreement is observed at angles beyond $\theta_i = 40°$. One possible reason for the disagreement is the blocking by the supporting rod of the baffle, as discussed with Figure

Table 8.1 Correction factor η at the wavelength of 635 nm.

	Si-1				Si-2			
	p polarization		*s* polarization		*p* polarization		*s* polarization	
θ_i	$\phi_i = 0°$	$\phi_i = 45°$	$\phi_i = 0°$	$\phi_i = 45°$	$\phi_i = 0°$	$\phi_i = 45°$	$\phi_i = 0°$	$\phi_i = 45°$
0°	0.066	0.066	0.066	0.066	0.058	0.059	0.058	0.058
10°	0.024	0.025	0.024	0.024	0.011	0.017	0.011	0.017
20°	0.017	0.012	0.015	0.011	0.008	0.020	0.008	0.019
30°	0.012	0.006	0.009	0.005	0.007	0.034	0.006	0.029
40°	0.001	0.003	0.001	0.002	0.006	0.005	0.004	0.004
50°	0.000	0.001	0.000	0.000	0.003	0.006	0.002	0.004
60°	0.000	0.000	0.000	0.000	0.001	0.004	0.001	0.002

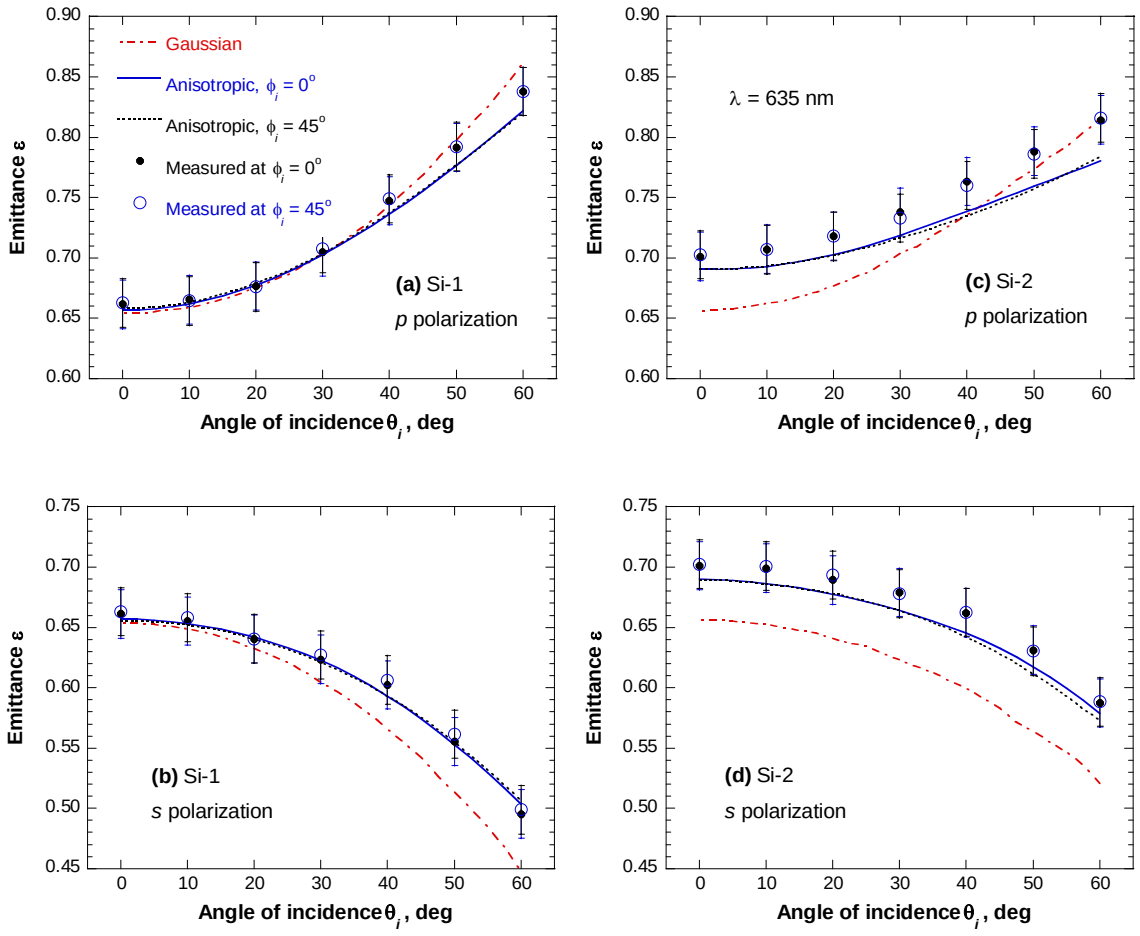

Figure 8.3 Emittance of Si-1 and Si-2 at the wavelength of 635 nm for two azimuthal angles $\phi_i = 0°$ and $\phi_i = 45°$. (a) Si-1 for *p* polarization; (b) Si-1 for *s* polarization; (c) Si-2 for *p* polarization; (d) Si-2 for *s* polarization.

8.1b. Wave features may also be responsible for the disagreement at large incidence angles because of optical roughness decrease. Note that the anisotropic modeling predicts larger errors at large incidence angles in Figure 8.3a than those in Figure 8.3b. Standard deviations between the anisotropic modeling and the measurement are approximately 0.010 and 0.007 for *p* and *s* polarizations, respectively. On the other hand, the Gaussian modeling tends to deviate from measurement at large angles, especially for *s* polarization.

As demonstrated in Chapters 5 and 7, the anisotropy of Si-2 is so strong that the BRDF of Si-2 along $\phi_i = 45°$ reveals prominent side peaks according to the SDF, whereas no side peaks appear in the BRDF along $\phi_i = 0°$. However, the measured and predicted emittance shows little difference between $\phi_i = 0°$ and $\phi_i = 45°$, as shown in Figures 8.3c and 8.3d. It seems that anisotropy roughness effects on the emittance even out in the azimuthal direction as a result of the integration of BRDF. Similarly to Figure 8.2b, the anisotropic modeling consistently underpredicts emittance for the two polarizations. The difference gradually increases with θ_i for *p* polarization while that for *s* polarization does not change noticeably. The standard deviations between the anisotropic modeling and the measurement are 0.022 and 0.015 for *p* and *s* polarizations, respectively, in Figures 8.3c and 8.3d. The large difference for *p* polarization at large incidence angles, regardless of Si-1 and Si-2, implies that wave features are more significant for *p* polarization than for *s* polarization. Meanwhile, the Gaussian modeling does not predict the emittance variation for *p* polarization correctly and largely underpredicts the emittance for *s* polarization.

When the emittance of Si-1 and Si-2 shown in Figure 8.3 is compared to that of a smooth silicon surface in Figure 8.1b, the emittance for *p* polarization is decreased at

large incidence angles whereas that for *s* polarization is increased. Ever if incident light is purely *p* or *s* polarized, depolarization generally occurs at randomly-oriented microfacets. The effect of depolarization is more prominent at large θ_i because the difference in the microfacet reflectivity of the two polarizations is large. Furthermore, depolarization affects the emittance of Si-2 more strongly than that of Si-1 due to larger surface roughness. Consequently, the emittance difference between the two polarizations is much smaller for Si-2. However, the average emittance for the two polarizations depends little on θ_i, indicating nearly diffuse emission up to 60° for both Si-1 and Si-2, similarly to that of a smooth surface.

The emittance of silicon wafers with a 107.2 nm thick SiO_2 coating at near normal incidence for random polarization is compared in Figure 8.4. The emittance of coated surfaces is calculated with SGM using the microfacet reflectivity in Equation 7.3. Therefore, modeling is based on geometric optics for surface roughness and thin-film optics for coatings. Despite the presence of coating, the correction factor does not change much from the values used in Figure 8.4. At the thickness of 107.2 nm, silicon dioxide

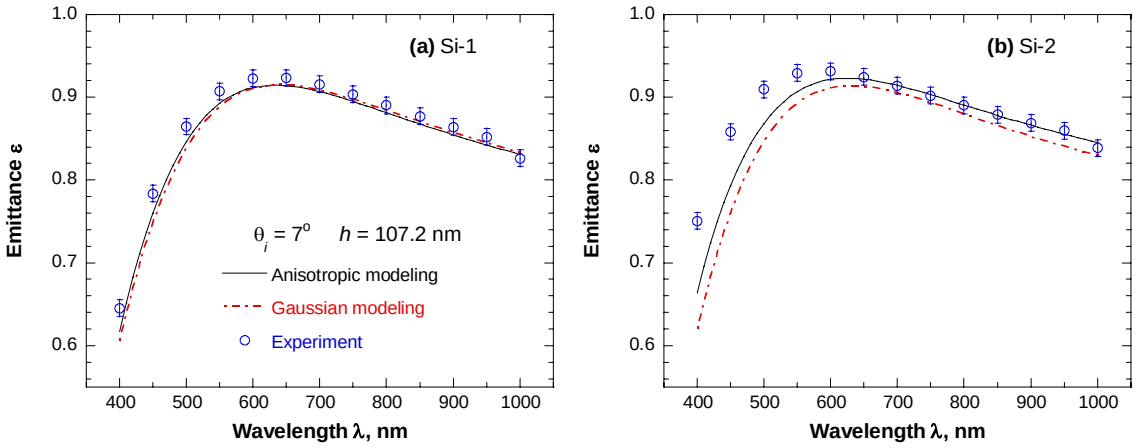

Figure 8.4 Emittance of Si-1 and Si-2 with a 107.2 nm thick SiO_2 coating at near normal incidence. (a) Si-1; (b) Si-2.

coating behaves like an antireflection coating, so the emittance of the coated surface is larger than that of the bare surface presented in Figure 8.2. The emittances of Si-1 and Si-2 are on the average enhanced by 34% and 38%, respectively, while the enhancement is large at short wavelengths.

Compared to the results in Figure 8.2, the disagreement between experiment and anisotropic modeling becomes larger due to coating. The standard deviation between the anisotropic modeling and the measurement for Si-1 is 0.014 (1.9%) which is slightly beyond the expanded sphere measurement uncertainty. The difference between the anisotropic modeling and the Gaussian modeling is still insignificant for Si-1. On the other hand, the disagreement between the anisotropic modeling and the measurement for Si-2 is increased, especially in short wavelengths, and the standard deviation of the anisotropic modeling is 0.033 (4.1%). Regardless of Si-1 and Si-2, the large disagreement at short wavelengths, i.e., at small h/λ is consistent with the observations in Section 7.2 and in Refs. [62,71]. The disagreement is more prominent for Si-2 because corner effects are more significant for surfaces with a larger rms slope. When the wavelength is larger than 600 nm, the standard deviation is 0.004 (0.5%) which is better that that of Si-2 shown in Figure 8.2b. The inherent limitation of GOA and the additional limitation of GOA due to coatings counteract at large wavelengths, resulting in the better agreement. Meanwhile, the average difference between the anisotropic modeling and the Gaussian modeling for Si-2 is approximately 2%. Antireflection coatings reduce the microfacet reflectivity and thereby the anisotropic roughness effect of Si-2 on multiple scattering. Therefore, a silicon dioxide coating decreases the difference between Si-2 and a corresponding Gaussian surface, compared to the difference shown in Figure 8.2b.

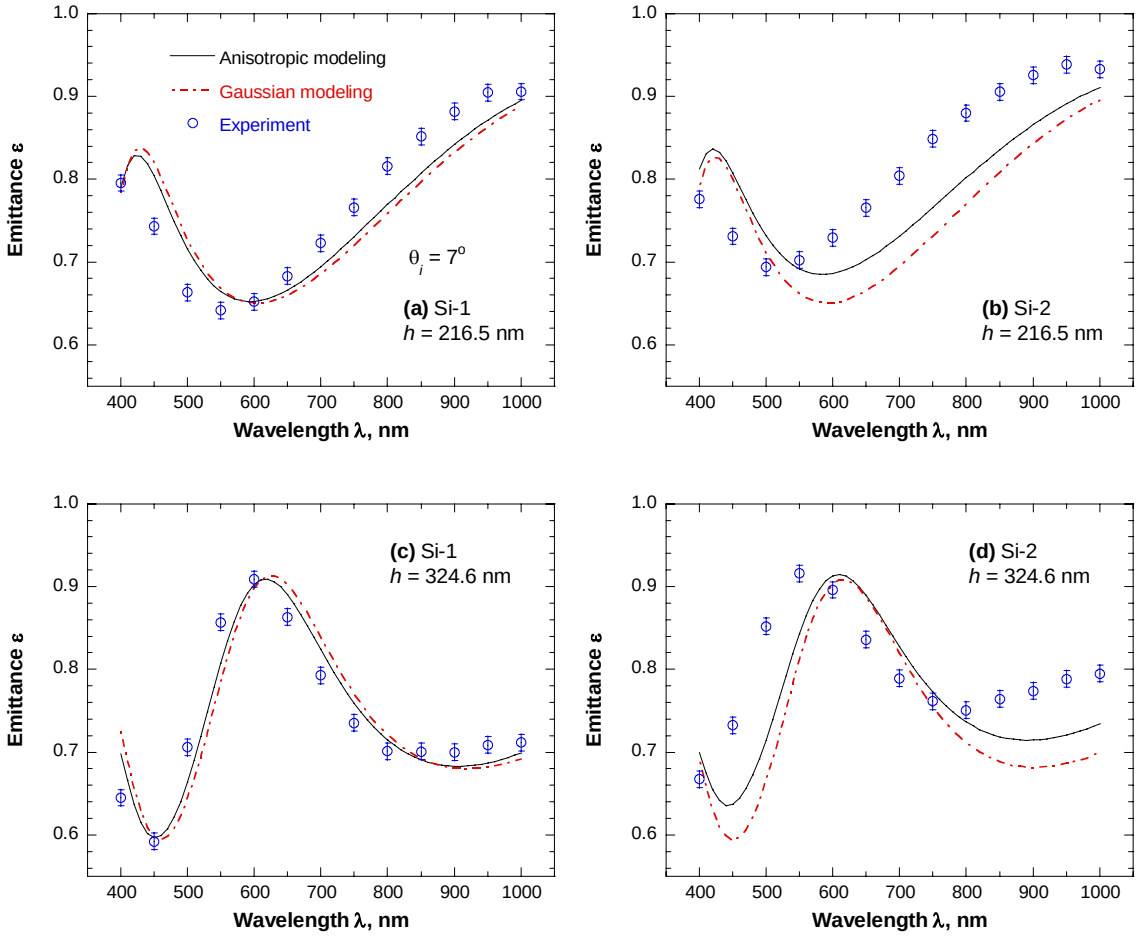

Figure 8.5 Emittance of Si-1 and Si-2 with 216.5 nm and 324.6 nm thick SiO_2 coatings at near normal incidence. (a) Si-1 and $h = 216.5$ nm; (b) Si-1 and $h = 324.6$ nm; (c) Si-2 and $h = 324.6$ nm; (d) Si-2 and $h = 324.6$ nm.

Consequently, Figure 8.4 implies that thin-film coating affects emittance more significantly than anisotropic roughness.

Subsequently, the emittance of Si-1 and Si-2 is compared in Figure 8.5 when coating thicknesses are 216.5 nm and 324.6 nm. Wave interferences inside silicon dioxide coating cause emittance oscillation, whose period decreases as coating thickness increases. Therefore, the emittance significantly varies within the wavelength range at the presence of coating, and the variation is more drastic at $h = 324.6$ nm than that at $h = 216.5$ nm . The anisotropic modeling captures general trends of the emittance variation. However, all the calculated emittance spectra tend to be shifted towards long wavelengths, and the shift is larger for Si-2 than Si-1. The emittance spectrum shift is related with coating thickness, as shown in Equation 7.4. In the present work, the thickness of coatings on rough surfaces is assumed to be equal to that on smooth reference surfaces. This assumption may break down when a thick coating is deposited and more presumably for rougher surfaces. Introduction of an effective coating thickness for rough surfaces, depending on roughness parameters, may be necessary for the correction of shifts and accurate emittance modeling.

The shift of modeling results in Figure 8.5 causes considerable disagreement with measurements. Anisotropic modeling errors can be as large as 8% for Si-1 and 16% for Si-2. In Figure 8.4, the agreement between the anisotropic modeling and the measurement is good at long wavelengths, i.e., small h/λ . However, 216.5 nm thickness is large enough to invalidate modeling assumption even at long wavelengths in Figure 8.5. Thin-film coating effects on emittance overwhelm anisotropic roughness effects at a

large coating thickness. From the comparisons in Figures 8.4 and 8.5, it may be concluded that modeling based on GOA is not applicable for the emittance if $h/\lambda > 0.2$.

CHAPTER 9

CONCULSIONS AND RECOMMENDATIONS

The research in this thesis has advanced the radiative property modeling of anisotropic rough surfaces. Monte Carlo ray-tracing methods that consider multiple scattering and depolarization are developed with attention to the observation of the reciprocity principle. The incorporation of AFM topography measurements into surface simulation algorithms enables the ray-tracing methods to deal with anisotropic roughness. Comparisons with BRDF and emittance measurements demonstrate that BRDF modeling that accounts for specific roughness statistics and multiple scattering is essential for accurate prediction. The major conclusions and findings of this thesis are as follows.

- MSM that Zhou and Zhang [38] proposed is further developed to satisfy the reciprocity principle and agree with the analytical BRDF model. When a rough surface is simulated with the normal vector of microfacets, the probability that an incoming ray hits a microfacet depends on the ray direction as well as the roughness slope distribution. Therefore, a weighted slope distribution function is introduced based on the project area of a microfacet into the ray direction. The weight function enables MSM to predict the BRDF that obeys the reciprocity principle and agrees with an analytical BRDF formula. However, comparisons with SGM and a rigorous approach indicate that MSM does not model multiple scattering for surfaces with very steep slopes at large incidence angles. SGM more accurately predicts multiple scattering based on the geometry of numerically generated surfaces.

- For the first time, the measured 2D topographic data are fully incorporated into the Monte Carlo ray-tracing methods to model non-Gaussian and anisotropic roughness. Good agreement between predicted and measured BRDFs demonstrates that the incorporation of topography measurement is essential for modeling the BRDF of anisotropically rough surfaces. The depolarization should be considered to accurately model the BRDF and study the dependence of radiative properties on the incident polarization. The Monte Carlo method predicts that first-order scattering is dominant for the studied surfaces up to $\theta_i = 45°$, particularly for *p* polarization. Because of the same roughness statistics between silicon and gold surfaces, their BRDFs describe many common features. However, split peak occurrence around the specular direction implies that wave interference may affect gold surface properties more than silicon surface properties. Some modeling discrepancies, observed around specular peaks and at large reflection angles, are mainly ascribed to inaccurate AFM measurements and geometric-optics limitations.

- In an attempt to handle wave effects with the ray-tracing method, the applicability of PRTM is evaluated. When an rms roughness is sufficiently large and thus wave effects are negligible, PRTM is essentially the same as KA and SGM. KA shows that coherent components result in narrow peaks in the specular direction for all the elements at a small rms roughness. PRTM also predicts coherent, narrow peaks. However, PRTM always underpredicts peaks and deviates from KA in angular regions other than the peaks. Although PRTM predicts partially coherent components unlike SGM, its inaccurate prediction indicates that the ray-tracing method is not applicable for modeling of wave features at surfaces with small roughness parameters.

- SiO_2 coating effects on the BRDF of silicon surfaces are investigated with an analytical model-based approach, in which slope distributions are obtained from BRDF measurements rather than from topography measurements. BRDFs significantly change depending on SiO_2 coating thickness while the underlying anisotropic features of silicon substrates affect the BRDF despite the presence of coating. Comparisons between predicted and measured BRDFs suggest that geometric optics should be applicable for a large range of coating thickness: up to $h/\lambda \approx 0.5$ for the slightly anisotropic wafer Si-1 ($\sigma/\tau \approx 0.1$) and up to $h/\lambda \approx 0.3$ for the strongly anisotropic wafer Si-2 ($\sigma/\tau \approx 0.2$) at normal incidence. Furthermore, large coating thickness does not necessarily degrade modeling accuracy. Besides inherent geometric-optics limitations without coating, additional limitations due to coating such as the corner effect and non-uniform coating thickness cause deviations in the predicted BRDF of coated surfaces.

- Emittances are calculated with the Monte Carlo method and compared with measurements using integrating sphere at a wavelength region from 400 to 1000 nm. Prediction based on topography measurement agrees well with emittance measurements within 1.5%. However, a simple assumption of the Gaussian surface yields 7% average errors for Si-2. If the emittance modeled with Gaussian statistics is used for an LPRT working at 950 nm to monitor Si-2 at 1000 °C, temperature is underpredicted by 7 °C, which does not meet the requirement for RTP. It is anisotropic roughness that increases multiple scattering and enhances the emittance noticeably. The significant role of anisotropic roughness in emittance enhancement suggests that the incorporation of surface topography into BRDF modeling is critical for emittance as well as BRDF. Even for Si-1, the emittance modeled with the Gaussian surface deviates at large angles.

However, SiO_2 coating reduces the anisotropic roughness effect on emittance enhancement, and coating effects on emittance overwhelm roughness effects at large thickness $h/\lambda > 0.2$.

In closure, this thesis research demonstrates importance of BRDF modeling based on specific roughness statistics for accurate radiative property prediction. This thesis focuses on BRDF modeling to predict radiative properties after roughness statistics are determined. However, rapid progress in surface metrology necessitates non-contact tools to probe and characterize surfaces. Since engineered surfaces are frequently anisotropic, an inverse procedure of the developed methods may be useful to obtain roughness statistics from BRDF measurements. Meanwhile, the basic assumption of this thesis research, i.e., geometric optics, revealed its limitations when an incidence angle is large, when an autocorrelation length is not sufficiently larger than an incident wavelength, or when a coating is thick compared to an incident wavelength. Further studies need to improve BRDF modeling based on other wave scattering theories. Since rigorous approaches such as the boundary integral method or the finite difference time domain method are rapidly growing lately, their application is highly recommended to overcome the limitations of geometric optics and unveil more anisotropic roughness effects. Furthermore, efforts to measure surface topography accurately will be needed to improve property prediction.

REFERENCES

[1] Siegel, R. and Howell, J.R., *Thermal Radiation Heat Transfer*, 4th ed., Taylor & Francis, New York, 2002.

[2] Modest, M.F., *Radiative Heat Transfer*, McGraw-Hill, New York, 1993.

[3] Mahan, J.R., *Radiation Heat Transfer: A Statistical Approach*, J. Wiley, New York, 2002.

[4] Beckmann, P. and Spizzichino, A., *The Scattering of Electromagnetic Waves from Rough Surfaces*, Artech House, Norwood, Massachusetts, 1987.

[5] Ogilvy, J.A., *Theory of Wave Scattering from Random Rough Surfaces*, A. Hilger, Bristol, England, 1991.

[6] Tsang, L., Kong, J.A., and Ding, K.-H., *Scattering of Electromagnetic Waves. Theories and Applications*, J. Wiley, New York, 2000.

[7] Elfouhaily, T.M. and Guerin, C.A., "A Critical Survey of Approximate Scattering Wave Theories from Random Rough Surfaces," Waves Random Media, Vol. 14, pp. R1-R40, 2004.

[8] Saillard, M. and Sentenac, A., "Rigorous Solutions for Electromagnetic Scattering from Rough Surfaces," Waves Random Media, Vol. 11, pp. R103-R137, 2001.

[9] Warnick, K.F. and Chew, W.C., "Numerical Simulation Methods for Rough Surface Scattering," Waves Random Media, Vol. 11, pp. R1-R30, 2001.

[10] Maradudin, A.A., Michel, T., McGurn, A.R., and Mendez, E.R., "Enhanced Backscattering of Light from a Random Grating," Ann. Phys., Vol. 203, pp. 255-307, 1990.

[11] Sanchez-Gil, J.A. and Nieto-Vesperinas, M., "Light Scattering from Random Rough Dielectric Surfaces," J. Opt. Soc. Am. A, Vol. 8, pp. 1270-1286, 1991.

[12] Torrance, K.E. and Sparrow, E.M., "Theory for Off-Specular Reflection from Roughened Surfaces," J. Opt. Soc. Am., Vol. 57, pp. 1105-1114, 1967.

[13] Toor, J.S. and Viskanta, R., "A Numerical Experiment of Radiant Heat Interchange by Monte Carlo Method," Int. J. Heat Mass Transfer, Vol. 11, pp. 883-897, 1968.

[14] Dimenna, R.A. and Buckius, R.O., "Quantifying Specular Approximations for Angular Scattering from Perfectly Conducting Random Rough Surfaces," J. Thermophys. Heat Transfer, Vol. 8, pp. 393-399, 1994.

[15] Makino, T., Nakamura, A., and Wakabayashi, H., "Directional Characteristics of Radiation Reflection on Rough Metal Surfaces with Description of Heat Transfer Parameters," JSME Int. J. B., Vol. 42, pp. 745-751, 1999.

[16] Tang, K. and Buckius, R.O., "The Geometric Optics Approximation for Reflection from Two-Dimensional Random Rough Surfaces," Int. J. Heat Mass Transfer, Vol. 41, pp. 2037-2047, 1998.

[17] Tang, K. and Buckius, R.O., "A Statistical Model of Wave Scattering from Random Rough Surfaces," Int. J. Heat Mass Transfer, Vol. 44, pp. 4059-4073, 2001.

[18] Roozeboom, F., "Introduction: History and Perspectives of Rapid Thermal Processing", Advances in Rapid Thermal and Integrated Processing (Edited by F. Roozeboom), Academic Publishers, Dordrecht, Netherlands, pp. 1-34, 1996.

[19] Timans, P.J., Sharangpani, R., and Thakur, R.P.S., "Rapid Thermal Processing", Handbook of Semiconductor Manufacturing Technology (Edited by Y. Nishi and R. Doering), Marcel Dekker, New York, pp. 201-286, 2000.

[20] Borisenko, V.E. and Hesketh, P.J., *Rapid Thermal Processing of Semiconductors*, Plenum Press, New York, 1997.

[21] Timans, P.J., "The Thermal Radiative Properties of Semiconductors", Advances in Rapid Thermal and Integrated Processing (Edited by F. Roozeboom), Academic Publishers, Dordrecht, Netherlands, pp. 35-102, 1996.

[22] Schietinger, C., "Wafer Temperature Measurement in RTP", Advances in Rapid Thermal and Integrated Processing (Edited by F. Roozeboom), Academic Publishers, Dordrecht, Netherlands, pp. 103-123, 1996.

[23] Frankman, D.J., Webb, B.W., and Jones, M.R., "Investigation of Lightpipe Volumetric Radiation Effects in RTP Thermometry," J. Heat Transfer, Vol. 128, pp. 132-141, 2006.

[24] Benjamin, K.T., "NIST High Accuracy Reference Reflectometer Spectrophotometer," J. Res. Natl. Inst. Stand. Technol., Vol. 111, pp. 9-30, 2006.

[25] Zhang, Z.M., "Surface Temperature Measurement Using Optical Techniques", Annual Review of Heat Transfer (Edited by C.L. Tien), Begell House, New York, Vol. 11, pp. 351-411, 2000.

[26] DeWitt, D.P. and Nutter, G.D., *Theory and Practice of Radiation Thermometry*, Wiley, New York, 1988.

[27] Zhu, Q.Z. and Zhang, Z.M., "Anisotropic Slope Distribution and Bidirectional Reflectance of a Rough Silicon Surface," J. Heat Transfer, Vol. 126, pp. 985-993, 2004.

[28] Zhu, Q.Z. and Zhang, Z.M., "Correlation of Angle-Resolved Light Scattering with the Microfacet Orientation of Rough Silicon Surfaces," Opt. Eng., Vol. 44, pp. 073601, 2005.

[29] O'Donnell, K.A. and Mendez, E.R., "Experimental Study of Scattering from Characterized Random Surfaces," J. Opt. Soc. Am. A, Vol. 4, pp. 1194-1205, 1987.

[30] Vandenabeele, P. and Maex, K., "Influence of Temperature and Backside Roughness on the Emissivity of Si Wafers During Rapid Thermal Processing," J. Appl. Phys., Vol. 72, pp. 5867-5875, 1992.

[31] Prokhorov, A.V., "Monte Carlo Method in Optical Radiometry," Metrologia, Vol. 35, pp. 465-471, 1998.

[32] Zhang, Z.M. and Zhou, Y.H., "An Effective Emissivity Model for Rapid Thermal Processing Using the Net-Radiation Method," Int. J. Thermophys., Vol. 22, pp. 1563-1575, 2001.

[33] Zhou, Y.H., Shen, Y.J., Zhang, Z.M., Tsai, B.K., and DeWitt, D.P., "A Monte Carlo Model for Predicting the Effective Emissivity of the Silicon Wafer in Rapid Thermal Processing Furnaces," Int. J. Heat Mass Transfer, Vol. 45, pp. 1945-1949, 2002.

[34] Tsao, J.C. and Su, C.C., "A Monte Carlo Model for Analyzing the Effects on Radiometric Temperature Measurement in Rapid Thermal Processor," Materials Science Forum, Vol. 505-507, pp. 325-330, 2006.

[35] Born, M. and Wolf, E., *Principles of Optics*, 7th (expanded) ed., Cambridge University Press, Cambridge [England]; New York, 1999.

[36] O'Donnell, K.A. and Knotts, M.E., "Polarization Dependence of Scattering from One-Dimensional Rough Surfaces," J. Opt. Soc. Am. A, Vol. 8, pp. 1126-1131, 1991.

[37] Zhao, Y.-P., Wang, G.-C., and Lu, T.-M., *Characterization of Amorphous and Crystalline Rough Surface: Principles and Applications*, Academic Press, San Diego, California, 2001.

[38] Zhou, Y.H. and Zhang, Z.M., "Radiative Properties of Semitransparent Silicon Wafers with Rough Surfaces," J. Heat Transfer, Vol. 125, pp. 462-470, 2003.

[39] Press, W.H., *Numerical Recipes in C: The Art of Scientific Computing*, 2nd ed., Cambridge University Press, Cambridge, New York, 1992.

[40] Thorsos, E.I., "The Validity of the Kirchhoff Approximation for Rough Surface Scattering Using a Gaussian Roughness Spectrum," J. Acoust. Soc. Am., Vol. 83, pp. 78-92, 1988.

[41] Chan, T.K., Kuga, Y., Ishimaru, A., and Le, C.T.C., "Experimental Studies of Bistatic Scattering from Two-Dimensional Conducting Random Rough Surfaces," IEEE Trans. Geosci. Remote Sens., Vol. 34, pp. 674-680, 1996.

[42] Nieto-Vesperinas, M. and Soto-Crespo, J.M., "Monte Carlo Simulations for Scattering of Electromagnetic Waves from Perfectly Conductive Random Rough Surfaces," Opt. Lett., Vol. 12, pp. 979-981, 1987.

[43] Lu, J.Q., Maradudin, A.A., and Michel, T., "Enhanced Backscattering from a Rough Dielectric Film on a Reflecting Substrate," J. Opt. Soc. Am. B, Vol. 8, pp. 311-318, 1991.

[44] Gu, Z.H., Lu, J.Q., and Maradudin, A.A., "Enhanced Backscattering from a Rough Dielectric Film on a Glass Substrate," J. Opt. Soc. Am. A, Vol. 10, pp. 1753-1764, 1993.

[45] Ghmari, F., Ghbara, T., Laroche, M., Carminati, R., and Greffet, J.J., "Influence of Microroughness on Emissivity," J. Appl. Phys., Vol. 96, pp. 2656-2664, 2004.

[46] Chen, M.F. and Fung, A.K., "A Numerical Study of the Regions of Validity of the Kirchhoff and Small Perturbation Rough Surface Scattering Models," Radio Science, Vol. 23, pp. 163-170, 1988.

[47] Tang, K., Dimenna, R.A., and Buckius, R.O., "Regions of Validity of the Geometric Optics Approximation for Angular Scattering from Very Rough Surfaces," Int. J. Heat Mass Transfer, Vol. 40, pp. 49-59, 1997.

[48] Soto-Crespo, J.M. and Nieto-Vesperinas, M., "Electromagnetic Scattering from Very Rough Random Surfaces and Deep Reflection Gratings," J. Opt. Soc. Am. A, Vol. 6, pp. 367-384, 1989.

[49] Soto-Crespo, J.M., Nieto-Vesperinas, M., and Friberg, A.T., "Scattering from Slightly Rough Random Surfaces - a Detailed Study on the Validity of the Small Perturbation Method," J. Opt. Soc. Am. A, Vol. 7, pp. 1185-1201, 1990.

[50] Lettieri, T.R., Marx, E., Song, J.F., and Vorburger, T.V., "Light Scattering from Glossy Coatings on Paper," Appl. Opt., Vol. 30, pp. 4439-4447, 1991.

[51] Tang, K., Kawka, P.A., and Buckius, R.O., "Geometric Optics Applied to Rough Surfaces Coated with an Absorbing Thin Film," J. Thermophys. Heat Transfer, Vol. 13, pp. 169-176, 1999.

[52] Elson, J.M., "Infrared Light Scattering from Surfaces Covered with Multiple Dielectric Overlayers," J. Opt. Soc. Am., Vol. 67, pp. 253-253, 1977.

[53] Icart, I. and Arques, D., "Simulation of the Optical Behavior of Rough Identical Multilayer," SPIE 4100, pp. 84-95, 2000.

[54] Shen, Y.J., Zhu, Q.Z., and Zhang, Z.M., "A Scatterometer for Measuring the Bidirectional Reflectance and Transmittance of Semiconductor Wafers with Rough Surfaces," Rev. Sci. Inst., Vol. 74, pp. 4885-4892, 2003.

[55] Thomas, T.R., *Rough Surfaces*, 2nd ed., Imperial College Press, London, 1999.

[56] Church, E.L. and Takacs, P.Z., "Effects of Non-Vanishing Tip Size in Mechanical Profile Measurements," SPIE 1332, pp. 504-514, 1991.

[57] O'Donnell, K.A., "Effects of Finite Stylus Width in Surface-Contact Profilometry," Appl. Opt., Vol. 32, pp. 4922-4928, 1993.

[58] Proctor, J.E. and Barnes, P.Y., "NIST High Accuracy Reference Reflectometer Spectrophotometer," J. Res. Natl. Inst. Stand. Technol., Vol. 101, pp. 619-627, 1996.

[59] Zaworski, J.R., Welty, J.R., and Drost, M.K., "Measurement and Use of Bi-Directional Reflectance," Int. J. Heat Mass Transfer, Vol. 39, pp. 1149-1156, 1996.

[60] White, D.R., Saunders, P., Bonsey, S.J., van de Ven, J., and Edgar, H., "Reflectometer for Measuring the Bidirectional Reflectance of Rough Surfaces," Appl. Opt., Vol. 37, pp. 3450-3454, 1998.

[61] Lee, B.J., Zhang, Z.M., Early, E.A., DeWitt, D.P., and Tsai, B.K., "Modeling Radiative Properties of Silicon with Coatings and Comparison with Reflectance Measurements," J. Thermophys. Heat Transfer, Vol. 19, pp. 558-569, 2005.

[62] Lee, H.J. and Zhang, Z.M., "Measurement and Modeling of the Bidirectional Reflectance of SiO_2 Coated Si Surfaces," Int. J. Thermophys., 2006 (in press).

[63] Lee, H.J., Bryson, A.C., and Zhang, Z.M., "Measurement and Modeling of the Emittance of Silicon Wafers with Anisotropic Roughness," Int. J. Thermophys., 2006 (submitted).

[64] Weidner, V.R. and Hsia, J.J., "Reflection Properties of Pressed Polytetrafluoroethylene Powder," J. Opt. Soc. Am., Vol. 71, pp. 856-861, 1981.

[65] Edwards, D.K., Gier, J.T., Nelson, K.E., and Roddick, R.D., "Integrating Sphere for Imperfectly Diffuse Samples," J. Opt. Soc. Am., Vol. 51, pp. 1279-1288, 1961.

[66] Hanssen, L.M. and Snail, K.A., "Integrating Spheres for Mid- and near-Infrared Reflection Spectroscopy", Handbook of Vibrational Spectroscopy (Edited by J.M. Chalmers and P.R. Griffiths), Wiley, New York, Vol. 2, 2002.

[67] Hanssen, L.M., "Effects of Restricting the Detector Field of View When Using Integrating Spheres," Appl. Opt., Vol. 28, pp. 2097-2103, 1989.

[68] Macaskill, C., "Geometric Optics and Enhanced Backscatter from Very Rough Surfaces," J. Opt. Soc. Am. A, Vol. 8, pp. 88-96, 1991.

[69] Prokhorov, A.V. and Hanssen, L.M., "Algorithmic Model of Microfacet BRDF for Monte Carlo Calculation of Optical Radiation Transfer," SPIE 5192, pp. 141-157, 2003.

[70] Lee, H.J., Lee, B.J., and Zhang, Z.M., "Modeling the Radiative Properties of Semitransparent Wafers with Rough Surfaces and Thin-Film Coatings," J. Quant. Spectrosc. Radiat. Transfer, Vol. 93, pp. 185-194, 2005.

[71] Zhu, Q.Z., Lee, H.J., and Zhang, Z.M., "The Validity of Using Thin-Film Optics in Modeling the Bidirectional Reflectance of Coated Rough Surfaces," J. Thermophys. Heat Transfer, Vol. 19, pp. 548-557, 2005.

[72] Smith, B.G., "Geometrical Shadowing of a Random Rough Surface," IEEE Trans. Antennas Propag., Vol. 15, pp. 668-671, 1967.

[73] Lee, H.J., Chen, Y.B., and Zhang, Z.M., "Directional Radiative Properties of Anisotropic Rough Silicon and Gold Surfaces," Int. J. Heat Mass Transfer, 2006 (in press).

[74] Tsang, L. and Kong, J.A., "Energy Conservation for Reflectivity and Transmissivity at a Very Rough Surface," J. Appl. Phys., Vol. 51, pp. 673-680, 1980.

[75] Caron, J., Lafait, J., and Andraud, C., "Catastrophe Theory Interpretation of Multiple Peaks Produced by Light Scattering from Very Rough Dielectric Surfaces," Physica B, Vol. 325, pp. 76-85, 2003.

[76] Wu, S.C., Chen, M.F., and Fung, A.K., "Non-Gaussian Surface Generation," IEEE Trans. Geosci. Remote Sens., Vol. 26, pp. 885-888, 1988.

[77] Knotts, M.E., Michel, T.R., and O'Donnell, K.A., "Comparisons of Theory and Experiment in Light Scattering from a Randomly Rough Surface," J. Opt. Soc. Am. A, Vol. 10, pp. 928-941, 1993.

[78] Palik, E.D., *Handbook of Optical Constants of Solids*, Academic Press, Orlando, Florida, 1985.

[79] Bruce, N.C., "Scattering of Light from Surfaces with One-Dimensional Structure Calculated by the Ray-Tracing Method," J. Opt. Soc. Am. A, Vol. 14, pp. 1850-1858, 1997.

[80] Bruce, N.C., "Calculations of the Mueller Matrix for Scattering of Light from Two-Dimensional Surfaces," Waves Random Media, Vol. 8, pp. 15-28, 1998.

[81] Lee, H.J. and Zhang, Z.M., "Applicability of Phase Ray-Tracing Method for Light Scattering from Rough Surfaces," J. Thermophys. Heat Transfer, 2006 (submitted).

[82] Howell, J.R. and Perlmutter, M., "Monte Carlo Simulation of Thermal Transfer through Radiant Media between Gray Walls," J. Heat Transfer, Vol. 86, pp. 116-122, 1964.

[83] Mitsas, C.L. and Siapkas, D.I., "Generalized Matrix-Method for Analysis of Coherent and Incoherent Reflectance and Transmittance of Multilayer Structures with Rough Surfaces, Interfaces, and Finite Substrates," Appl. Opt., Vol. 34, pp. 1678-1683, 1995.

[84] Lee, B.J., Khuu, V.P., and Zhang, Z.M., "Partially Coherent Spectral Transmittance of Dielectric Thin Films with Rough Surfaces," J. Thermophys. Heat Transfer, Vol. 19, pp. 360-366, 2005.

[85] Ghmari, F., Sassi, I., and Sifaoui, M.S., "Directional Hemispherical Radiative Properties of Random Dielectric Rough Surfaces," Waves Random Complex, Vol. 15, pp. 469-486, 2005.

VITA

Hyunjin Lee was born in Chungbuk, South Korea on June 7, 1974. He attended Seoul National University and received his Bachelor and Master Degrees in the School of Mechanical and Aerospace Engineering in 2000 and 2002, respectively. He came to the United States of America in 2002 to pursuit his Ph. D. degree in the George W. Woodruff School of Mechanical Engineering at the Georgia Institute of Technology. His research interests include heat transfer in nano/micro scales, thermal management in electronic and optical devices, direct energy conversion, and so on. He is a member of the American Society of Mechanical Engineers and the American Institute of Aeronautics and Astronautics.